博士論文

Materials Exploration and Reaction Mechanism Analyses of Iron-based Cathode Materials for Rechargeable Batteries

（二次電池用鉄系正極の材料探索と反応機構解析）

Gosuke Oyama（大山 剛輔）

Department of Chemical System Engineering

Graduate school of Engineering

The University of Tokyo

Tokyo, Japan

Table of contents

1. General introduction

References

Part I Electrochemical behaviors of Olivine Lithium Iron Phosphate

2. Kinetics of Nucleation and Growth in Two-Phase Electrochemical Reaction of Li_xFePO_4

3. Electrochemical Properties of Heterosite $FePO_4$ in Aqueous Mg^{2+} Electrolytes

Part II Alluaudite sodium iron sulfate as a sodium-ion battery cathode

4. A 3.8 V Earth-Abundant Sodium Battery Electrode

5. Off-stoichiometry in Alluaudite-type Sodium Iron Sulfate $Na_{2+2x}Fe_{2-x}(SO_4)_3$ as an Advanced Sodium Battery Cathode Material

6. Sodium Intercalation Mechanism of 3.8 V Class Alluaudite Sodium Iron Sulfate

7. Combined Experimental and Computational Analyses on Electronic Structure of Alluaudite Sodium Iron Sulfate

1. General introduction

1.1Rechargeable batteries

1.1.1 Overview

"Portability" builds upon rechargeable batteries. Nowadays, a wide range of applications (e.g. laptop computers, cameras, mobile phones, and electric vehicles) are empowered by rechargeable batteries, which are indispensable in our modern lives. At 2013, more than five billion cells were sold only for lithium-ion batteries.[1] Over centuries, rechargeable batteries have been under development, and currently lead acid, nickel cadmium (Ni-Cd), nickel-metal hydride (Ni-MH), high temperature (e.g. sodium-sulfur[2], and ZEBRA[3]), and lithium-ion batteries are used as commercial rechargeable batteries.

All of the rechargeable batteries are a type of chemical batteries, which reversibly convert chemical and electronic energy. The operating principle for any rechargeable battery is analogous at the fundamental level. A battery should consist of at least three components; a positive electrode (usually referred to as cathode in battery community), an electrolyte, and a negative electrode (usually referred to as anode) as shown in Fig. 1.1. In rechargeable batteries, electrochemical reduction occurs at the cathode, and oxidation occurs at the anode for discharging process, and vice versa for charging process. Besides, chemical potential of the cathode should be lower than that of the anode, while both of them are within a band gap of electrolyte to avoid electrolyte decomposition in principle.

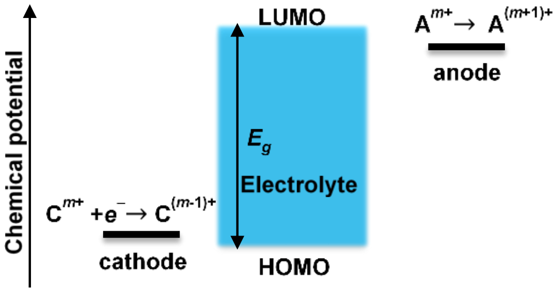

Figure 1.1 Schematic representation of the operating system of a chemical battery.

For designing better rechargeable batteries, it is of key importance to consider all of those components under a multidimensional perspective. In general, rechargeable batteries should display superior performance for the following four major parameters: (i) the gravimetric and volumetric energy densities, (ii) cycle life, (iii) coulombic efficiency, and (iv) power density. The three types of rechargeable batteries (lithium-ion, sodium-ion, and magnesium batteries) will be introduced in the following sections with respect to the parameters listed above along with cost and safety.

1.1.2 Lithium-ion battery

Lithium-ion battery is one of the most ideal systems based on the criterion (i) in section 1.1.1. Lithium has the lowest electrode potential ($E = -3.04$ V versus standard hydrogen electrode, SHE), which produces the largest potential difference between the cathode and the anode. Besides, the mass/volume of a lithium-ion per electron is minimal among all alkali metals. Owing to this merit, lithium-ion battery has the highest energy density (210 Wh/kg) of all commercial rechargeable batteries, and has dominated the portable device market since the early 1990s.[4,5] Moreover, lithium-ion battery has started to enter large-scale applications, especially for automobiles.[1]

Schematic representation of lithium-ion battery is illustrated in Fig. 1.2. Lithium-ion battery can be charged/discharged by shuttling of lithium ions, often referred to as (de)intercalation, between the cathode and anode through an electrolyte. The most typical electrochemical reaction of lithium-ion battery can be described as,

$$\text{(cathode)} \quad \mathrm{LiCoO_2} \rightarrow \mathrm{Li_{1-\mathit{x}}CoO_2} + x\mathrm{Li^+} + x\mathrm{e^-} \qquad (1.1)$$

$$\text{(anode)} \quad 6\mathrm{C} + x\mathrm{Li^+} + x\mathrm{e^-} \rightarrow \mathrm{Li_\mathit{x}C_6} \qquad (1.2).$$

The initial state of the lithium-ion battery is the discharged state and initial charging is required before usage as is common for rechargeable batteries. Upon charging, an external electric potential forces lithium ions to migrate from the cathode to the anode through the electrolyte.

Upon discharging, lithium ions migrate from the anode through the electrolyte, and back into the cathode. At the same time, electrons move through the external circuit, and this performs external work.

Looking back at the history of lithium-ion battery, major leaps forward were taken in the 1970-1980s. Mizushima, and Goodenough et al. reported layered Li_xCoO_2 as an intercalation cathode material, which delivers a high electrode potential of 3.9 V versus Li/Li^+ with a specific capacity of 140 $mAhg^{-1}$ (theoretical capacity: 270 $mAhg^{-1}$).[6] The layered oxides will be discussed further in section 1.2. Furthermore, substitution of lithium metal by an intercalation material (e.g hard carbon, and graphite) improved cycle life and safety.[7] Graphite intercalation compound (GIC) had been known as a possible lithium host framework, which delivers an excellent capacity of 372 $mAhg^{-1}$ as an anode.[8] Combination with lithium embedded cathode $LiCoO_2$ and graphite anode was instrumental in commercialization of 3.6 V class lithium-ion battery in 1991.[9]

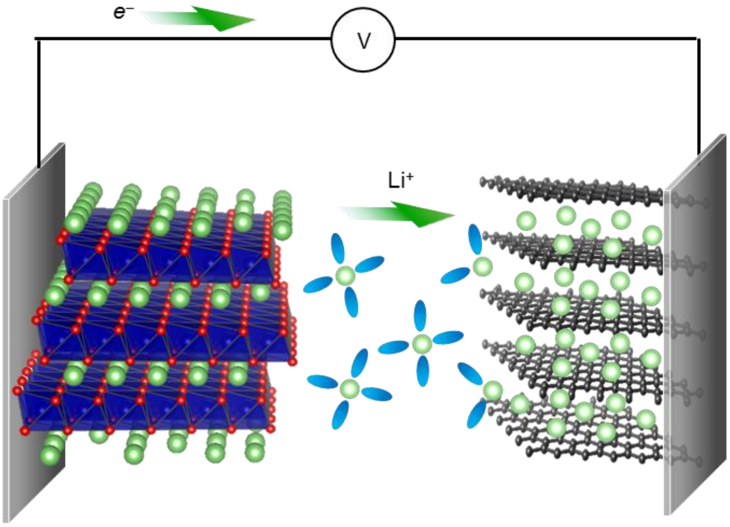

Figure 1.2 Schematic image of lithium-ion battery system. Green arrows indicate flow of Li^+ and electrons upon charging process.

1.1.3 Sodium-ion battery

For large-scale applications of rechargeable batteries, stricter restrictions are imposed on the criteria mentioned in section 1.1.1 not only for the electrode performance parameters, but safety and cost also. As was mentioned in the section 1.1.2, in large-scale energy storage applications, the presence of lithium-ion batteries has been expanding. However, it is yet to satisfy the criteria, especially with regards to cost.

As one of the most promising alternatives, sodium-ion battery has rapidly re-attracted the attention of battery reseachers.[10] Owing to high natural abundance of sodium elements, the concept for sodium battery, which utilizes sodium ion as the guest species was originally reported for TiS_2[11,12], followed by Na_xCoO_2[13,14] already in 1970-1980s. However, as a charge charrier in rechargeable battery, sodium is inferior to lithium. The redox potential of sodium (–2.71 V vs. SHE) is greater than that of lithium (–3.04 V vs. SHE), and the weight per electron of sodium is more than three times that of lithium, which intrinsically limits the maximum energy density of sodium ion batteries.

Due to higher polarizability and lower Lewis acidity of sodium ions, the activation energies for charge transfer at electrode/electrolyte interface and migration within layered structure are expected to be lower than those for lithium ion.[10,15,16] These processes are recognized as the two major rate limiting steps in battery operation, suggesting that sodium ion battery can potentially compete with lithium ion battery.[16] Moreover, rich crystal chemistry can be expected due to the ionic radius difference between sodium ions (1.02 Å for octahedral coordination) and 3*d* transition metals (typically 0.5~0.6 Å), which could help sodium ion batteries surpass state-of-the-art lithium ion battery systems.[10]

As cathode materials, intercalation compounds have been reported as promising candidates, which will be further described in section 1.2.

The graphite anode, which used as anode in commercial lithium-ion battery is not applicable to sodium-ion battery, and the most promising candidate is hard carbon, so far. Hard carbon is artificial carbon consisted of disordered graphite layers. This compound showed reversible capacity of ~250 $mAhg^{-1}$ (retained over 200 cycles).[17,18] Besides, titanium oxide based compounds, such as TiO_2, P2-$Na_{2/3}[Li_{0.22}Ti_{0.78}]O_2$ and $Na_2Ti_3O_7$) showed relatively high electrochemical performances.[19–21] These materials store sodium by intercalation mechanism, thereby delivering reversible behavior at the expense of relatively lower capacities. Conversion type electrodes (e.g phosphorous, Sb_2S_3, SnS_2 and Sn_4P_3) also showed very high capacities (> 500 $mAhg^{-1}$).[22–25] More recently, a family of metal carbide MXene, (e.g. Ti_3C_2 and Ti_2C) were reported as possible sodium ion battery anodes.[26,27] These compounds store charge as a pseudocapacitor with reversible capacity of 200 $mAhg^{-1}$ (> 100 cycles) and fast kinetics.[27]

As electrolyte candidates, electrochemical performances of sodium salts dissolved in carbonate ester solvents and their mixtures have been measured with the hard carbon as anode and $Na_3V_2(PO_4)_2F_3$ as cathode.[28,29] $NaPF_6$ with ethylene carbonate (EC), proplylene carbonate (PC), and diethyl carbonate(DEC) (with optimized mixing ratio 45 : 45 : 10 vol.%) drastically improved electrochemical performance owing to high ionic conductivity of electrolyte and stable Surface Electrolyte Interface (SEI) formation.[28] As an additive for electrolyte, fluoroethylene carbonate (FEC) can improve the reversibility of electrochemical performances also.[30]

1.1.4 Magnesium battery

Another possible way to exceed theoretical energy density of the current state-of-the-art lithium-ion battery is utilization of divalent cations, such as Mg^{2+}. Contrary to lithium, magnesium element is earth-abundant (23,000 ppm as compared with 20 ppm for Li), cheap (ca. \$ 2.85 /kg), and less reactive in the air.[31–33] Furthermore, magnesium metal has large theoretical capacity (2205 $mAhg^{-1}$), which is about six times higher than that of the commercial graphite anode (372 $mAhg^{-1}$) in lithium ion battery, with relatively low redox potential at -2.37 V (versus SHE). Intriguingly, the magnesium metal might be applicable for the anode of magnesium battery (thereby, namely as “magnesium battery”), because it does not favor dendritic morphology unlike lithium.[34] Both experimental and computational works indicated the anisotropic growth of the magnesium metal along 001 direction without any dendrite formation in various Grignard's reagents/ethereal electrolytes, which can be due to more covalent bonding character between magnesium than lithium.[35–37] However, two intrinsic obstacles still exist and stunt further development of magnesium batteries for practical application.

One is spontaneous formation of passivation film on magnesium metal anode, which inhibits Mg^{2+} migration and further electrochemical reactions in most of electrolytes.[38–40] Reversible electrochemical reaction of Mg^{2+}/Mg was possible in only a limited number of electrolytes, such as $Mg(AlCl_2RR')$ (R, R' = alkyl group) dissolved tetrahydrofuran (THF)[41], $Mg(BH_4)_2$ dissolved diglyme, and magnesium trifluoromethylsulfonyl-amide ($Mg(TFSA)_2$) dissolced triglyme. [33,42–44]

The other is a sluggish bulk diffusion process of magnesium ion within host frameworks of cathode materials. The Mg^{2+} diffusion process accompanies extraction of strongly trapped Mg^{2+} within the host framework, and drastic change of a local electronic state by a two-electron reaction. At present, these effects can be suppressed by (i) cluster structure, (ii) shielding with electroneutral molecules, and (iii) particle nano-sizing.

(i) Cluster structure

One possible way to suppress these effects is a utilization of cluster structures. Chevrel phase Mo_6T_8 (T = S and Se) is the first family of materials, which allows fast and reversible Mg^{2+} intercalation.[41] The Mo_6S_8 electrode showed reversible capacity of 122 mAg^{-1} at ca. 1.1 V versus

Mg^{2+}/Mg with a minimal polarization at 60 °C.[41] The crystal structure of Chevrel phase, Mo_6S_8 is illustrated in Fig. 1.3.

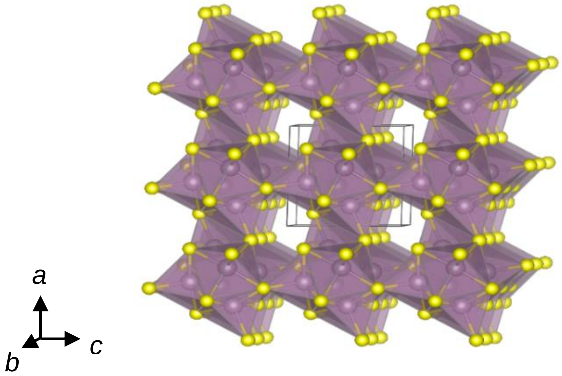

Figure 1.3 Crystal structure of Chevrel phase Mo_6S_8. Mo, S ions, and MoS_6 units are shown in purple, yellow, and purple octahedra, respectively.

In the Chevrel phase, a fundamental structure unit is a Mo_6S_8 cluster, in which molybdenum ions forms Mo_6 octahedral surround by a cube of sulfur ions.[45] The Mo_6S_8 clusters edge-shares with each other and forms a 3D open $[Mo_6S_8]_\infty$ framework. Due the strong hybridization within a Mo_6 octahedra, the cluster cooperatively accommodates up to four electrons. The unique charge compensation mechanism enables the fast and reversible intercalation of Mg^{2+} as well as other divalent cations such as Zn^{2+}, Cd^{2+}, Ni^{2+}, and etc.[41,46–48] More recently, orthorhombic-Mo_9Se_{11} with the cluster structure also showed reversible Mg^{2+} intercalation (up to x ~ 1.5 in $Mg_xMo_9Se_{11}$), and fullerene (C_{60} cluster) showed the capacity of 50 $mAhg^{-1}$ (up to x ~ 2 in Mg_xC_{60}) with a flat voltage plateau at ~1.5 V. [49,50] Therefore, the delocalization of electrons with the cluster structure might be a key for fast and reversible Mg^{2+} intercalations, but, this concept obviously sacrifices energy density of the battery, in exchange.

(ii) Shielding with electroneutral molecules

Shielding the charge of Mg^{2+} with electroneutral molecules, such as H_2O is another effective way.[47] V_2O_5 aerogels[51,52], and Prussian Blue Analog (PBA), $A_kM_l[M'(CN)_6]_m\ nH_2O$[53,54] showed electrochemical activities in aqueous electrolytes.

(iii) Particle nano-sizing

Besides, decreasing a particle size into nanometric scale can activates many of cathode materials. In fact, the electrochemical activity with Mg^{2+} has been reported for V_6O_{13},[55] MoS_2,[56] $MgMSiO_4$ (M = Mn, Fe and Co),[44,57,58] RuO_2,[59] Co_3O_4,[60] TiS_2,[61] α-, Hollandite-, and Birnessite-MnO_2[62,63]. Generally, they showed the high initial capacities (~100 $mAhg^{-1}$) and high voltages (> 2 V). However, the electrochemical behaviors are irreversible with slow kinetics, which are far from topotactic intercalation reaction. Their reaction mechanisms are still under debate.

1.2 Intercalation cathode materials

Intercalation reaction is insertion/extraction of “guest” ion into/from rigid “host” framework, which has been well known for graphite intercalation compounds (GICs). In principle, the reaction is totally topotactic, which ensures the reversibility as electrodes in rechargeable batteries.

Titanium disulfide TiS_2 is the first example of an intercalation compound used as a cathode material for lithium battery.[11,12,64] TiS_2 has the CdI_2-type layered structure, in which sulfur ions are arrayed as hexagonal close packing (hcp) array, and titanium ions occupy a half of the octahedral sites. Lithium ions are intercalated in between TiS_2 layers and reversely deintercalated. Rigid host framework of TiS_2 enables the reversible and fast intercalation without phase transformations.[11] Two important classes of cathode materials will be introduced in the following section 1.2.1 and 1.2.2.

1.2.1 Layered oxides

Layered oxides have been extensively studied over decades as cathode materials both for lithium and sodium-ion batteries. As was mentioned in section 1.1.2, electrochemical lithium intercalation/extraction was reported for Li_xCoO_2. This compound is isostructural to α–$NaFeO_2$, which is consisted of cubic close packing (ccp) order of oxygen ions, whereas 3*d* transition metal and alkali metal occupy octahedral sites in between oxygen ions alternately, forming transition metal layer, and alkali metal layer. The specific capacity of 140 $mAhg^{-1}$ (i.e. ~50 % of theoretical capacity: 273 $mAhg^{-1}$) is commercially used to avoid irreversible structure transformation above 4.2 V vs. Li/Li^+.[65,66] Thereafter, tremendous studies have been conducted for substituting cobalt with the other 3*d* transition metals (e.g. Ni, Mn, and Fe), doping inert cations (e.g. Mg, and Al), and surface modifications. At present, $LiNi_{1-x-y}Co_xAl_yO_2$ and $LiNi_{1-x-y}Mn_xCo_yO_2$ systems are successful outcomes due to their larger specific capacities (>150 $mAhg^{-1}$) and partial replacement of expensive and toxic cobalt ion. Besides, O3-type layered oxides, Na_xMO_2 (e.g. M = Cr[67,68], Mn[69,70], Fe[71,72], Co[14], Ni[73], and their solid solutions[74,75]), P2-type Na_xMO_2 (e.g. M = solid solutions of Mn, Fe, Co, Ni, and Mg)[76–79] have been reported as cathode materials for sodium-ion battery. More reviews for important electrochemically active oxides, such as spinel $Li_xMn_2O_4$, $Li_xNi_{0.5}Mn_{1.5}O_4$, and lithium rich layered oxides, are beyond the scope of this thesis.

1.2.2 Oxyanionic compounds

Oxyanionic (or polyanionic) compounds are another important family of intercalation materials, which are main targets of the present thesis. In 1970s, a skeleton rigid structure of $Na_{1+x}Zr_2P_{3-x}Si_xO_{12}$ system was extensively studied as potential candidate for solid state electrolyte in sodium sulfur battery.[80] At the optimized composition, this structure exhibits super ionic conductivity, and therefore is named as NA Super Ionic CONductor (NASICON)-type structure.

After a decade, NASICON-type structure with formula of $Fe_2(XO_4)_3$ (X = Mo, W, and S) was reported as lithium intercalation materials.[81,82] Intriguingly, an Fe^{3+}/Fe^{2+} redox potential of $Fe_2(SO_4)_3$ is much higher for ~0.6 V than those of $Fe_2(MoO_4)_3$ and $Fe_2(WO_4)_3$ phases. This potential upshifting can be explained by "inductive effect", which shows higher electronegativity of X makes redox potential higher.[82] The electronegative X anions form strong covalent X-O bond, thereby making Fe-O bond more ionic through Fe-O-X bonds. As illustrated in Fig. 1.4, the energy level of antibonding orbital corresponds to the redox potential of Fe^{3+}/Fe^{2+}. The higher redox potential is caused by deeper energy level of antibonding orbital due to less hybridization between iron and oxygen ions.

The inductive effect is widely accepted concept nowadays, thereby phosphates and sulfates are targeted in the preset study due to their higher electronegativity (P: 2.19, S: 2.58) and expected higher redox potentials. Lithium iron phosphate, and series of iron sulfates will be introduced in the following sections.

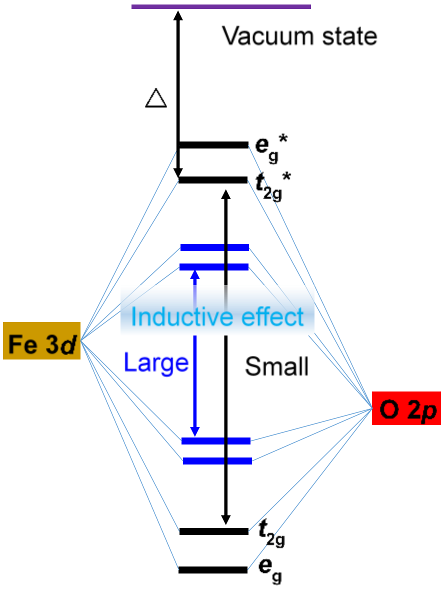

Figure 1.4 Schematic energy diagrams for bonding and antibonding orbitals with large and small inductive effects.

1.2.2.1 Olivine lithium iron phosphate

Lithium iron phosphate, Li_xFePO_4 is one of the most promising cathode materials for large-scale application.[83,84] Li_xFePO_4 electrode delivers specific capacity of ca. 160 $mAhg^{-1}$ (theoretical capacity: 169 $mAhg^{-1}$) with an operating voltage at ca. 3.4 V versus. Li/Li^+.[83,85] Another important aspect of $LiFePO_4$ and its delithiated phase $FePO_4$, "heterosite", are the high thermal stability at high temperature, which greatly contributes to reducing the safety risks of Li-ion batteries due to the strong bond between oxygen and phosphorus atoms.[84]

$LiFePO_4$ is isostructure to one of the minerals, olivine Mg_2SiO_4. Following the way in battery community, $LiFePO_4$ will be referred as olivine $LiFePO_4$, hereafter (although $LiFePO_4$ itself is a mineral named triphylite). The crystal structure of olivine $LiFePO_4$ is illustrated in Fig. 1.5. The olivine $LiFePO_4$ has orthorhombic *Pnma* symmetry (No. 62), where the general formula is described as $M1M2XO_4$ (M = alkaline or transition metals). In this formula, lithium, iron, and phosphorous ions correspond to $M1$ (4*a*), $M2$ (4*c*), and X (4*c*), respectively (Wyckoff positions are shown in brackets).

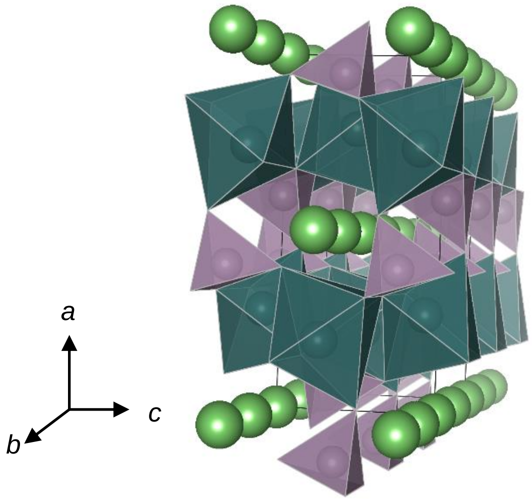

Figure 1.5 Crystal structure of olivine $LiFePO_4$ projected along the *b* axis. Li ions, FeO_6, and PO_4-units are shown in light green spheres, deep green octahedra, and light purple tetrahedra, respectively.

Lithium ion on 4*a* site diffuses along the *b* direction through a face-shared tetrahedral interstitial site.[86] The *ab-initio* calculations[87,88] showed the lowest activation energy (ca. 0.27 eV) for lithium diffusion along the *b* direction, while the crooked lithium diffusion pathways was experimentally visualized by combining high-temperature powder neutron diffraction and the maximum entropy method (MEM).[89]

As a lithium insertion compound, electrochemical processes of Li_xFePO_4 are commonly described as a two-phase reaction between Li-rich $Li_{1-\beta}FePO_4$ and Li-poor $Li_{\alpha}FePO_4$ phases.[4,83,85] The electrochemical reaction can be described as,

$$Li_{1-\beta}FePO_4 \rightarrow (1-x)Li_{1-\beta}FePO_4 + x\,Li_{\alpha}FePO_4 + x\,Li^+ + x\,e^- \quad (1.?).$$

Generally, two phase reaction should have relatively low kinetics due to poor electric conductivities ($< 10^{-9}$ Scm^{-2}) of end-members. However, this is counter-intuitive for the excellent rate performance of the optimized Li_xFePO_4 electrode.[90,91] Here, the revealed phase transformation mechanism of Li_xFePO_4 is summarized about (i) miscibility-gap shrinkage, (ii) one dimensional phase transformation, and (iii) non-equilibrium behavior in the following part.

(i) Miscibility-gap shrinkage

As is mentioned above, Li-rich and Li-poor phases are expected in their end members at finite temperature, which have a mixed valence state of Fe^{3+}/Fe^{2+}.[92–94] In the two-phase region ($Li_{\alpha}FePO_4$ + $Li_{1-\beta}FePO_4$), both Fe (II) and Fe (III) exist in each phase, which work as charge carriers to improve the electric conductivity during the charge/discharge processes. [92–94] In-detailed analyses revealed that the solid solution regions expand with decreasing particle sizes.[95–97] Phase field simulations supported the shrinkage of miscibility gap, and suggested it is originated to the diffuse interphase between Li-rich and Li-poor phases. [98,99]

(ii) One dimensional phase transformation

During the two reaction between the Li-rich and Li-poor phases, phase boundaries were observed along the *bc* plane, which moves along the *a* direction.[100–102] With considering multiple particles, lithium ions accommodate between particles to form single-phase particles without phase boundaries.[103–105] The process is thermodynamically preferable in the case that the particles have size-distribution or electrochemical connection each other, which are quite common in practical porous electrode.[103–105] Due to the spontaneous accommodation over particles, it is indispensable to conduct analyses under the battery operations.

(iii) Non-equilibrium behavior

More recently, a thermodynamic calculation suggested a single-phase transformation path at very low overpotential (ca. 30 meV) is possible, and this is why $LiFePO_4$ shows reasonable rate capability as a cathode.[106,107] The Li_xFePO_4 system might be an example where the kinetic transformation path between Li-rich and Li-poor phases is fundamentally different from the path deduced from its equilibrium phase diagram.[108] More recently, in situ neutron and synchrotron diffraction measurements supported the proposed phenomenon.[109–113] Simulation for the in situ XRD patterns suggested enlargements of diffuse interface between Li-rich and Li-poor phases under non-equilibrium conditions.[112]

1.2.2.2 Sulfate-based compounds

Followed by commercial success of olivine $LiFePO_4$, many of other oxyanionic compounds have been surveyed as cathode candidates for the future rechargeable batteries. Utilization of the SO_4^{2-} units is one of the most effective way to increase the redox potential owing to the strong inductive effect of the sulfur ion, which was mentioned in the section 1.2. Sulfate compounds typically generate high redox potentials for Fe^{3+}/Fe^{2+} (at 3.6–3.9 V versus. Li/Li^+). Structure types and electrode performances of reported lithium intercalation sulfate-based compounds are shown in Table 1.1.

Table 1.1 Structure types and electrochemical performances of reported sulfate-based compounds

composition	Structure type	space group	Potential / V vs. Li/Li$^+$	Capacity / mAhg^{-1}
$LiFeSO_4F$[114]	tavorite	triclinic P-1	3.6	140
$LiFeSO_4F$[115]	triplite	monoclinic $C2/c$	3.9	130
$LiFeSO_4OH$[116]	layered	monoclinic $P2_1/c$	3.6	120
$Li_2Fe(SO_4)_2$[117]	marinite	monoclinic $P2_1/c$	3.83	95
$Li_2Fe(SO_4)_2$[118]	-	orthorhombic $Pbca$	3.73 and 3.85	90
$FeSO_4OH$[119,120]	maxwellite	monoclinic $C2/c$	3.2	110
$(K)FeSO_4F$[121]	potasium tatanyl phosphate (KTP)	orthorhombic $Pna2_1$	3.7	130
$Fe_2(SO_4)_3$[82]	NASICON	monoclinic $P2_1/n$	3.6	100
$Fe_2(SO_4)_3$[122]	mikasite (NASICON-related)	rhombohedral R-3	3.55	60
$Fe_2O(SO_4)_2$[123]	-	monoclinic $I2/m$	3.0	125

Looking back at the 1980-1990s, electrochemical activities for sulfate-based compounds were reported for NASICON-type $Fe_2(SO_4)_3$.[82,124,125] However, the pristine $Fe_2(SO_4)_3$ phase does not include inherent sodium ions within the structure and its initial valence state of iron is Fe(III), which are not applicable for the cathode in ‘ion’ batteries.

After two decades, tavorite $LiFe(II)SO_4F$ was reported as an electrochemically active sulfate-based material, which exhibits a high redox potential at 3.6 V with reversible capacity of 140 mAhg^{-1}(i.e. 90 % of the theoretical capacity: 151 mAhg^{-1}).[114] Due to metastability of the phase, soft-chemical synthetic roots were essential for the synthesis of this compound.[114,120] The ionothermal method was originally applied with cost-expensive ionic liquids, such as 1-ethyl-3-methlimidazolium bis(trifluoromethylsulfonyl) amide (EMI-TFSA), followed by a solvothermal method with tetraethylene glycol as a reacting media.[126] The tavorite $LiFeSO_4F$ is an isostructure of $LiMgSO_4F$, which has triclinic P–1 symmetry. Within the structure, FeO_4F_2 octahedra are liked by corner sharing mode, forming $[Fe_6O_4F_2]_\infty$.These are bridged with SO_4^{2-} units and forms 3D open framework as illustrated in Fig. 1.6. DFT calculation predicted the tavorite $LiFeSO_4F$ is a fast 3D lithium ion conductor with low migration barrier (ca. 0.4 eV) along [100], [010], and [111] direction.[127] Upon delithiation process, two phase reaction takes place involving slightly large volume change ($\Delta V/V = 8.6$ %) with structure distortion from triclinic P–1 to monoclinic $C2/c$ symmetry.[114]

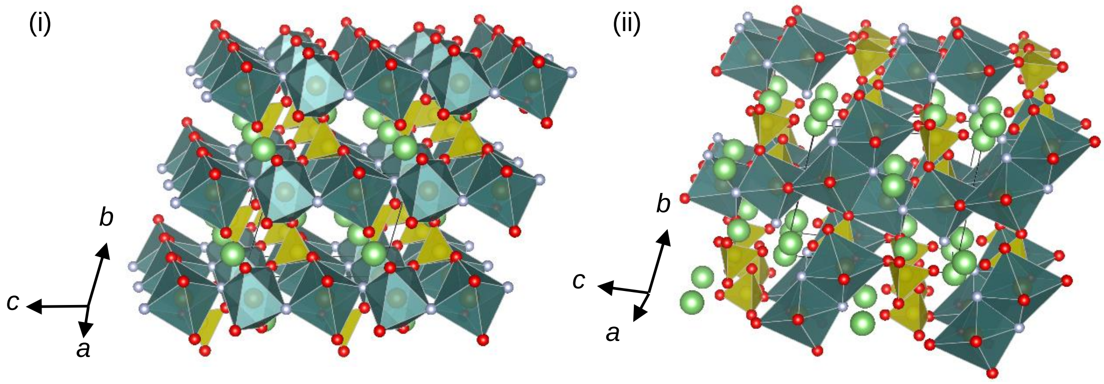

Figure 1.6 The crystal structures of (i) tavorite and (ii) triplite $LiFeSO_4F$ phases. Lithium, oxygen, and fluorine ions are illustrated in light green, red, and grey colors, respectively. FeO_4F_2 octahedra, and SO_4 tetrahedra are colored in deep green, and yellow.

A thermodynamically more stable polymorph, triplite $LiFeSO_4F$, was reported as a promising cathode candidate soon after.[115,128] The triplite phase can be obtained from several synthetic roots, such as low temperature solid-state (< 300 °C), solvothermal, spark plasma, microwave-assisted, and mechanical milling syntheses.[129–131] The crystal structure belongs to a family of triplite with formula: $(Mn,Fe)_2PO_4(F, OH)$, which has a monoclinic $C2/c$ lattice. Two distinctive Fe sites occupy octahedral sites within FeO_4F_2 units, which are bridged by edge-sharing configuration and forms edge-sharing chains along the [101] and [010] directions. The triplite phase exhibits extremely high redox potential at ca. 3.9 V versus Li/Li^+ with net capacity of 100 $mAhg^{-1}$. However, unlike the tavorite phase, the rate performance of the triplite phase is rather slow due to the distorted zigzag lithium migration pathways.

The reason why the triplite phase can offer higher redox potential than that of the tavorite phase (for ~0.3 V) is still under debate; the potential might be enhanced by (i) electrostatic repulsion between Fe^{3+}–Fe^{3+} at the dilithated phase due to close Fe-Fe distances within edge-sharing configuration, (ii) the repulsion between F ion at *trans* positions around Fe, and/or (iii) the inductive due to longer distance between metal and coordinated anions.[132–134]

The chemistry of fluorsulfate expanded to potassium metal sulfate compounds.[121] The $KFeSO_4F$ was reported as a relative of $KTiOPO_4$ (KTP) structure, which have orthorhombic unit cell with $Pna2_1$ symmetry. The FeO_4F_2 octahedra are connected with SO_4^{2-} units by corner-sharing manner, forming 3D open framework. $KFeSO_4F$ and potassium deintercalated derivative ($FeSO_4F_{KTP}$) show reversible capacities of with redox potentials at 4.0, 3.6, and 3.7 V versus K/K^+, Na/Na^+, and Li/Li^+, respectively. The larger ionic radius of K^+ (1.52 Å) assures the wide open channels, which can act as a suitable framework also for Li^+ and Na^+ intercalations, which can be a strategy for designing active cathode materials.[121] However, all of fluorsulfate compounds potentially have environmental and safety issues due to fluorine ions, which drive decomposition with moisture, producing strong HF acids.[135]

Exploration for fluorine-free sulfate compounds were conducted in this pursuit. Maxwellite $FeSO_4OH$ was reported as a potential cathode candidate.[119] The maxwellite phase was obtained by annealing $FeSO_4 \cdot 7H_2O$ for a week in air. The reversible capacity of 110 $mAhg^{-1}$ with the redox potential at 3.2 V versus Li/Li^+ were reported. More recently, layered-type $LiFeSO_4OH$, which was synthesized by a mechanical milling method was reported.[116] The layered-type $LiFeSO_4OH$ adopts monoclinic lattice with $P2_1/c$ symmetry. The edge-sharing FeO_6 octahedra forms zigzag chaings along *b*-axis. The DFT calculation showed 2D lithium-ion migration along *bc* plane with low activation energy of 0.2 eV, which is much smaller than that of maxwellite $FeSO_4OH$ (0.7 eV).[136] Furthermore, the layered phase operates a redox potential of 3.6 V with reversible net capacity of 120 $mAhg^{-1}$.[116] The obtained redox potential is slightly higher than that of maxwellite phase (3.2 V), might due to more stable lithiated and more unstable delithiated phases of the layered phase.

Another possibility for fluorine-free sulfates was proposed for bisulfate compounds. Marinate $Li_2Fe(SO_4)_2$ phase was reported as a 3.83 V class lithium battery cathode.[117] The marinate phase was synthesized via a low-temperature solid solution method (at ~300 ^{o}C) from anhydrous Li_2SO_4 and $FeSO_4$ compounds. The phase is isostructural to one of the minerals, “marinate”, which adopts monoclinic lattice with $P2_1/c$ symmetry. FeO_6 octahedra are isolated each other and linked with SO_4^{2-} anions in corner-sharing manner. One of the oxygens at the corner of SO_4^{2-} anions are coordinated toward open lithium tunnels. The marinate phase delivers a high redox potential at 3.83 V and 85 $mAhg^{-1}$ (i.e. 83 % of the theoretical capacity: 102 $mAhg^{-1}$) with large polarization. One of the origins for slow kinetics of the marinate $Li_2Fe(SO_4)_2$ can be large volume change for 12 % under the two-phase reaction mechanism.

Followed by the discovery of the marinate phase, a polymorph of $Li_2Fe(SO_4)_2$ was synthesized via a mechanical milling process.[118] The phase has a orthorhombic framework with *Pbca* symmetry. In the structure, isolated FeO_6 octahedra are bridged with SO_4^{2-} units by corner-sharing configuration, whereas one of the oxygen ions within the SO_4^{2-} units are coordinated to lithium ions in distorted tunnels along *b* axis as was also observed in the marinate phase. The reversible capacity of ~90 $mAhg^{-1}$ and two potential plateau at 3.73 and 3.85 V were obtained. In-situ XRD shows the electrochemical (de)lithiation process undergoes in two-phase reaction mechanism with volume change of ($\Delta V/V$ = ~6%).[118] Molecular dynamics calculation simulated the migration barrier for lithium migration is relatively low (0.33 eV) along the *a* axis, which might be the origin of superior rate performances than that of marinate phase.[137]

Recently, oxysulfate compounds $Fe_2O(SO_4)_2$ showed a new designing cocept for mixed anion systems. [123]Substitution of oxyanionic units with lighter oxygen ions can increase theoretical capacity in exchange with decrement of redox potential. This compound delivers reversible capacity of 125 $mAhg^{-1}$ with average potential at 3.0 V.

As for sodium battery cathode, α-$NaFeSO_4F$, bloedite $Na_2Fe(SO_4)_2{\cdot}4H_2O$, and kröhnkite $Na_2Fe(SO_4)_2{\cdot}2H_2O$ have been reported, but they are inactive or poorly active as sodium intercalation compounds (the specific capacities of ca. 6-70 $mAhg^{-1}$). [138–141]

More recently, eldfellite $NaFe(SO_4)_2$ was reported as 3 V class sodium intercalation material.[142] The phase adopt monoclinic lattice with $C12/m1$ symmetry. The FeO_6 octahedra are connected each other in edge-sharing mode, forming transition metal layers along the *ab* plane. These are connected with SO_4^{2-} units and sodium is placed at octahedral sites between the layers. This phase delivers reversible capacity of 78 $mAhg^{-1}$ with average voltage of 3.0 V versus Na/Na^+ under single phase reaction mechanism.[142]

Unlike the well-established phosphate (i.e. olivine Li_xFePO_4), practical impacts of sulfate-based compounds are limited so far. This is mainly due to common thermal/chemical instabilities of the sulfate-based compounds, which are not negligible issues; the sulfate compounds are (i) thermally unstable at around 350-400 ^oC, releasing SO_x gases, and (ii) hygroscopic at ambient condition, which should be solved for future commercial applications.

1.2.2.3 Other polyanionic compounds

Followed by studies for flurosulfate compounds, tavorite $LiFePO_4F$ was reported as possible lithium cathode material.[143] This phase delivers a reversible capacity of 145 $mAhg^{-1}$ with redox potential at 2.9 V under two phase reaction mechanism, involving ~8 % volume change. Subsequently, lithium metal pyrophosphate $Li_2MP_2O_7$ (M =Fe) was found to exhibit a high redox potential at 3.5 V with reversible capacity of 110 $mAhg^{-1}$.[144] Theoretically, the capacity would be more than 200 $mAhg^{-1}$ based on M^{4+}/M^{2+} redox, but is not achieved, so far. In this compound, substation of iron by the other 3*d* transition metal or inert alkaline metal enhanced the redox potential up to 4 V.[145,146] This may due to suppression of structural rearrangement upon the initial charging processes. Besides, sodium intercalation were reported for series of phosphates (e.g. olivine-Na_xFePO_4[147,148], NASICON-$Na_3V_2(PO_4)_3$[149], $Na_2FeP_2O_7$[150], $Na_4Fe_3(PO_4)_2(P_2O_7)$[151,152]), and fluorophospates (e.g. Na_2FePO_4F[153], $Na_{1.5}VPO_{4.8}F_{0.7}$[154,155], $Na_3V_2(PO_4)_2F_3$[156–158]).

Recently, alluaudite $NaMnFe_2(PO_4)_3$ forms a new class of possible cathode candidates both for lithium- and sodium-ion batteries.[159] The compound is isostructural to the mineral "alluaudite", which has general formula of $AA'BM_2(XO_4)_3$ with monoclinic lattice under $C2/c$ symmetry.[160] In the general formula, each ions correspond to A = Na1, A' = Na2, and B =Mn, M = Fe, and X = P. As illustrated in Fig. 1.7, FeO_6 octahedra are connected with another octahedral by an edge-sharing configuration, forming Fe_2O_{10} dimers. This dimer is isolated each other and linked by MnO_6 octahedra in edge-sharing mode, and by PO_4^{3-} tetrahedra in corner-sharing mode, building 3D skeleton structure. The structure has two distinctive tunnels along *c* axis for 1D sodium migration. Initially, the reported electrochemical property was poor (30, and 80 $mAhg^{-1}$ for solid-state, and sol-gel synthesized sample, respectively), but improved electrochemical performances were reported for $NaM_3(PO_4)_3$ (M = Mn, and Fe) as cathode for lithium-ion battery.[161,162]

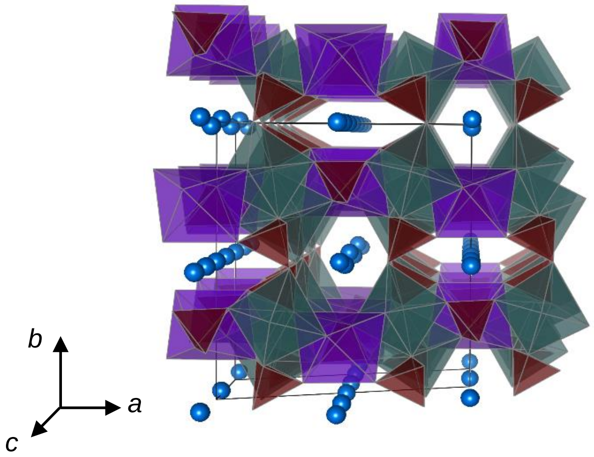

Figure 1.7 Crystal structure of alluaudite $NaMnFe_2(PO_4)_3$ projected along the *c* axis with two dinstictive Na^+ (blue spheres) channels. Green, purple, and brown polyhedra indicate FeO_6, MnO_6 and PO_4 units, respectively.

1.3 Purpose of this study

Currently, rechargeable batteries are under usage in wide variety of application, and it is indispensable to seek possibilities over types of rechargeable batteries for their future applications under the unwavering strategy. Here, the author has focused on exploring electrode candidates and understanding their reaction mechanisms, which are the two “pillars” for continuous development. The present thesis will focus on following topics:

1. Kinetics of nucleation and growth in two-phase reaction of olivine Li_xFePO_4,
2. The possibility of heterosite $FePO_4$ as a magnesium battery cathode,
3. Synthesis and electrochemical properties of alluaudite sodium iron sulfate,
4. Composition and crystal structure of alluaudite sodium iron sulfate,
5. Electrochemical reaction mechanism of alluaudite sodium iron sulfate,
6. Electronic structure of alluaudite sodium iron sulfate.

Overall, the present thesis contributes to the strategies for designing superior iron based cathode materials regardless of the types of batteries. These will be discussed in General Conclusion and Future Perspectives.

References

(1) Van Noorden, R. *Nature* **2014**, *507*, 26–28.

(2) Oshima, T.; Kajita, M.; Okuno, A. *Int. J. Appl. Ceram. Technol.* **2005**, *1*, 269–276.

(3) Bones, R. J. *J. Electrochem. Soc.* **1989**, *136*, 1274.

(4) Goodenough, J. B.; Park, K.-S. *J. Am. Chem. Soc.* **2013**, *135*, 1167–1176.

(5) Armand, M.; Tarascon, J.-M. *Nature* **2008**, *451*, 652–657.

(6) Mizushima, K.; Jones, P. C.; Wiseman, P. J.; Goodenough, J. B. *Mater. Res. Bull.* **1980**, *15*, 783–789.

(7) Yoshino, A.; Sanechika, K.; Nakajima, T. Secondary battery. USRE34991 E, July 4, 1985.

(8) Yazami, R.; Touzain, P. *J. Power Sources* **1983**, *9*, 365–371.

(9) Nishi, Y.; Azuma, H.; Omaru, A. Non aqueous electrolyte cell. 4959281, 1989.

(10) Yamada, A. *MRS Bull.* **2014**, *39*, 423–428.

(11) Whittingham, M. S. *Science* **1976**, *192*, 1126–1127.

(12) Whittingham, M. S. *Mater. Res. Bull.* **1974**, *9*, 1681–1689.

(13) Delmas, C.; Braconnier, J.; Fouassier, C.; Hagenmuller, P. *Solid State Ionics* **1981**, *3-4*, 165–169.

(14) Molenda, J.; Delmas, C.; Hagenmuller, P. *Solid State Ionics* **1983**, *9-10*, 431–435.

(15) Okoshi, M.; Yamada, Y.; Yamada, A.; Nakai, H. *J. Electrochem. Soc.* **2013**, *160*, A2160–A2165.

(16) Ong, S. P.; Chevrier, V. L.; Hautier, G.; Jain, A.; Moore, C.; Kim, S.; Ma, X.; Ceder, G. *Energy Environ. Sci.* **2011**, *4*, 3680.

(17) Komaba, S.; Murata, W.; Ishikawa, T.; Yabuuchi, N.; Ozeki, T.; Nakayama, T.; Ogata, A.; Gotoh, K.; Fujiwara, K. *Adv. Funct. Mater.* **2011**, *21*, 3859–3867.

(18) Stevens, D. A.; Dahn, J. R. *J. Electrochem. Soc.* **2000**, *147*, 1271.

(19) Oh, S.-M.; Hwang, J.-Y.; Yoon, C. S.; Lu, J.; Amine, K.; Belharouak, I.; Sun, Y.-K. *ACS Appl. Mater. Interfaces* **2014**, *6*, 11295–11301.

(20) Wang, Y.; Yu, X.; Xu, S.; Bai, J.; Xiao, R.; Hu, Y.-S.; Li, H.; Yang, X.-Q.; Chen, L.; Huang, X. *Nat. Commun.* **2013**, *4*.

(21) Senguttuvan, P.; Rousse, G.; Seznec, V.; Tarascon, J.-M.; Palacín, M. R. *Chem. Mater.* **2011**, *23*, 4109–4111.

(22) Qian, J.; Wu, X.; Cao, Y.; Ai, X.; Yang, H. *Angew. Chem. Int. Ed. Engl.* **2013**, *52*, 4633–4636.

(23) Yu, D. Y. W.; Prikhodchenko, P. V; Mason, C. W.; Batabyal, S. K.; Gun, J.; Sladkevich, S.; Medvedev, A. G.; Lev, O. *Nat. Commun.* **2013**, *4*, 2922.

(24) Qu, B.; Ma, C.; Ji, G.; Xu, C.; Xu, J.; Meng, Y. S.; Wang, T.; Lee, J. Y. *Adv. Mater.* **2014**, *26*, 3854–3859.

(25) Li, W.; Chou, S.-L.; Wang, J.-Z.; Kim, J. H.; Liu, H.-K.; Dou, S.-X. *Adv. Mater.* **2014**, *26*, 4037–4042.

(26) Ghidiu, M.; Lukatskaya, M. R.; Zhao, M.-Q.; Gogotsi, Y.; Barsoum, M. W. *Nature* **2014**, *516*, 78–81.

(27) Wang, X.; Kajiyama, S.; Iinuma, H.; Hosono, E.; Oro, S.; Moriguchi, I.; Okubo, M.; Yamada, A. *Nat. Commun.* **2015**, *6*, 6544.

(28) Ponrouch, A.; Dedryvère, R.; Monti, D.; Demet, A. E.; Ateba Mba, J. M.; Croguennec, L.; Masquelier, C.; Johansson, P.; Palacín, M. R. *Energy Environ. Sci.* **2013**, *6*, 2361.

(29) Ponrouch, A.; Marchante, E.; Courty, M.; Tarascon, J.-M.; Palacín, M. R. *Energy Environ. Sci.* **2012**, *5*, 8572.

(30) Komaba, S.; Ishikawa, T.; Yabuuchi, N.; Murata, W.; Ito, A.; Ohsawa, Y. *ACS Appl. Mater. Interfaces* **2011**, *3*, 4165–4168.

(31) Yoo, H. D.; Shterenberg, I.; Gofer, Y.; Gershinsky, G.; Pour, N.; Aurbach, D. *Energy Environ. Sci.* **2013**, *6*, 2265.

(32) Muldoon, J.; Bucur, C. B.; Oliver, A. G.; Sugimoto, T.; Matsui, M.; Kim, H. S.; Allred, G. D.; Zajicek, J.; Kotani, Y. *Energy Environ. Sci.* **2012**, *5*, 5941.

(33) Mohtadi, R.; Matsui, M.; Arthur, T. S.; Hwang, S.-J. *Angew. Chem. Int. Ed. Engl.* **2012**, *51*, 9780–9783.

(34) Saha, P.; Datta, M. K.; Velikokhatnyi, O. I.; Manivannan, A.; Alman, D.; Kumta, P. N. *Prog. Mater. Sci.* **2014**, *66*, 1–86.

(35) Gummow, R. J.; He, Y. *J. Electrochem. Soc.* **2010**, *157*, E45.

(36) Matsui, M. *J. Power Sources* **2011**, *196*, 7048–7055.

(37) Ling, C.; Banerjee, D.; Matsui, M. *Electrochim. Acta* **2012**, *76*, 270–274.

(38) Lu, Z.; Schechter, A.; Moshkovich, M.; Aurbach, D. *J. Electroanal. Chem.* **1999**, *466*, 203–217.

(39) Genders, J. D.; Pletcher, D. *J. Electroanal. Chem. Interfacial Electrochem.* **1986**, *199*, 93–100.

(40) Brown, O. R.; McIntyre, R. *Electrochim. Acta* **1985**, *30*, 627–633.

(41) Aurbach, D.; Lu, Z.; Schechter, A.; Gofer, Y.; Gizbar, H.; Turgeman, R.; Cohen, Y.; Moshkovich, M.; Levi, E. *Nature* **2000**, *407*, 724–727.

(42) Shao, Y.; Liu, T.; Li, G.; Gu, M.; Nie, Z.; Engelhard, M.; Xiao, J.; Lv, D.; Wang, C.; Zhang, J.-G.; Liu, J. *Sci. Rep.* **2013**, *3*, 3130.

(43) Mohtadi, R.; Mizuno, F. *Beilstein J. Nanotechnol.* **2014**, *5*, 1291–1311.

(44) Orikasa, Y.; Masese, T.; Koyama, Y.; Mori, T.; Hattori, M.; Yamamoto, K.; Okado, T.; Huang, Z.-D.; Minato, T.; Tassel, C.; Kim, J.; Kobayashi, Y.; Abe, T.; Kageyama, H.; Uchimoto, Y. *Sci. Rep.* **2014**, *4*, 5622.

(45) Hughbanks, T.; Hoffmann, R. *J. Am. Chem. Soc.* **1983**, *105*, 1150–1162.

(46) Aurbach, D.; Suresh, G. S.; Levi, E.; Mitelman, A.; Mizrahi, O.; Chusid, O.; Brunelli, M. *Adv. Mater.* **2007**, *19*, 4260–4267.

(47) Levi, E.; Gofer, Y.; Aurbach, D. *Chem. Mater.* **2010**, *22*, 860–868.

(48) Levi, E.; Levi, M. D.; Chasid, O.; Aurbach, D. *J. Electroceramics* **2007**, *22*, 13–19.

(49) Taniguchi, K.; Yoshino, T.; Gu, Y.; Katsura, Y.; Takagi, H. *J. Electrochem. Soc.* **2014**, *162*, A198–A202.

(50) Zhang, R.; Mizuno, F.; Ling, C. *Chem. Commun.* **2015**, *51*, 1108–1111.

(51) Imamura, D.; Miyayama, M.; Hibino, M.; Kudo, T. *J. Electrochem. Soc.* **2003**, *150*, A753.

(52) Le, D. B.; Passerini, S.; Coustier, F.; Guo, J.; Soderstrom, T.; Owens, B. B.; Smyrl, W. H. *Chem. Mater.* **1998**, *10*, 682–684.

(53) Mizuno, Y.; Okubo, M.; Hosono, E.; Kudo, T.; Oh-ishi, K.; Okazawa, A.; Kojima, N.; Kurono, R.; Nishimura, S.; Yamada, A. *J. Mater. Chem. A* **2013**, *1*, 13055.

(54) Wang, R. Y.; Wessells, C. D.; Huggins, R. A.; Cui, Y. *Nano Lett.* **2013**, *13*, 5748–5752.

(55) Bruce, P. G.; Krok, F.; Nowinski, J.; Gibson, V. C.; Tavakkoli, K. *J. Mater. Chem.* **1991**, *1*, 705.

(56) Liang, Y.; Feng, R.; Yang, S.; Ma, H.; Liang, J.; Chen, J. *Adv. Mater.* **2011**, *23*, 640–643.

(57) NuLi, Y.; Yang, J.; Li, Y.; Wang, J. *Chem. Commun.* **2010**, *46*, 3794.

(58) NuLi, Y.; Zheng, Y.; Wang, Y.; Yang, J.; Wang, J. *J. Mater. Chem.* **2011**, *21*, 12437.

(59) Sutto, T. E.; Duncan, T. T. *Electrochim. Acta* **2012**, *79*, 170–174.

(60) Sutto, T. E.; Duncan, T. T. *Electrochim. Acta* **2012**, *80*, 413–417.

(61) Tao, Z.-L.; Xu, L.-N.; Gou, X.-L.; Chen, J.; Yuan, H.-T. *Chem. Commun.* **2004**, 2080.

(62) Zhang, R.; Yu, X.; Nam, K.-W.; Ling, C.; Arthur, T. S.; Song, W.; Knapp, A. M.; Ehrlich, S. N.; Yang, X.-Q.; Matsui, M. *Electrochem. commun.* **2012**, *23*, 110–113.

(63) Rasul, S.; Suzuki, S.; Yamaguchi, S.; Miyayama, M. *Electrochim. Acta* **2012**, *82*, 243–249.

(64) Whittingham, M. S.; Gamble, F. R. *Mater. Res. Bull.* **1975**, *10*, 363–371.

(65) Amatucci, G. G. *J. Electrochem. Soc.* **1996**, *143*, 1114.

(66) Reimers, J. N. *J. Electrochem. Soc.* **1992**, *139*, 2091.

(67) Braconnier, J. J.; Delmas, C.; Hagenmuller, P. *Mater. Res. Bull.* **1982**, *17*, 993–1000.

(68) Komaba, S.; Takei, C.; Nakayama, T.; Ogata, A.; Yabuuchi, N. *Electrochem. commun.* **2010**, *12*, 355–358.

(69) Mendiboure, A.; Delmas, C.; Hagenmuller, P. *J. Solid State Chem.* **1985**, *57*, 323–331.

(70) Ma, X.; Chen, H.; Ceder, G. *J. Electrochem. Soc.* **2011**, *158*, A1307.

(71) Takeda, Y.; Nakahara, K.; Nishijima, M.; Imanishi, N.; Yamamoto, O.; Takano, M.; Kanno, R. *Mater. Res. Bull.* **1994**, *29*, 659–666.

(72) Yabuuchi, N.; Yoshida, H.; Komaba, S. *Electrochemistry* **2012**, *80*, 716–719.

(73) Vassilaras, P.; Ma, X.; Li, X.; Ceder, G. *J. Electrochem. Soc.* **2012**, *160*, A207–A211.

(74) Wang, X.; Liu, G.; Iwao, T.; Okubo, M.; Yamada, A. *J. Phys. Chem. C* **2014**, *118*, 2970–2976.

(75) Mortemard de Boisse, B.; Cheng, J.-H.; Carlier, D.; Guignard, M.; Pan, C.-J.; Bordère, S.; Filimonov, D.; Drathen, C.; Suard, E.; Hwang, B.-J.; Wattiaux, A.; Delmas, C. *J. Mater. Chem. A* **2015**, *3*, 10976–10989.

(76) Berthelot, R.; Carlier, D.; Delmas, C. *Nat. Mater.* **2011**, *10*, 74–80.

(77) Yabuuchi, N.; Kajiyama, M.; Iwatate, J.; Nishikawa, H.; Hitomi, S.; Okuyama, R.; Usui, R.; Yamada, Y.; Komaba, S. *Nat. Mater.* **2012**, *11*, 512–517.

(78) Mortemard de Boisse, B.; Carlier, D.; Guignard, M.; Delmas, C. *J. Electrochem. Soc.* **2013**, *160*, A569–A574.

(79) Buchholz, D.; Chagas, L. G.; Winter, M.; Passerini, S. *Electrochim. Acta* **2013**, *110*, 208–213.

(80) Goodenough, J. B.; Hong, H. .-P.; Kafalas, J. A. *Mater. Res. Bull.* **1976**, *11*, 203–220.

(81) Manthiram, A.; Goodenough, J. B. *J. Solid State Chem.* **1987**, *71*, 349–360.

(82) Manthiram, A.; Goodenough, J. B. *J. Power Sources* **1989**, *26*, 403–408.

(83) Padhi, A. K.; Nanjundaswamy, K. S.; Goodenough, J. B. *J. Electrochem. Soc.* **1997**, *144*, 1188–1193.

(84) Yamada, A.; Chung, S. C.; Hinokuma, K. *J. Electrochem. Soc.* **2001**, *148*, A224.

(85) Padhi, A. K.; Nanjundaswamy, K. S.; Masquelier, C.; Okada, S.; Goodenough, J. B. *J. Electrochem. Soc.* **1997**, *144*, 1609.

(86) Amin, R.; Maier, J.; Balaya, P.; Chen, D. P.; Lin, C. T. *Solid State Ionics* **2008**, *179*, 1683–1687.

(87) Morgan, D.; Van der Ven, A.; Ceder, G. *Electrochem. Solid-State Lett.* **2004**, *7*, A30.

(88) Islam, M. S.; Driscoll, D. J.; Fisher, C. A. J.; Slater, P. R. *Chem. Mater.* **2005**, *17*, 5085–5092.

(89) Nishimura, S.; Kobayashi, G.; Ohoyama, K.; Kanno, R.; Yashima, M.; Yamada, A. *Nat. Mater.* **2008**, *7*, 707–711.

(90) Yamada, A.; Yonemura, M.; Takei, Y.; Sonoyama, N.; Kanno, R. *Electrochem. Solid-State Lett.* **2005**, *8*, A55.

(91) Kang, B.; Ceder, G. *Nature* **2009**, *458*, 190–193.

(92) Srinivasan, V.; Newman, J. *J. Electrochem. Soc.* **2004**, *151*, A1517.

(93) Yamada, A.; Koizumi, H.; Nishimura, S.; Sonoyama, N.; Kanno, R.; Yonemura, M.; Nakamura, T.; Kobayashi, Y. *Nat. Mater.* **2006**, *5*, 357–360.

(94) Kobayashi, G.; Nishimura, S.; Park, M.-S.; Kanno, R.; Yashima, M.; Ida, T.; Yamada, A. *Adv. Funct. Mater.* **2009**, *19*, 395–403.

(95) Meethong, N.; Huang, H.-Y. S.; Speakman, S. A.; Carter, W. C.; Chiang, Y.-M. *Adv. Funct. Mater.* **2007**, *17*, 1115–1123.

(96) Meethong, N.; Huang, H.-Y. S.; Carter, W. C.; Chiang, Y.-M. *Electrochem. Solid-State Lett.* **2007**, *10*, A134.

(97) Kobayashi, G.; Yamada, A.; Nishimura, S.; Kanno, R.; Kobayashi, Y.; Seki, S.; Ohno, Y.; Miyashiro, H. *J. Power Sources* **2009**, *189*, 397–401.

(98) Singh, G. K.; Ceder, G.; Bazant, M. Z. *Electrochim. Acta* **2008**, *53*, 7599–7613.

(99) Burch, D.; Bazant, M. Z. *Nano Lett.* **2009**, *9*, 3795–3800.

(100) Chen, G.; Song, X.; Richardson, T. J. *Electrochem. Solid-State Lett.* **2006**, *9*, A295.

(101) Laffont, L.; Delacourt, C.; Gibot, P.; Wu, M. Y.; Kooyman, P.; Masquelier, C.; Tarascon, J. M. *Chem. Mater.* **2006**, *18*, 5520–5529.

(102) Delmas, C.; Maccario, M.; Croguennec, L.; Le Cras, F.; Weill, F. *Nat. Mater.* **2008**, *7*, 665–671.

(103) Lee, K. T.; Kan, W. H.; Nazar, L. F. *J. Am. Chem. Soc.* **2009**, *131*, 6044–6045.

(104) Gaberscek, M.; K?zma, M.; Jamnik, J. *Phys. Chem. Chem. Phys.* **2007**, *9*, 1815.

(105) Dreyer, W.; Jamnik, J.; Guhlke, C.; Huth, R.; Moškon, J.; Gaberšček, M. *Nat. Mater.* **2010**,

9, 448–453.

(106) Malik, R.; Zhou, F.; Ceder, G. *Nat. Mater.* **2011**, *10*, 587–590.

(107) Malik, R.; Abdellahi, A.; Ceder, G. *J. Electrochem. Soc.* **2013**, *160*, A3179–A3197.

(108) Bai, P.; Cogswell, D. A.; Bazant, M. Z. *Nano Lett.* **2011**, *11*, 4890–4896.

(109) Sharma, N.; Guo, X.; Du, G.; Guo, Z.; Wang, J.; Wang, Z.; Peterson, V. K. *J. Am. Chem. Soc.* **2012**, *134*, 7867–7873.

(110) Orikasa, Y.; Maeda, T.; Koyama, Y.; Murayama, H.; Fukuda, K.; Tanida, H.; Arai, H.; Matsubara, E.; Uchimoto, Y.; Ogumi, Z. *Chem. Mater.* **2013**, *25*, 1032–1039.

(111) Orikasa, Y.; Maeda, T.; Koyama, Y.; Murayama, H.; Fukuda, K.; Tanida, H.; Arai, H.; Matsubara, E.; Uchimoto, Y.; Ogumi, Z. *J. Am. Chem. Soc.* **2013**, *135*, 5497–5500.

(112) Liu, H.; Strobridge, F. C.; Borkiewicz, O. J.; Wiaderek, K. M.; Chapman, K. W.; Chupas, P. J.; Grey, C. P. *Science*, **2014**, *344*, 1252817.

(113) Zhang, X.; van Hulzen, M.; Singh, D. P.; Brownrigg, A.; Wright, J. P.; van Dijk, N. H.; Wagemaker, M. *Nano Lett.* **2014**, *14*, 2279–2285.

(114) Recham, N.; Chotard, J.-N.; Dupont, L.; Delacourt, C.; Walker, W.; Armand, M.; Tarascon, J.-M. *Nat. Mater.* **2010**, *9*, 68–74.

(115) Barpanda, P.; Ati, M.; Melot, B. C.; Rousse, G.; Chotard, J.-N.; Doublet, M.-L.; Sougrati, M. T.; Corr, S. A.; Jumas, J.-C.; Tarascon, J.-M. *Nat. Mater.* **2011**, *10*, 772–779.

(116) Subban, C. V.; Ati, M.; Rousse, G.; Abakumov, A. M.; Van Tendeloo, G.; Janot, R.; Tarascon, J.-M. *J. Am. Chem. Soc.* **2013**, *135*, 3653–3661.

(117) Reynaud, M.; Ati, M.; Melot, B. C.; Sougrati, M. T.; Rousse, G.; Chotard, J.-N.; Tarascon, J.-M. *Electrochem. commun.* **2012**, *21*, 77–80.

(118) Lander, L.; Reynaud, M.; Rousse, G.; Sougrati, M. T.; Laberty-Robert, C.; Messinger, R. J.; Deschamps, M.; Tarascon, J.-M. *Chem. Mater.* **2014**, *26*, 4178–4189.

(119) Anji Reddy, M.; Pralong, V.; Caignaert, V.; Varadaraju, U. V.; Raveau, B. *Electrochem. commun.* **2009**, *11*, 1807–1810.

(120) Rousse, G.; Tarascon, J. M. *Chem. Mater.* **2014**, *26*, 394–406.

(121) Recham, N.; Rousse, G.; Sougrati, M. T.; Chotard, J.-N.; Frayret, C.; Mariyappan, S.; Melot, B. C.; Jumas, J.-C.; Tarascon, J.-M. *Chem. Mater.* **2012**, *24*, 4363–4370.

(122) Wu, Q.; Xu, Y.; Ju, H. *Ionics (Kiel).* **2012**, *19*, 471–475.

(123) Sun, M.; Rousse, G.; Abakumov, A. M.; Van Tendeloo, G.; Sougrati, M.-T.; Courty, M.; Doublet, M.-L.; Tarascon, J.-M. *J. Am. Chem. Soc.* **2014**, *136*, 12658–12666.

(124) Nanjundaswamy, K. S.; Padhi, A. K.; Goodenough, J. B.; Okada, S.; Ohtsuka, H.; Arai, H.; Yamaki, J. *Solid State Ionics* **1996**, *92*, 1–10.

(125) Padhi, A. K. *J. Electrochem. Soc.* **1998**, *145*, 1518.

(126) Tripathi, R.; Ramesh, T. N.; Ellis, B. L.; Nazar, L. F. *Angew. Chemie Int. Ed.* **2010**, *49*, 8738–8742.

(127) Tripathi, R.; Gardiner, G. R.; Islam, M. S.; Nazar, L. F. *Chem. Mater.* **2011**, *23*, 2278–

2284.

(128) LIU, L.; ZHANG, B.; HUANG, X. *Prog. Nat. Sci. Mater. Int.* **2011**, *21*, 211–215.

(129) Ati, M.; Sathiya, M.; Boulineau, S.; Reynaud, M.; Abakumov, A.; Rousse, G.; Melot, B.; Van Tendeloo, G.; Tarascon, J.-M. *J. Am. Chem. Soc.* **2012**, *134*, 18380–18387.

(130) Tripathi, R.; Popov, G.; Ellis, B. L.; Huq, A.; Nazar, L. F. *Energy Environ. Sci.* **2012**, *5*, 6238.

(131) Tripathi, R.; Popov, G.; Sun, X.; Ryan, D. H.; Nazar, L. F. *J. Mater. Chem. A* **2013**, *1*, 2990.

(132) Chung, S. C.; Barpanda, P.; Nishimura, S.; Yamada, Y.; Yamada, A. *Phys. Chem. Chem. Phys.* **2012**, *14*, 8678.

(133) Ben Yahia, M.; Lemoigno, F.; Rousse, G.; Boucher, F.; Tarascon, J.-M.; Doublet, M.-L. *Energy Environ. Sci.* **2012**, *5*, 9584.

(134) Melot, B. C.; Scanlon, D. O.; Reynaud, M.; Rousse, G.; Chotard, J.-N.; Henry, M.; Tarascon, J.-M. *ACS Appl. Mater. Interfaces* **2014**, *6*, 10832–10839.

(135) Barpanda, P. *Isr. J. Chem.* **2015**, *55*, 537–557.

(136) Eames, C.; Clark, J. M.; Rousse, G.; Tarascon, J.-M.; Islam, M. S. *Chem. Mater.* **2014**, *26*, 3672–3678.

(137) Islam, S.; Eames, C.; Clark, J.; Tarascon, J.-M.; Rousse, G.; Chotard, J.-N.; Reynaud, M. *J. Mater. Chem. A* **2014**.

(138) Reynaud, M.; Rousse, G.; Abakumov, A. M.; Sougrati, M. T.; Van Tendeloo, G.; Chotard, J.-N.; Tarascon, J.-M. *J. Mater. Chem. A* **2014**, *2*, 2671–2680.

(139) Ati, M.; Dupont, L.; Recham, N.; Chotard, J.-N. J. N.; Walker, W. T.; Davoisne, C.; Barpanda, P.; Sarou-Kanian, V.; Armand, M.; Tarascon, J.-M. J. M. *Chem. Mater.* **2010**, *22*, 4062–4068.

(140) Barpanda, P.; Chotard, J.-N.; Recham, N.; Delacourt, C.; Ati, M.; Dupont, L.; Armand, M.; Tarascon, J.-M. *Inorg. Chem.* **2010**, *49*, 7401–7413.

(141) Barpanda, P.; Oyama, G.; Ling, C. D.; Yamada, A. *Chem. Mater.* **2014**, *26*, 1297–1299.

(142) Singh, P.; Shiva, K.; Celio, H.; Goodenough, J. B. *Energy Environ. Sci.* **2015**, *8*, 3000–3005.

(143) Ramesh, T. N.; Lee, K. T.; Ellis, B. L.; Nazar, L. F. *Electrochem. Solid-State Lett.* **2010**, *13*, A43.

(144) Nishimura, S.; Nakamura, M.; Natsui, R.; Yamada, A. *J. Am. Chem. Soc.* **2010**, *132*, 13596–13597.

(145) Furuta, N.; Nishimura, S.; Barpanda, P.; Yamada, A. *Chem. Mater.* **2012**, *24*, 1055–1061.

(146) Ye, T.; Barpanda, P.; Nishimura, S.; Furuta, N.; Chung, S.-C.; Yamada, A. *Chem. Mater.* **2013**, *25*, 3623–3629.

(147) Moreau, P.; Guyomard, D.; Gaubicher, J.; Boucher, F. *Chem. Mater.* **2010**, *22*, 4126–4128.

(148) Lu, J.; Chung, S. C.; Nishimura, S.; Yamada, A. *Chem. Mater.* **2013**, 131029074415004.

(149) Saravanan, K.; Mason, C. W.; Rudola, A.; Wong, K. H.; Balaya, P. *Adv. Energy Mater.* **2013**, *3*, 444–450.

(150) Barpanda, P.; Liu, G.; Ling, C. D.; Tamaru, M.; Avdeev, M.; Chung, S.-C.; Yamada, Y.; Yamada, A. *Chem. Mater.* **2013**, 130826145907003.

(151) Kim, H.; Park, I.; Seo, D.-H.; Lee, S.; Kim, S.-W.; Kwon, W. J.; Park, Y.-U.; Kim, C. S.; Jeon, S.; Kang, K. *J. Am. Chem. Soc.* **2012**, *134*, 10369–10372.

(152) Kim, H.; Park, I.; Lee, S.; Kim, H.; Park, K.-Y.; Park, Y.-U.; Kim, H.; Kim, J.; Lim, H.-D.; Yoon, W.-S.; Kang, K. *Chem. Mater.* **2013**, *25*, 3614–3622.

(153) Ellis, B. L.; Makahnouk, W. R. M.; Makimura, Y.; Toghill, K.; Nazar, L. F. *Nat. Mater.* **2007**, *6*, 749–753.

(154) Sauvage, F.; Quarez, E.; Tarascon, J. M.; Baudrin, E. *Solid state Sci.* **2006**, *8*, 1215–1221.

(155) Park, Y.-U.; Seo, D.-H.; Kwon, H.-S.; Kim, B.; Kim, J.; Kim, H.; Kim, I.; Yoo, H.-I.; Kang, K. *J. Am. Chem. Soc.* **2013**, *135*, 13870–13878.

(156) Gover, R.; Bryan, A.; Burns, P.; Barker, J. *Solid State Ionics* **2006**, *177*, 1495–1500.

(157) Shakoor, R. A.; Seo, D.-H.; Kim, H.; Park, Y.-U.; Kim, J.; Kim, S.-W.; Gwon, H.; Lee, S.; Kang, K. *J. Mater. Chem.* **2012**, *22*, 20535.

(158) Liu, Z.; Hu, Y.-Y.; Dunstan, M. T.; Huo, H.; Hao, X.; Zou, H.; Zhong, G.; Yang, Y.; Grey, C. P. *Chem. Mater.* **2014**, *26*, 2513–2521.

(159) Trad, K.; Carlier, D.; Croguennec, L.; Wattiaux, A.; Ben Amara, M.; Delmas, C. *Chem. Mater.* **2010**, *22*, 5554–5562.

(160) Fisher, D. J. *Am. Mineral.* **1955**, *40*, 1100–1109.

(161) Kim, J.; Kim, H.; Park, K.-Y.; Park, Y.-U.; Lee, S.; Kwon, H.-S.; Yoo, H.-I.; Kang, K. *J. Mater. Chem. A* **2014**, *2*, 8632.

(162) Kim, J.; Kim, H.; Park, I.; Park, Y.-U.; Yoo, J.-K.; Park, K.-Y.; Lee, S.; Kang, K. *Energy Environ. Sci.* **2013**, *6*, 830.

Part I

Electrochemical behaviors of Olivine Lithium Iron Phosphate

2. Kinetics of Nucleation and Growth in Two-Phase Electrochemical Reaction of Li_xFePO_4

2.1 Introduction

Due to growing public concern about energy and environmental issues, lithium-ion batteries are increasing their presence in large-scale energy storage (e.g., electric-load leveling systems and power sources for automobiles) as well as in conventional small-scale use (e.g., cell phones and notebook computers). The emerging large-scale usage of lithium-ion batteries has imposed more and more strict criteria for their performance, service life, cost, and safety, among which the latter two are the key obstacles to the large-scale applications.[1] Hence, the use of conventional cobalt-based cathodes (e.g., $LiCoO_2$) is unrealistic because of the scarcity of Co resource and the structural instability (i.e., O_2 evolution at high state of charge). Facing the cost and safety challenges for large-scale lithium-ion batteries, researchers have been considering a new material-design strategy on the basis of constituent element and structural stability.

Olivine-type lithium iron phosphate, $LiFePO_4$, is gaining momentum as one of the most promising cathode materials for large-scale applications due to its low cost offered by abundant iron element as well as its high safety based on fixed oxygen by a strong P–O covalent bond.[2,3] Initially, the charge-discharge kinetics of $LiFePO_4$ was considered to be slow because of its insulating nature based on a two-phase electrochemical reaction between $LiFePO_4$ and $FePO_4$ with localized small polarons in each phase. Through progressive technological innovations, however, a leading-edge $LiFePO_4$ battery can deliver high power density of 10 kW kg^{-1} with almost full theoretical capacity (ca. 170 mAh g^{-1}),[4] by using nanoparticles, mixing conductive carbon, and/or doping aliovalent cations.[3-6] Motivated by the extraordinary two-phase kinetics of nanosized $LiFePO_4$, much effort has been made to study the mechanism of electrochemically-driven phase transition (i.e., nucleation and growth of a new phase) in both experimental and computational ways, clarifying i) the existence of Fe^{3+}/Fe^{2+} mixed-valent phases[7], Li-poor $Li_{\alpha}FePO_4$ and Li-rich $Li_{1-\beta}FePO_4$, during the two-phase reaction,[8] ii) small room-temperature miscibility gap for nanosized Li_xFePO_4,[9-10] iii) one-dimensional lithium diffusion along the [010] channel with the smallest activation energy,[11-13] and iv) one-dimensional phase-boundary movement like "domino cascade[14]" along the [100] direction with the smallest two-phase lattice misfit in the *bc* plane.[15,16] Despite the vigorous studies on the reaction mechanism through microscopy, X-ray/neutron diffraction method, and spectroscopy, there are few electrochemical analyses on the kinetics of phase transition in Li_xFePO_4. Behind this situation lies the difficulty of not only applying a suitable time-resolving technique but also adopting an appropriate experimental condition to accurately detect the dynamics of phase transition.

Potential-step chronoamperometry[17] is one of the most powerful techniques to investigate the kinetics of electrochemical phase transition, because the chronoamperogram (i.e., current *vs.* time plot) shows a clear sign of nucleation and growth; when the nucleation and growth govern the electrode kinetics, the current response shows momentary increase followed by gradual decline.[18] Using chronoamperometry, several researches have been conducted on the two-phase reaction of graphite with lithium.[19-22] For Li_xFePO_4, Allen et al. analyzed the chronoamperogram of the phase transition[23,24] by using Kolmogorov-Johnson-Mehl-Avrami (KJMA) theory,[25-27] a widely-accepted model applied to phase transition of metal. They reached the same conclusion as those presented thus far that the electrochemical phase transition of Li_xFePO_4 proceeds in a one-dimensional way.[15,16] Meethong et al. discussed the influences of particle size and aliovalent doping on the kinetics of Li_xFePO_4 by separating the contributions of Li diffusion and phase transition on the chronoamperograms.[28]

In this chapter, potential-step chronoamperometry was used to provide systematic information about the kinetics of electrochemical phase transition during lithiation and delithiation of Li_xFePO_4, including the effects of overpotential, particle size, and electrode thickness. Our work started from determining an appropriate experimental condition for investigating the kinetics of nucleation and growth, by identifying the factors that determine the two-phase reaction mechanism of Li_xFePO_4 under various experimental conditions. Next, chronoamperometry was conducted on Li_xFePO_4 particles under the optimized condition in which the nucleation and growth govern the electrode kinetics, and the current response was analyzed by using KJMA equation.[25-27] Finally, the activation energies of phase-boundary movement was evaluated during lithiation and delithiation from the temperature dependence of rate constant obtained by fitting the chronoamperograms with KJMA model.

2.2 Experimental methods

$LiFePO_4$ powders with different particle sizes were synthesized by a solid-state reaction from stoichiometric amounts of Li_2CO_3 (Wako, 99.0%), FeC_2O_4•$2H_2O$ (JUNSEI, 99%), and $(NH_4)_2HPO_4$ (Wako, 99.0%) as a starting material. The average particle size was controlled to around 45, 84, and 203 nm by altering sintering temperature, and milling condition. Detailed conditions are shown elsewhere.[10]

For characterization of the samples, X-ray diffraction (XRD) patterns were measured at room temperature using a Bruker AXS D8 ADVANCE powder diffractometer equipped with Co Kα radiation and a Vantec-1 linear position-sensitive detector. The X-ray tube current and voltage were set to 40 mA and 35 kV, respectively. Measurements were taken in the range from $2\theta=15^\circ$ to 120° with the sample-stage rotation at 30 rpm. Structural parameters were obtained by Rietveld refinement using Topas ver 3.0 program. The morphology and particle size of the synthesized $LiFePO_4$ powders were observed by a field-emission scanning electron microscope (FE-SEM, Hitachi S-4800).

For electrochemical measurements, $LiFePO_4$/C composite including 85 wt% $LiFePO_4$, 8 wt% carbon black (Ketjen Black, Lion Corp., ECP), and 2 wt% vapor-grown carbon fiber (VGCF, Showa Denko K. K.) was well-mixed with 5 wt % polyvinylidene fluoride (PVdF) in *N*-methylpyrrolidone (NMP, Wako). The slurry was uniformly spread on an aluminum current collector with a doctor blade and dried at 60 °C under vacuum for 6-10 hours. The obtained sheets were pressed onto aluminum mesh to form a 16-mmϕ disk electrode. Electrochemical measurements were carried out using 2032-type coin cells with Li metal anode. The electrolyte solution was 1 mol dm^{-3} $LiPF_6$ dissolved in a mixture of ethylene carbonate (EC) / diethyl carbonate (DEC) (3:7 by vol., Tomiyama Chemical). A polypropylene film was used as a separator. In advance to potential-step chronoamperometry, galvanostatic charge-discharge tests for two cycles were conducted over a potential range between 2.0 V and 4.5 V at C/20 rate by using TOSCAT-3100 charge-discharge unit (TOYO SYSTEM). Potential was relaxed down to C/200 rate at the end of the charging process (at 4.5 V) to get the full capacity. Potential-step chronoamperograms of the $LiFePO_4$ electrode were recorded with VMP-3 (Bio-Logic). A potential step was applied to cross the two-phase equilibrium potential in various experimental conditions: amplitude of potential step (150 mV or 10 mV), particle size of the $LiFePO_4$ particles (45 nm, 84 nm, or 203 nm), direction of potential step (anodic or cathodic), and thickness of composite electrode (1 μm or 10 μm).

2.3 Sample characterization

Synthesized samples were all single-phase $LiFePO_4$ with an ordered olivine structure of orthorhombic *Pnma* symmetry (Fig. 2.1 and Table 2.1). There were no impurities observed in the XRD patterns. The mean particle sizes were evaluated to be 45 nm, 84 nm, and 203 nm by two methods: direct observation by SEM (Fig. 2.2) and crystallite sizes from Rietveld refinement of XRD patterns using fundamental parameters analyses. In advance to potential-step chronoamperometry, charge-discharge measurements of the $LiFePO_4$ cells were conducted for two cycles to confirm their reversible capacity. All the $LiFePO_4$ samples showed reversible capacities close to the theoretical value (ca. 170 mAh g^{-1}), indicating that the synthesized $LiFePO_4$ samples were pure and contained a negligible amount of antisite defects. The charge-discharge profiles of the samples were characterized by a plateau at ca. 3.45 V vs. Li/Li^{+}, which corresponded to the equilibrium potential of two-phase reaction in Li_xFePO_4. In the potential profiles, the two-phase flat region (i.e., miscibility gap) narrowed with decreasing particle size, which was consistent with the previous literature.[9,10]

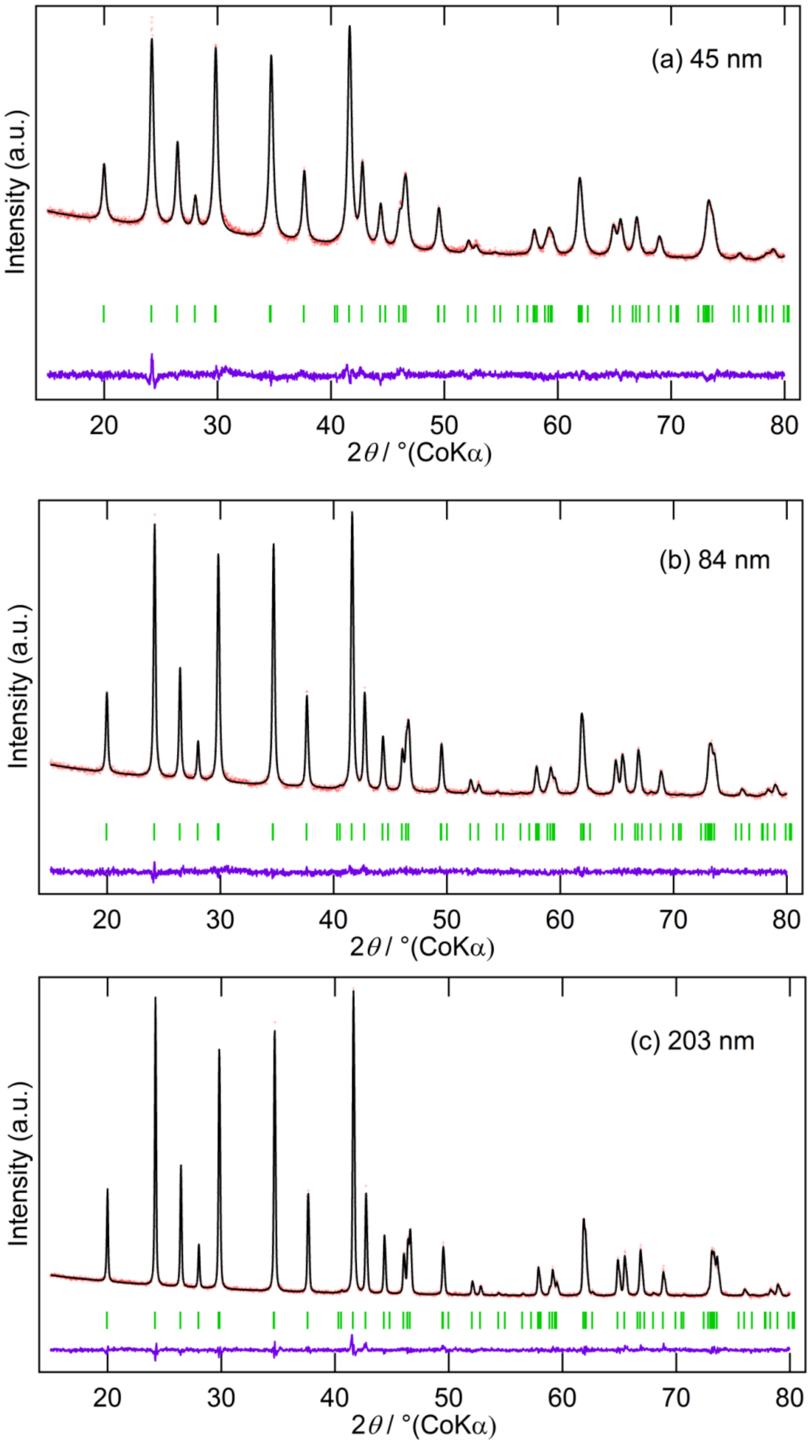

Figure 2.1 Rietveld refinement patterns of the X-ray diffraction data for synthesized $LiFePO_4$ with different particle sizes: (a) 45 nm, (b) 84 nm, and (c) 203 nm.

Table 2.1 Refined structural parameters of synthesized $LiFePO_4$ with different particle sizes.

(i) $LiFePO_4$ 44.5 (4) nm

Site	x	y	z	g	B_{eq}
Li	0	0	0	1	1
Fe	0.28219 (10)	0.25	0.9736 (3)	1	0.6
P	0.0963 (2)	0.25	0.4159 (5)	1	0.6
O1	0.0965 (4)	0.25	0.7450 (8)	1	1
O2	0.4513 (6)	0.25	0.2093 (5)	1	1
O3	0.1660 (3)	0.0424 (5)	0.2795 (5)	1	1

a = 10.3247 (5), b = 6.0012 (3), c = 4.696 (3) R_{exp} = 1.19, R_{wp} = 1.44, R_p = 1.14, GOF =1.20

(ii) $LiFePO_4$ 84.3 (8) nm

Site	x	y	z	g	B_{eq}
Li	0	0	0	1	1
Fe	0.28219 (10)	0.25	0.9736 (3)	1	0.6
P	0.0963 (2)	0.25	0.4159 (5)	1	0.6
O1	0.0965 (4)	0.25	0.7450 (8)	1	1
O2	0.4513 (6)	0.25	0.2093 (5)	1	1
O3	0.1660 (3)	0.0424 (5)	0.2795 (5)	1	1

a = 10.3234 (2), b = 6.00397 (12), c = 4.69389 (12), R_{exp} = 1.16, R_{wp} = 1.40, R_p = 1.12, GOF =1.21

(iii) $LiFePO_4$ 203 (4) nm

Site	x	y	z	g	B_{eq}
Li	0	0	0	1	1
Fe	0.28220 (11)	0.25	0.9748 (4)	1	0.6
P	0.0951 (2)	0.25	0.4171 (6)	1	0.6
O1	0.0991 (6)	0.25	0.74650 (12)	1	1
O2	0.4551 (7)	0.25	0.2072 (9)	1	1
O3	0.1672 (7)	0.0444 (9)	0.2830 (7)	1	1

a = 10.3254 (3), b = 6.00706 (14), c = 4.69307 (13), R_{exp} = 1.31, R_{wp} = 1.82, R_p = 1.40, GOF =1.39

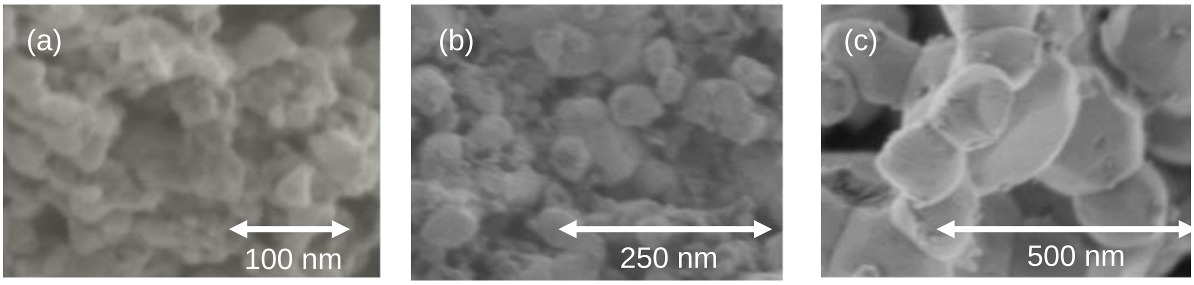

Figure 2.2 SEM images of synthesized $LiFePO_4$ with different particle sizes: (a) 45 nm, (b) 84 nm, and (c) 203 nm.

2.4 Chronoamperogram to analyze phase transformations

A chronoamperogram shows a characteristic "current hump" when the nucleation and growth in a bulk material dominate the electrode reaction (Fig. 2.3).[18] This behavior cannot be explained by Cottrell equation[17] which deals with only a diffusion process induced by the gradient of chemical potential. The characteristic current profile for nucleation and growth is generally interpreted as follows. The current drops sharply at the very beginning of the chronoamperogram, which is typical response for charging electric double layer at the electrode-electrolyte interface. Immediately, the current begins to increase at point a), which corresponds to the initiation of nucleation. The momentary current increase results from the increase in the number of two-phase boundaries (i.e., the planes where the new phase grows) in a Li_xFePO_4 particle, as shown in the inset of Fig. 2.3. Then, the current reaches a maximum at point b), which corresponds to the maximum number of the phase boundaries (i.e., minimum resistance to new-phase growth). Subsequently, the current shows monotonic decrease in a region from point b) to d), indicating that new phases merge with each other to form large domains. Such unique current response is also reported in the two-phase electrode reaction of lithium graphite intercalation compound (Li_xC_6)[18,21,22] and spinel lithium manganese oxide $Li_xMn_2O_4$.[29]

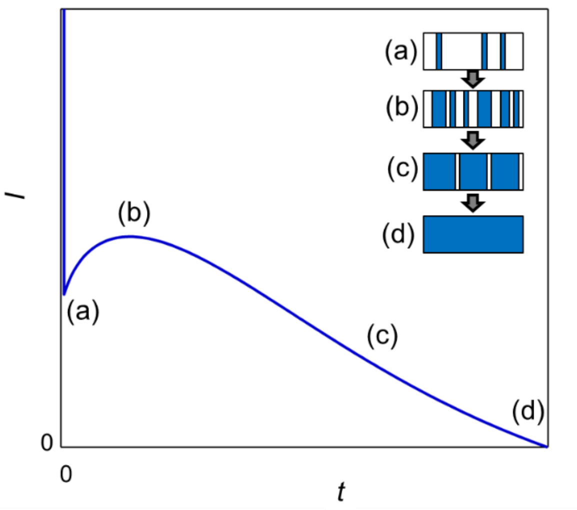

Figure 2.3 Schematic illustration of chronoamperogram that characterizes nucleation and growth in a two-phase electrochemical reaction. The inset indicates the picture of nucleation and growth in a particle: (a) initiation of nucleation, (b) maximum number of phase boundaries, (c) growth and merger, and (d) termination.

The characteristic chronoamperogram can be interpreted based on KJMA model,[23-27,29] which is an important theory that describes phase transformation in metal. KJMA equation gives the fraction of a new phase (f) as a function of time (t) as follows,

$$f = 1 - \exp(-kt^n) \quad (2.1),$$

where n is Avrami exponent and k is the rate constant of phase transformation. To analyze chronoamperograms, the KJMA equation is transformed to the following equation,[23,29]

$$I(t) = C\, t^{\,n-1} \exp(-kt^n) \quad (2.2),$$

where $I(t)$ is current response and C is constant. The Avrami exponent n consists of three indexes as follows,[30]

$$n = a + bc \quad (2.3),$$

where a is nucleation index, b is dimension of growth, and c is growth index. The nucleation index a indicates the time dependence of nucleation rate; $a = 0$ corresponds to nucleation rate of zero, $a = 1$ means constant nucleation rate, and $0 < a < 1$ indicates decreasing nucleation rate with time. The index *b* indicates the dimension of the nuclear growth; *b* = 1, 2, and 3 corresponds to one-, two-, and three- dimensional nuclear growth, respectively. The growth index *c* indicates the rate-limiting step of the phase transformation; *c* = 1/2 and 1 correspond to diffusion and phase-boundary-movement controlled growth, respectively. Figure 2.4 shows chronoamperograms described by KJMA equation with *n* = 1, 1.3, 1.6, and 2. The chronoamperogram with *n* = 1 is monotonic current decrease, whereas those with *n* > 1 are characterized by momentary current increase followed by gradual decline.

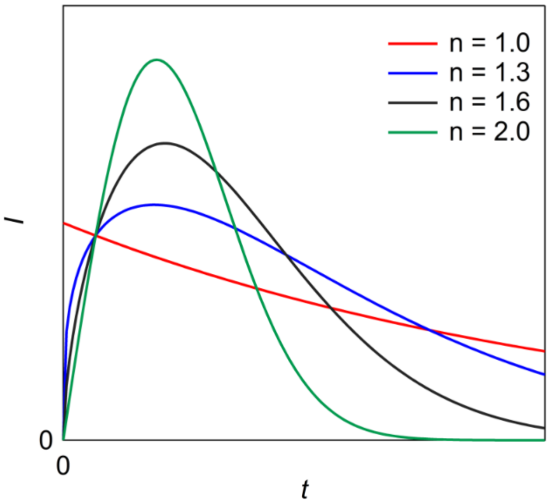

Figure 2.4 Chronoamperograms described by KJMA equation with various Avrami exponents of *n* = 1, 1.3, 1.6, and 2.

2.5 Seeking the best experimental conditions

With the ease and clarity of detecting the response from nucleation and growth, potential-step chronoamperometry is a powerful tool to discuss the kinetics of phase transition. However, special care should be taken to choose an optimum experimental condition in which the current response certainly reflects nucleation and growth. Therefore, in advance to detailed analysis of chronoamperogram, influential factors in current response was investigated to extract the optimum condition for analyzing nucleation and growth. Here, four influential factors are taken into account: amplitude of potential step, mean particle size of Li_xFePO_4, direction of potential step, and thickness of composite electrodes.

2.5.1 Amplitude of potential step

Figure 2.5 shows different current responses of Li_xFePO_4 (mean particle size: 203 nm) under large (150 mV, from 3.50 V to 3.35 V) and small (10 mV, from 3.41 V to 3.40 V) cathodic steps. The thickness of the composite electrode is 1 μm, where the current of 30 μA corresponds to ca. 1 C rate. Under a 10 mV potential step, the chronoamperogram showed momentary current increase followed by gradual decline, which was well-fitted to KJMA equation with Avrami exponent of $n \cong 1.1$ (e.g., $a \cong 0.1$, $b = 1$, and $c = 1$ corresponding to one dimensional phase boundary movement with decreasing nucleation rate). This result indicates that the nucleation and growth of a new phase determine the electrode kinetics and such a small potential step is an appropriate condition for analyzing the kinetics of nucleation and growth. On the other hand, a much larger potential step of 150 mV resulted in monotonic current decrease, which could not be fitted to KJMA equation with Avrami exponent of ca. 1. This suggests that the electrode reaction loses two-phase character and that the nucleation and growth are no longer important processes under such large potential steps. One plausible reason for this behavior is the suppression of phase separation under a large potential step. Malik et al. argued that there should be a non-equilibrium single-phase reaction pathway for the phase transformation of Li_xFePO_4 nanoparticles.[31] Bai et al. reported that, if the applied potential (or current) exceeds a certain threshold (i.e., overpotential that enables the solid-solution pathway), the system behaves as a non-equilibrium quasi-solid solution.[32]

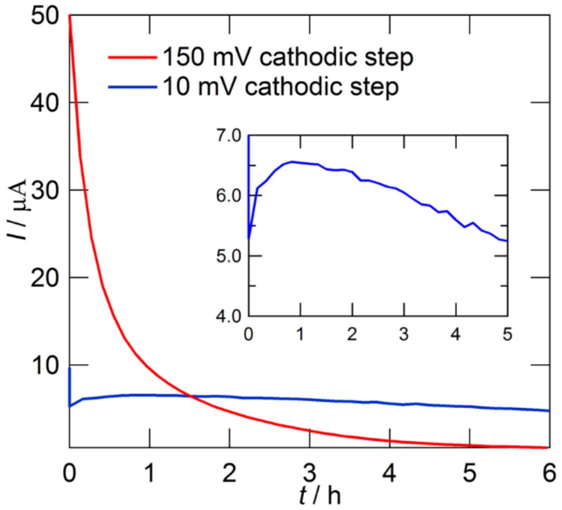

Figure 2.5 Chronoamperograms of $LiFePO_4$ (particle size: 203 nm) composite electrode (thickness: 1 μm) with different amplitude of cathodic potential step: 150 mV (from 3.5 V to 3.35 V) and 10 mV (from 3.42 V to 3.41 V).

Figure 2.6 shows chemical potential profile of Li_xFePO_4 assuming single-phase reaction (blue solid line) and two-phase reaction (blue dashed line). Before the potential step (red solid line), the equilibrium state is solid solution O (Li-poor Li_xFePO_4). When a large potential step (= $E_2 - E_0$) is applied to the system, solid solution B (Li-rich Li_xFePO_4) is the only equilibrium state, where the applied potential (= E_2) corresponds to the chemical potential of solid solution B. In this case, the applied overpotential exceeds potential barrier to single solid-solution region (= E_{sp1}) and there is no need for nucleation and growth at the expense of higher energy. As a result, the reaction proceeds to solid solution B through a non-equilibrium solid-solution pathway. On the other hand, applying the small potential step (= $E_1 - E_0$) results in three equilibrium states, solid solutions A_1, A_2, and A_3, among which the solid solution A_2 is unstable because it is in the spinodal region and the solid solutions A_1 and A_3 are metastable and stable, respectively. In this case, lithiation proceeds with the two-phase reaction of metastable A_1 and stable A_3, and the system finally reaches the single-phase solid solution A_3 driven by the applied potential (= E_1) corresponding to the chemical potential of A_3. Therefore, small overpotential ($< |E_{sp1}|$ or$|E_{sp2}|$) is one of the prerequisites for observing nucleation and growth in Li_xFePO_4. Theoretical calculation by Malik et al. shows that the potential gap between the two spinodal points ($|E_{sp1} - E_{sp2}|$) is ca. 30 mV,[31] which is in good agreement with our result that a two-phase reaction occurs only under such small potential steps as 10 mV. However, the instant nucleation or inhomogeneous reaction will give monotonic current decay also, and the further confirmation combining with diffraction methods are highly required.

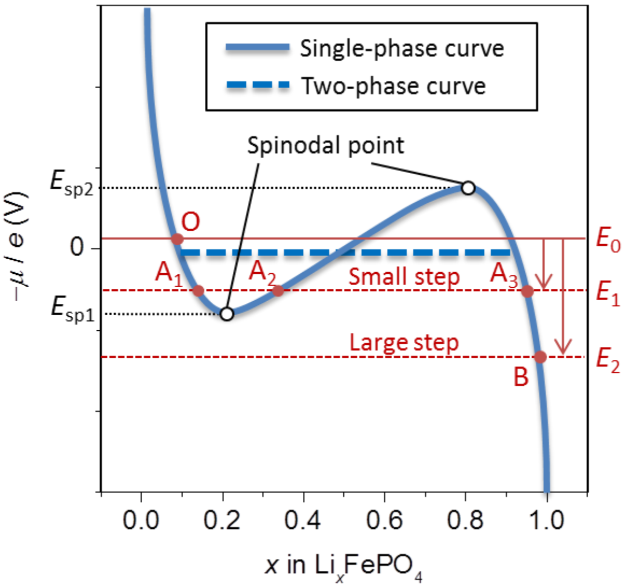

Figure 2.6 Chemical potential profiles of Li_xFePO_4 assuming single-phase reaction (blue solid line) and two-phase reaction (blue dashed line). The symbols O, A_1, A_2, A_3, and B denote the equilibrium states at different potentials (E_0, E_1, and E_2). The white circles indicate spinodal points. In a potential region between two spinodal points (E_{sp1} and E_{sp2}) exists a metastable solid solution (A_1) as well as stable one (A_3).

2.5.2 Particle size

Here the influence of particle sizes on reaction kinetics is surveyed. Figure 2.7 shows current responses of Li_xFePO_4 with three mean particle sizes (203 nm, 84 nm, and 45 nm) under 10 mV potential steps. The momentary current increase gradually disappeared with decreasing particle sizes. The chronoamperogram of 203 nm Li_xFePO_4 showed a “current hump” characteristic of nucleation and growth, whereas those of 84 nm and 45 nm Li_xFePO_4 were monotonic current decrease which could not be fitted to KJMA equation with Avrami exponent of ca. 1. Therefore, the use of large particles (>200 nm) is appropriate for the analysis of nucleation and growth in Li_xFePO_4. In contrast, nucleation and growth might not be the rate limiting step in small Li_xFePO_4 particles (<100 nm) even under the small potential step (10 mV), suggesting that a solid-solution reaction pathway is available at small overpotential for small particles. In Fig. 2.6, the overpotential required for a solid-solution pathway is the potential gap between the spinodal point (E_{sp1} or E_{sp2}) and the two-phase equilibrium ($-\mu / e = 0$ V). Considering the shrinking miscibility gap (i.e., two-phase region)[9,10] and the narrowing spinodal region[33] in a small Li_xFePO_4, the chemical potential curve should vary depending on the particle size, which potentially shifts the potential of spinodal point close to the two-phase equilibrium potential, leading to small overpotential for a solid-solution pathway in a small particle.

2.5.3 Direction of potential step

Next, the influence of current response to different direction of potential step (i.e., lithiation or delithiation) is surveyed. Figures 2.7 (a) and (b) compare cathodic and anodic chronoamperograms of Li_xFePO_4 with 10 mV potential steps (cathodic: from 3.41 V to 3.40 V, anodic: from 3.45 V to 3.46 V). Under both cathodic and anodic steps, the 203 nm Li_xFePO_4 showed momentary current increase characteristic of nucleation and growth governing the electrode kinetics, indicating that cathodic and anodic reactions are symmetric regardless of the composition of a growing Li_xFePO_4 phase (Li-rich or Li-poor) in the two-phase reaction. Whereas, the current hump was not clearly observed for 84 nm and 45 nm Li_xFePO_4; the chronoamperograms of which exhibited monotonic current decrease under both cathodic and anodic steps. This indicates that the solid-solution pathway exists in both lithiation and delithiation reactions at almost the same anodic/cathodic overpotential.

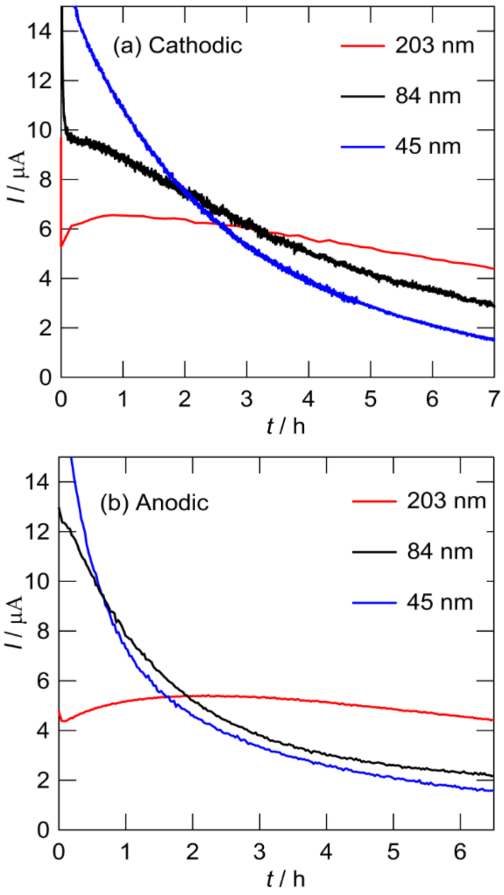

Figure 2.7 Chronoamperograms of Li_xFePO_4 with different particle sizes (203 nm, 84 nm, and 45 nm) under (a) cathodic and (b) anodic 10 mV potential steps. The thickness of composite electrodes is 1 µm.

2.5.4 Thickness of composite electrode

Here the influence of composite-electrode thickness is investigated, because the lithium diffusion in the interspace between particles in a composite electrode may be an influential factor. Figure 2.8 shows chronoamperograms of 203 nm Li_xFePO_4 composite electrodes with different thicknesses of 1 µm and 10 µm under a 10 mV anodic step. Both of the chronoamperograms showed momentary current increase, which were well-fitted to KJMA model with almost the same *n* values, indicating that the nucleation and growth governed two-phase electrode kinetics. In addition, the rate constant *k* of phase-boundary movement was evaluated to be 0.066 and 0.059 for 1 µm- and 10 µm-thick electrodes, respectively. The constant *k* values as well as the good fitting to KJMA model suggest that the lithium diffusion in a composite electrode cannot be a rate-determining step and the nucleation and growth can be observed regardless of the electrode thickness below ca. 10 μm.

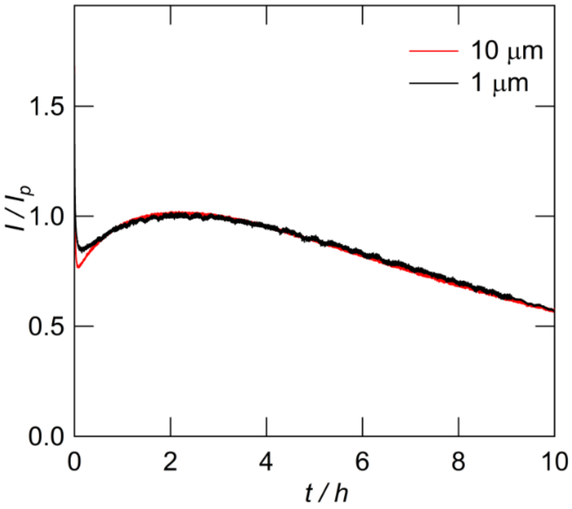

Figure 2.8 Chronoamperograms of 203 nm Li_xFePO_4 composite electrodes with different thicknesses of 1 μm and 10 μm under a 10 mV anodic step. The current (*I*) is normalized by the peak current (I_p).

2.6 Analysis of nucleation and growth

From the above discussions, the optimum condition for analyzing the kinetics of nucleation and growth is using large particles (203 nm) under a small potential step (10 mV). Figure 2.9 shows an example of fitting result for the chronoamperogram of Li_xFePO_4 (203 nm) composite electrode (1 μm thickness) under a 10 mV anodic step. The circles and solid line denote experimental result and fitting curve with KJMA model, respectively. The current response was well-fitted to KJMA model with the Avrami exponent of $n = 1.08$, except for the charge current of electric double layer at the very beginning of the chronoamperogram. The obtained n value of 1.08 is interpreted two ways: (i) two-dimensional diffusion-controlled system ($a = 0.08$, $b = 2$, and $c = 0.5$) or (ii) one-dimensional phase-boundary-movement controlled system ($a = 0.08$, $b = 1$, and $c = 1$). Considering the widely-accepted notion that the reaction of Li_xFePO_4 proceeds with

[100] one-dimensional phase-boundary movement accompanied by cooperative [010] one-dimensional Li diffusion,[15,16] the latter model (ii) should be the plausible interpretation.

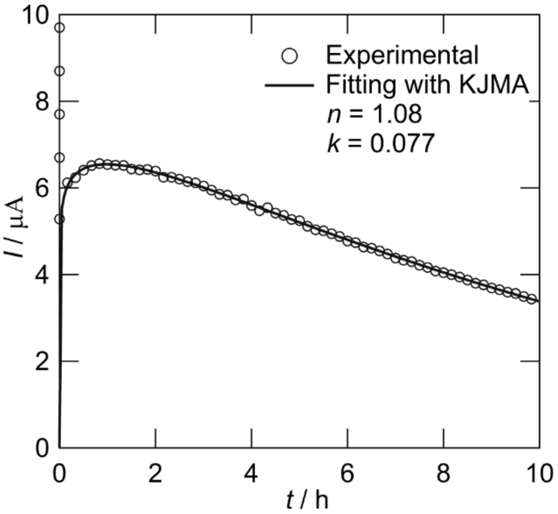

Figure 2.9 Chronoamperogram obtained for the 203 nm $LiFePO_4$ composite electrode (thickness: 1 μm) under a 10 mV anodic step from 3.45 V to 3.46 V. The plots and line denote the experimental and simulating curves, respectively. Obtained Avrami exponent (*n*) and rate constant of phase-boundary movement (*k*) are presented in the figure.

The rate constant k of phase-boundary movement was obtained from the chronoamperograms using the KJMA model. Figure 2.10 shows the temperature dependence of k for 203 nm $LiFePO_4$ under 10 mV potential steps in the temperature range from 25 ºC to 45 ºC. Applied anodic and cathodic steps were from 3.45 V to 3.46 V and from 3.42 V to 3.41 V, respectively. Note that all of the chronoamperograms were well-fitted to KJMA model in the present temperature range and the Avrami exponent n was kept constant within a range between 1.05 and 1.2. The rate constant k showed Arrhenius-type temperature dependence and, from the slope of the ln k vs. $1/T$ plots, the activation energies of phase-boundary movement were evaluated to be 42 kJ mol^{-1} and 40 kJ mol^{-1} during cathodic and anodic reactions, respectively. The almost same activation energy of anodic and cathodic reactions indicates that the phase-boundary movement proceeds in a symmetric way in both directions whether the growing phase is Li-rich or Li-poor. These activation energies were different from that (13 kJ mol^{-1}) obtained by Allen et al. with the same methodology.[23] This is because, in their chronoamperometry, the system behaved as a non-equilibrium solid solution due to the large potential step (500 mV) and the obtained activation energy derived from the single-phase reaction instead of two-phase reaction.

The obtained activation energies of phase-boundary movement in Li_xFePO_4 are substantially lower than other processes (e.g., interfacial charge transfer including a desolvation process and atomic-scale Li diffusion coupled with electron transport). The activation energy of interfacial charge-transfer is reported to be around 50 kJ mol^{-1} in various systems,[34-37] which reflects the energy required for Li^+-desolvation during lithiation.[26, 27] The activation energy of Li diffusion coupled with electron transport is evaluated to be over 50 kJ mol^{-1} by experiment[38] and theoretical calculation.[39] The low activation energies of phase-boundary movement indicate that the electrochemical phase transition in Li_xFePO_4 is relatively fast among several elementary steps of the reaction, which might be one of the factors that characterize Li_xFePO_4 as a high-rate cathode material of lithium-ion batteries.

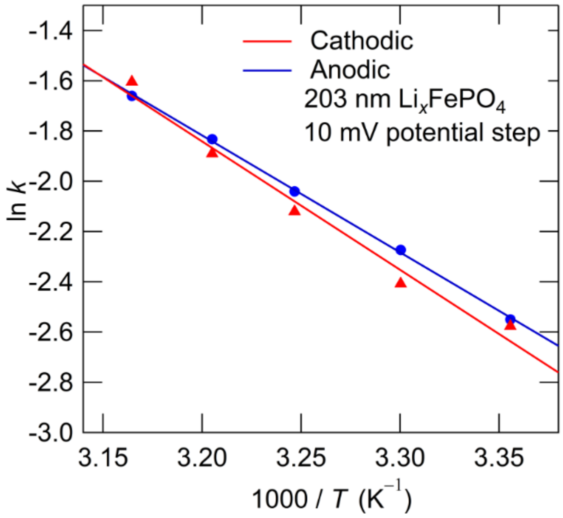

Figure 2.10 Temperature dependence of rate constant of phase-boundary movement (*k*) in 203 nm Li_xFePO_4 under 10 mV cathodic and anodic steps. The *k* values were obtained by fitting the chronoamperograms with KJMA equation.

2.7 Conclusion

Using potential-step chronoamperometry, the present chapter reveals the reaction mechanism of Li_xFePO_4 depends on the amplitude of potential step and particle size. With small particles (<100 nm) or under a large potential step (150 mV), the chronoamperogram exhibits monotonic current decrease, which cannot be fitted to KJMA equation with Avrami exponent of ca. 1, implying the existence of a non-equilibrium solid-solution pathway instead of a widely-accepted two-phase reaction pathway. Only under a small potential step (10 mV) applied to large particles (203 nm), the chronoamperogram is characterized by momentary current increase followed by gradual decline, indicating that the nucleation and growth of a new phase govern the electrode kinetics. Under this condition appropriate for analyzing nucleation and growth, the chronoamperogram is well-fitted to KJMA model with Avrami exponent of ca. 1.1, which is interpreted as one-dimensional phase-boundary movement occurring in Li_xFePO_4. The activation energies of phase-boundary movement in Li_xFePO_4 are evaluated to be 42 kJ mol^{-1} and 40 kJ mol^{-1} during cathodic and anodic reactions, respectively. These values are substantially lower than those of other processes (e.g., interfacial charge transfer and Li diffusion coupled with electron transport in Li_xFePO_4), indicating that the phase transition is relatively fast among several reaction processes in Li_xFePO_4.

References

(1) Armand, M; Tarascon, J. M. *Nature* **2001**, *414*, 359.
(2) Padhi, A.K.; Nanjundaswamy, K.S.; Goodenough, J.B. *J. Electrochem. Soc.* **1997**, *144*, 1188.
(3) Yamada, A.; Chung, S.; Hinokuma, K. *J. Electrochem. Soc.* **2001**, *148*, A224.
(4) Kang, B.; Ceder, G. *Nature* **2009**, *458*, 190.
(5) Delacourt, C.; Poizot, P.; Levasseur, S.; Masquelier, C. *Electrochem. Solid State Lett.* **2006**, *9*, A352.
(6) Chung, S. Y.; Bloking, J. T.; Chiang, Y. M. *Nature Mater.* **2002**, *1*, 123.
(7) Delacourt, C.; Poizot, P.; Tarascon, J. M.; Masquelier, C. *Nature Mater.* **2005**, *4,* 254.
(8) Yamada, A.; Koizumi, H.; Nishimura, S.; Sonoyama, N.; Kanno, R.; Yonemura, M.; Nakamura, T.; Kobayashi, Y. *Nature Mater.* **2006**, *5*, 357.

(9) Meethong, N.; Huang, H. Y. S.; Carter, W. C.; Chiang, Y. M. *Electrochem. Solid-State Lett.* **2007**, *10*, A134.

(10) Kobayashi, G.; Nishimura, S.; Park, M. S.; Kanno, R.; Yashima, M.; Ida, T.; Yamada, A. *Adv. Funct. Mater*. **2009**, *19*, 395.

(11) Morgan, D.; der Ven, A. V.; Ceder, G. *Electrochem. Solid-State Lett.* **2004**, *7*, A30.

(12) Islam, M.; Driscoll, D.; Fisher, C.; Slater, P. *Chem. Mater.* **2005**, *17*, 5085.

(13) Nishimura, S.; Kobayashi, G.; Ohoyama, K.; Kanno, R.; Yashima, M.; Yamada, A. *Nature Mater*. **2008**, *7*, 707.

(14) Delmas, C.; Maccario, M.; Croguennec, L.; Le Cras, F.; Weill, F. *Nature Mater.* **2008**, *7*, 665.

(15) Chen, G.; Song, X.; Richardson, T. J. *Electrochem. Solid-State Lett.* **2006**, *9*, A295.

(16) Laffont, L.; Delacourt, C.; Gibot, P.; Yue Wu, M.; Kooyman, P.; Masquelier, C.; Tarascon, J. M. *Chem. Mater.* **2006**, *18*, 5520.

(17) Bard, A. J.; Faulkner, L. R. "Electrochemical Methods, Fundamentals and Applications, 2nd Ed." Wiley, New York **2001**.

(18) Levi, M. D.; Aurbach, D. *J. Solid State Electrochem.* **2007**, *11*, 1031.

(19) Levi, M. D.; Levi, E. A.; Aurbach, D. *J. Electroanal. Chem.* **1997**, *421*, 89.

(20) Pyun, S. I., Ryu, Y. G. *J. Power Sources* **1998**, *70*, 34.

(21) Funabiki, A; Inaba, M.; Abe, T.; Ogumi, Z. *Electrochim. Acta*, **1999**, *45*, 865.

(22) Funabiki, A.; Inaba, M.; Abe, T.; Ogumi, Z. *J. Electro-chem. Soc.* **1999**, *146*, 2443.

(23) Allen, J. L.; Jow, T. R.; Wolfenstine, *J. Chem. Mater.* **2007,** *19*, 2108.

(24) Allen, J. L.; Jow, T. R.; Wolfenstine, *J. Solid State Elecro-chem.* **2008**, *12*, 1031.

(25) Avrami, M. *J. Chem. Phys.* **1939**, *7*, 1103.

(26) Avrami, M. *J. Chem. Phys.* **1940**, *8*, 212.

(27) Avrami, M. *J. Chem. Phys.* **1941**, *9*, 177.

(28) Meethong, N.; Kao, Y. H.; Carter, W. C.; Chiang, Y. M. *Chem. Mater.* **2010**, *22*, 1088.

(29) Okubo, M.; Mizuno, Y.; Yamada, H.; Kim, J.; Hosono, E.; Zhou, H. S., *ACS Nano* **2010**, *4*, 741.

(30) Ranganathan, S.; von Heimendahl, M. *J. Mater. Sci.* **1981**, *16*, 2401.

(31) Malik, R.; Zhou, F.; Ceder, G. *Nature Mater.* **2011**, *10*, 587.

(32) Bai, P.; Cogswell, D. A.; Bazant, M. Z. *Nano Lett.* **2011**, *11*, 4890.

(33) Burch, D.; Bazant, M. Z. *Nano Lett.* **2009**, *9*, 3795.

(34) Yamada, I.; Iriyama, Y.; Abe, T.; Ogumi, Z. *J. Power Sources* **2007**, *172*, 933.

(35) Yamada, I.; Abe, T.; Iriyama, Y.; Ogumi, Z. *Electrochem. Commun.* **2003**, *5*, 502.

(36) Yamada, Y.; Iriyama, Y.; Abe, T.; Ogumi, Z. *Langmuir* **2009**, *25*, 12766.

(37) Yamada, Y.; Sagane, F.; Iriyama, Y. Abe, T.; Ogumi, Z. *J. Phys. Chem. C* **2009**, *113*, 14528.

(38) Ellis, B.; Perry, L. K.; Ryan, D. H.; Nazar, L. F. *J. Am. Chem. Soc.* **2006**, *128*, 11416.

(39) Maxisch, T.; Zhou, F.; Ceder, G. *Phys. Rev. B* **2006**, *73*, 104301.

3. Electrochemical Properties of Heterosite $FePO_4$ in Aqueous Mg^{2+} Electrolytes

3.1 Introduction

Development of advanced energy storage is one of the most urgent challenges to realize sustainable society. Li-ion batteries are the state-of-the-art power sources for most portable electronic devices; however, large scale application for power grid requires inexpensive and safe batteries, which has spurred research activities for new battery systems.

One possible way to achieve inexpensive and safe batteries is to utilize magnesium systems.[1] In contrast to less abundant and maldistributed Li in the earth, Mg is earth abundant and evendistributed, allowing to reduce the cost of the batteries. Another possible positive outcome is efficient charge storage by divalent cation (Mg^{2+}), which may lead to large energy density. Thus, exploring reversible Mg^{2+} (de)intercalation compounds are very important toward suitable electrode materials of rechargeable Mg batteries.

An intrinsic obstacle for reversible Mg^{2+} (de)intercalation is large deformation of the local structure by accommodation of two-electron associated with Mg^{2+}.[2–4] For example, the Chevrel phase Mo_6T_8 (T = S and Se) shows fast and reversible Mg^{2+} intercalation, because multiple electrons can be accommodated with delocalized orbital of a Mo_6T_8 cluster to relieve the local structure deformation.[2] However, most previous works on Mg^{2+} intercalation have focused on nanosized compounds such as V_6O_{13},[5] MoS_2,[6] $MgMSiO_4$ (M = Mn, Fe and Co),[7–9] RuO_2,[10] Co_3O_4,[11] TiS_2,[12] and MnO_2,[13,14] where the detailed reaction mechanism has not been clarified.

In this work, the electrochemical reaction of heterosite $FePO_4$ in aqueous Mg^{2+} electrolyte is investigated. Heterosite $FePO_4$ is a metastable phase obtained by delithiation from triphilite $LiFePO_4$ and an important host electrode material because of the intercalation capability with various monovalent cations as guest species.[15,16] Herein, the electrochemical reaction mechanism of $FePO_4$ with Mg^{2+} in aqueous electrolyte is clarified by *ex-situ* Mössbauer spectroscopy, X-ray diffraction experiments, and ab-initio calculation.

3.2 Experimental methods

$LiFePO_4$/C composites including 10 wt% additive carbons (8 wt% carbon black, and 2 wt% vapor-grown carbon nano fiber) were synthesized according to the procedure reported previously.[17] $FePO_4$/C composites were prepared by chemical oxidation of $LiFePO_4$/C composites with nitronium tetrafluoroborate (NO_2BF_4; Alfa Aesar, 96%) in acetonitrile.[17] The products were filtered several times by acetonitrile to remove impurities before they were dried under vacuum at 60 °C.

The X-ray diffraction measurement was conducted at room temperature by using Bruker AXS D8 ADVANCE powder diffractometer equipped with Co Kα radiation source in the 2θ range from 15° to 80°. Structural refinement was performed by using a Topas ver. 3.0 program.

The paste for the working electrode was prepared by mixing 85 wt% $FePO_4$/C composite, 5 wt% carbon black (Ketjen Black, Lion Corp.), and 10 wt% polytetrafluoro-ethylene (PTFE), which was pressed onto Ti meshes. The total carbon content in the electrode is 13.5 wt%. All the electrochemical measurements were performed with three-electrode beaker-type cells at 298 K. A platinum mesh and Ag/AgCl electrode were used for the counter and reference electrodes, while 0.5 mol dm^{-3} $MgSO_4$ aqueous solution (pH 7.82) was used as the electrolyte. Note that oxygen dissolved in the electrolyte was degassed by Ar gas bubbling for 2 h. For cyclic voltammetry (CV), linear potential sweep was repeated with a scan rate of 0.03 mVs^{-1} in the voltage range between –0.5 and 0.5 V (vs. Ag/AgCl). For charge/discharge measurements, a constant current at a rate of C/20 was applied in the voltage range between –0.6 and 0.6 V (vs. Ag/AgCl).

^{57}Fe Mössbauer spectra were collected with a transmission optics spectrometer (Toplogic System, Inc.). A ^{57}Co dispersed Rh matrix was used as the radiation source and the proportional counter. α–Fe was used as a standard to calibrate velocity and isomer shift at room temperature with MossWinn Ver. 3.0 software. The chemical composition of the electrode material during the discharge-charge processes was determined by the inductively coupled plasma atomic emission spectrometry (ICP-AES, iCAP DUO-6300). The electrodes after soaked to the electrolyte, after first discharge, and after first charge were dissolved in 0.1 mol dm^{-3} HCl solution for the ICP measurements, respectively. The amount of Fe and Mg was calibrated by $Fe(NO_3)_3$ and $Mg(NO_3)_2$ solution (0−4 ppm).

All the DFT calculations were performed by Chung et al. using the Vienna Ab-Initio Simulation Package (VASP).[18] The PBE exchange-correlation functional[18] was employed and the wavefunctions are treated with the PAW method.[19] The energy cutoff for the planewave basis was 520 eV and a 2×2×2 k-point mesh was used. The calculations were spin-polarized with the ordering of spins on the Fe ion assumed to be ferromagnetic. A supercell with a size of 1×2×2 that of the unit cell of $FePO_4$ was used. The calculations were done by firstly optimizing the unit cell after inserting one Li/Mg ion into the supercell, then the unit cell dimensions was kept at the optimized values and the Li/Mg diffusion path was computed with the climbing-image nudged elastic band method.[20] The criterion for force convergence was 0.010 eV/Å.

3.3 Sample characterization for heterosite $FePO_4$

Figure 3.1 shows the X-ray diffraction (XRD) pattern and the Rietveld refinement result of the $FePO_4$/C composite, which was synthesized by the chemical oxidation of the $LiFePO_4$/C composite. The refined parameters are summarized in Table 3.1. The fitting is satisfactory (R_{wp} = 1.28 %, R_{p} = 0.98 %, R_{Bragg} = 0.559, and GOF = 1.45), and all the Bragg reflections are indexed in orthorhombic lattice parameters of a = 9.8246 (4) Å, b = 5.7981 (2) Å, c = 4.7846 (2) Å, and V = 272.55 (2) Å with *Pnma* symmetry. These values are consistent with the previous result (a = 9.819 Å, b = 5.792 Å, c = 4.782 Å, and V = 272.0 Å),[21] suggesting successful fabrication of a single $FePO_4$ phase without impurity.

The mean size of the crystallites is estimated as 48.0(4) nm by the Rietveld refinement. SEM images of $FePO_4$ particles (inset in Fig. 3.1) show that the average particle size is 46±11 nm, which is consistent with the Rietveld refinement result.

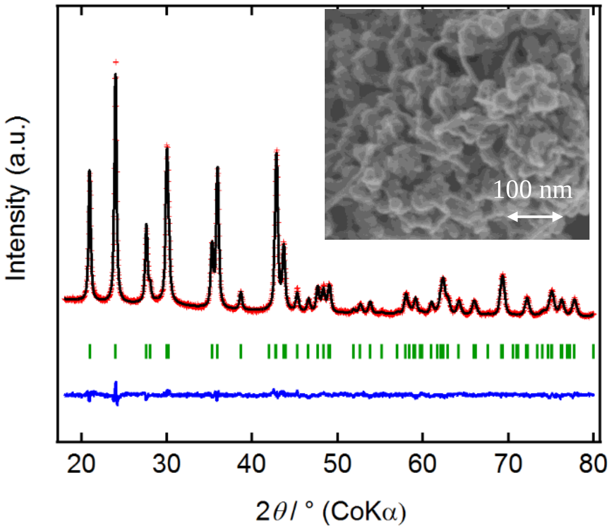

Figure 3.1 X-ray diffraction pattern and the Rietveld refinement result for chemically oxidized $FePO_4$. The inset shows a typical SEM image of $FePO_4$ particles.

Table 3.1 Refined structural parameters of chemically oxidized $FePO_4$.

Site	*x*	*y*	*z*	*g*	B_{eq}
Fe	0.2750 (4)	0.25	0.9516 (3)	1	0.6
P	0.0935 (2)	0.25	0.3930 (6)	1	0.6
O1	0.1198 (4)	0.25	0.7141 (9)	1	1
O2	0.4373 (6)	0.25	0.1597 (7)	1	1
O3	0.1683 (4)	0.0399 (4)	0.2450 (5)	1	1

a = 9.8246 (4) Å, b = 5.7981 (2) Å, and c = 4.7846 (2) Å

R_{wp} = 1.28 %, R_{exp} = 0.88 %, R_p = 0.98 %, and GOF = 1.45

3.4 Electrochemical properties in aqueous Mg^{2+} electrolytes

Figure 3.2 shows the cyclic voltammograms of the $FePO_4$ electrode in 0.5 mol dm^{-3} $MgSO_4$ aqueous solution at 298 K with a scan rate of 0.03 mVs^{-1}. While a sharp cathodic wave is observed at −0.42 V (vs. Ag/AgCl), a broad anodic wave is observed at −0.10 V. The separation between the cathodic and anodic peaks is very large (~ 320 mV) even with the very slow scan rate of 0.03 mVs^{-1}, suggesting the slow kinetics and/or irreversibility of the electrode reaction. Furthermore, the significant difference between the cathodic and anodic wave shapes strongly implies irreversible electrode reaction. Since the peak current of the cathodic wave decreases with repeating the CV cycle, the $FePO_4$ electrode has poor cycle stability against the electrochemical reaction with aqueous Mg^{2+} electrolyte.

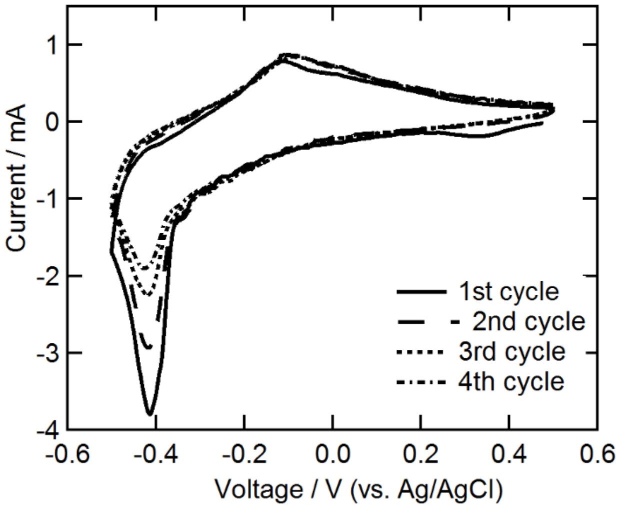

Figure 3.2 Cyclic voltammogram of $FePO_4$ electrode in 1 mol dm^{-3} $MgSO_4$ aqueous solution at a scan rate of 0.03 mV s^{-1}.

Figure 3.3 shows the discharge/charge curves at C/20 rate during the initial three cycles. The potential profile on the first discharge exhibits a sloping plateau centered at ca. −0.4 V (vs. Ag/AgCl), delivering the specific capacity of 90.5 mAh g^{-1}. Under the Assumption that the electric current is derived entirely from the Mg^{2+} intercalation ($FePO_4 + xMg^{2+} + 2xe^- \rightarrow Mg_x(FePO_4)$; theoretical capacity: 177 mAh g^{-1} for $0 < x < 0.5$), the first discharge capacity corresponds to 0.25 Mg^{2+} intercalation.

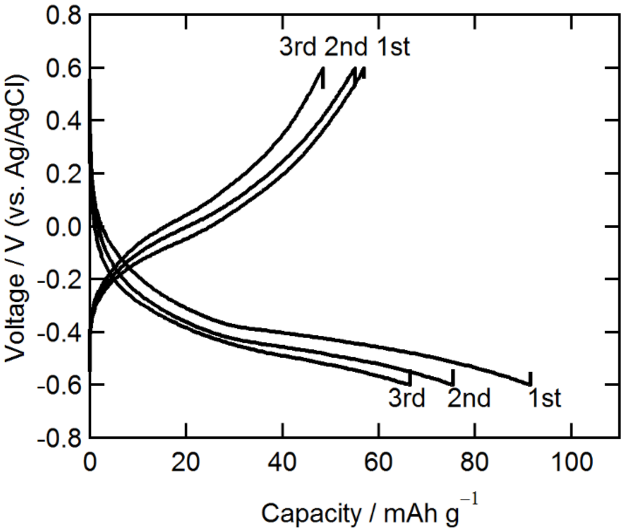

Figure 3.3 Discharge/charge curves of $FePO_4$ in 1 mol dm^{-3} $MgSO_4$ aqueous solution at a rate of C/20 (conducting at 298 K).

The first charge curve exhibits a sloping potential profile over a wide voltage range from −0.4 to 0.5 V, which agrees with the broad anodic wave in the CV curve. The first charge capacity is 56.6 mAh g^{-1} with coulombic efficiency of 63 %. As suggested by the CV cycles, the discharge/charge capacity decreases with repeating the cycle. Thus, the $FePO_4$ electrode has suffered from poor cycle stability in aqueous Mg^{2+} electrolyte.

3.5 Structural variation during electrochemical processes

To reveal the reaction mechanism, *ex-situ* Mössbauer spectroscopy was carried out for the pristine, discharged and charged samples (Fig. 3.4). The results for the curve fitting are summarized in Table 3.2. The pristine $FePO_4$ compound shows a doublet peak, which is fitted mainly by a doublet with the isomer shift (IS) of 0.427 mm s^{-1} and the quadrupole splitting (QS) of 1.531 mm s^{-1}. These values are consistent with those reported for high spin Fe^{3+} in $FePO_4$ (IS = 0.42 mm s^{-1} and QS = 1.5 mm s^{-1}) .[22] However, note that the best fit needs 8.1 % of another doublet (IS = 0.42 mm s^{-1} and QS = 0.661 mm s^{-1}), suggesting existence of defects or surface sites.

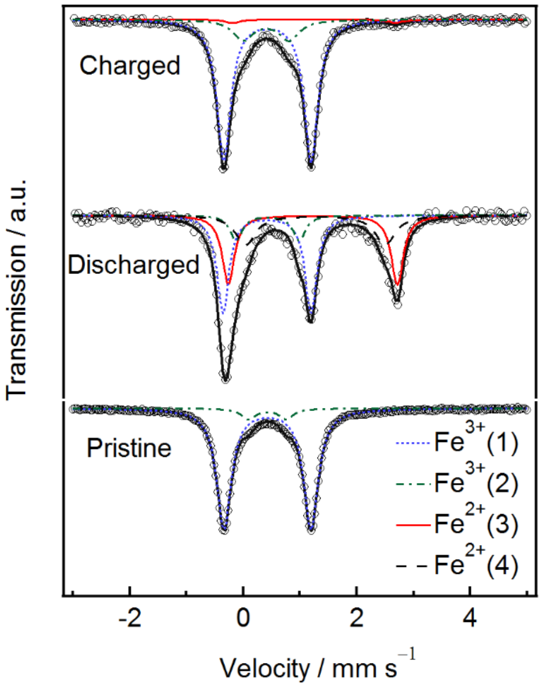

Figure 3.4 ***Ex-situ*** **Mössbauer spectra of the pristine, discharged, and charged $FePO_4$ electrodes.**

The Mössbauer spectrum for the discharged compound is best fitted by four doublets. The fraction of the Fe^{3+} doublet observed for the pristine compound decreases from 92% to 40%, whereas two new doublets with IS of 1.22–1.27 mm s^{-1} and QS of 2.5–3.0 mm s^{-1} emerge. These IS and QS values are close to those reported for high spin Fe^{2+} in $LiFePO_4$ (IS = 1.2 and QS = 3.0 mm s^{-1}) .[22] Thus, 50% of Fe^{3+} in the pristine $FePO_4$ is reduced to Fe^{2+} by discharging, which is in good agreement with the initial discharge capacity of 90.5 mAh g^{-1}. It should be emphasized that QS of one Fe^{2+} doublet (Fe^{2+}(4); 2.46 mm s^{-1}) is smaller to that of $LiFePO_4$ (3.0 mm s^{-1}). This result suggests that the local coordination change of Fe by the electrochemical reaction in aqueous Mg^{2+} electrolyte differs from that by Li^{+} intercalation. After charge, the Fe^{2+} doublets almost disappear while the fraction of the Fe^{3+} doublet is recovered to 85 %. Thus, reversible redox of Fe^{3+} / Fe^{2+} occurs on discharge–charge with Mg^{2+} aqueous electrolyte.

Table 3.2 Refined Parameters for Mössbauer Spectrum of the pristine, discharged and charged $FePO_4$. Normalized χ^2 for each fitting were 2.07, 1.0007, and 1.28 for pristine, first discharged, and first charged $FePO_4$ electrodes, respectively.

		Isomer shift (IS) / mm s^{-1}	Quadrupole splitting (QS) / mm s^{-1}	Fraction / %	Line width / mm s^{-1}
Pristine	Fe^{3+} (1)	0.4268 (2)	1.5309 (8)	91.9 (2)	0.313 (9)
	Fe^{3+} (2)	0.424 (4)	0.661 (9)	8.1 (1)	0.256 (8)
Discharged	Fe^{3+} (1)	0.417 (3)	1.549 (8)	40.1 (1)	0.256 (8)
	Fe^{3+} (2)	0.428 (16)	1.11 (5)	10.5 (1)	0.256 (8)
	Fe^{2+} (3)	1.224 (5)	2.97 (2)	28.8 (1)	0.256 (8)
	Fe^{2+} (4)	1.270 (11)	2.46 (5)	20.6 (1)	0.43 (3)
Charged	Fe^{3+} (1)	0.4259 (6)	1.530 (1)	85.4 (2)	0.3051 (2)
	Fe^{3+} (2)	0.406 (6)	0.72 (1)	11.8 (2)	0.3051 (2)
	Fe^{2+} (3)	1.255 (2)	2.84 (4)	2.8 (2)	0.3051 (2)

To further clarify the reaction mechanism, the *ex-situ* XRD measurements for the pristine, discharged, and charged compounds are conducted. The XRD patterns in Fig. 3.5 show neither peak shift of the original phase nor emergence of new peaks for a Mg^{2+} intercalated phase on discharge/charge. Whole profile fitting analyses on the diffraction patterns suggest only ca. 1.0 % of reversible volume expansion/contraction. Furthermore, significant peak broadening in all indices suggests strong lattice distortion and inhomogeneity at the discharged state. Since the observed volume change is very close to that in a solid solution region of Li_xFePO_4 ($0 < x < 0.05$)[17], the solid solution state, i.e., Mg_xFePO_4 may exist at the early stage of discharge. However, the 1.0% volume change is much smaller than that (ca. 7%) predicted for $FePO_4/Mg_{0.5}FePO_4$ by density functional theory (DFT) calculation[23]. Thus, reversible redox of Fe^{3+} / Fe^{2+} in the $FePO_4$ electrode cannot be explained by topochemical Mg^{2+} (de)intercalation.

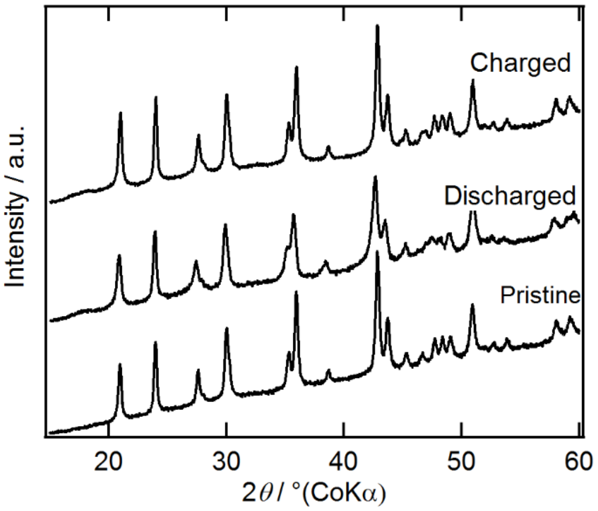

Figure 3.5 ***Ex-situ*** **X-ray diffraction patterns of the pristine, discharged, and charged $FePO_4$ electrodes.**

Then, the DFT calculation were performed by Chung et al, which also supports that topochemical Mg^{2+} intercalation is improbable in $FePO_4$.[26] Fig. 3.6 (a) shows the energies of Li^+ and Mg^{2+} along the minimum energy paths in $FePO_4$ calculated by the nudged elastic band method. The energy barriers for Li^+ diffusion are calculated to be about 0.20 eV. This agrees well with previously reported values.[24,25] The minimum energy profile has a characteristic dip in the mid of the path where the Li^+ occupies a tetrahedral site (Fig. 3.6 (b)). For Mg^{2+}, the activation energy is found to be more than three times that of Li^+, about 0.67 eV. The dip at the intermediate tetrahedral site is also found for Mg^{2+} but it is much more pronounced. These show that the smaller and higher-valent Mg^{2+} interacts much stronger with the framework when compare to the Li^+. The large activation energy for Mg^{2+} suggests that the topochemical intercalation into $FePO_4$ is difficult.

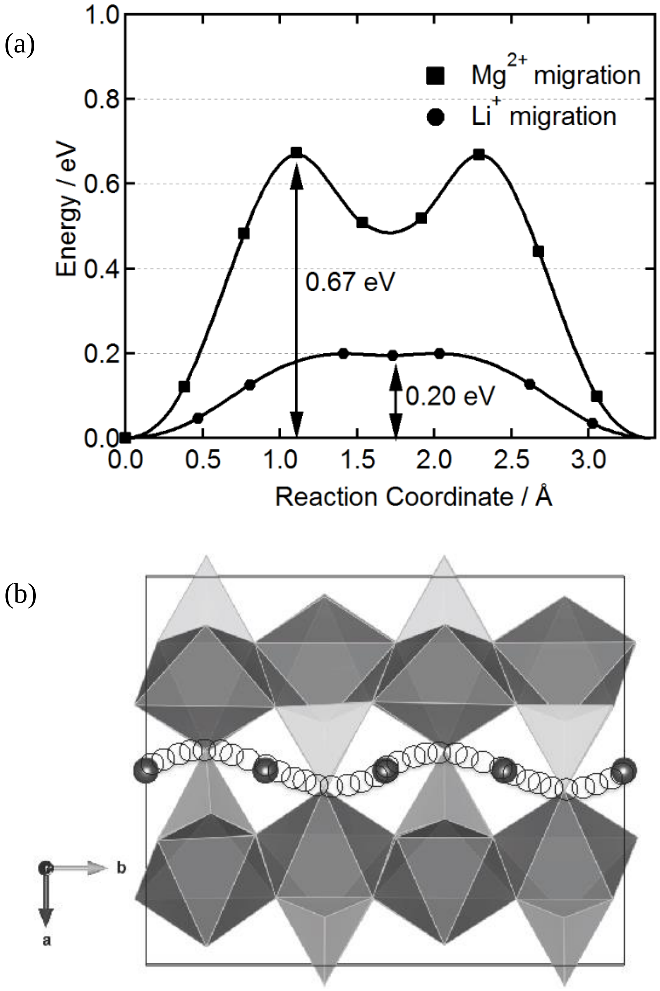

Figure 3.6 (a) Minimum energy path for Li^+ and Mg^{2+}-ions migration in $FePO_4$. (b) Migration path along *b* direction in $FePO_4$.[26]

The ICP measurement determines that the electrode after the first discharge contains 0.38 Mg per the formula unit of $FePO_4$, while those before the first discharge and after the first discharge/charge cycle contain *ca.* 0.02 Mg. Thus, the $FePO_4$ electrode should react with Mg^{2+}. It is most likely that, on discharge, the crystalline $FePO_4$ phase is partially transformed to an amorphous phase by non-topochemical Mg^{2+} intercalation. On charge, the Mg^{2+} intercalated amorphous phase may be oxidized to another amorphous phase by Mg^{2+} deintercalation. The irreversible partial phase transformation from the crystalline state to the amorphous state may explain both the asymmetric wave shapes in the CV curves and little change in the *ex-situ* XRD patterns.

3.6 Conclusion

The $FePO_4$ electrode shows partially reversible capacity with aqueous Mg^{2+} electrolyte on charge/discharge experiments. Reversible redox of Fe^{3+} / Fe^{2+} is evidenced by *ex-situ* Mössbauer spectroscopy, whereas little structural change occurs in the *ex-situ* XRD patterns. DFT calculation revealed activation energy for Mg^{2+} diffusion is over three times larger than that of Li^+, suggesting the topochemical intercalation into $FePO_4$ is difficult. All of these results might suggest that partial fraction of the $FePO_4$ phase becomes an amorphous phase by non-topochemical Mg^{2+} intercalation. This work suggests that an apparent capacity obtained in the charge/discharge experiments does not necessarily correspond to topochemical intercalation reaction, and therefore it is indispensable to analyze the structural and chemical states of the material as a function of incremental Mg^{2+} intercalation.

References

(1) Yoo H. D.; Shterenberg I.; Gofer Y.; Gershinsky G.; Pour N.; Aurbach D., *Energy Environ. Sci.* **2013**, 6, 2265.

(2) Aurbach D.; Lu Z.; Schechter A.; Gofer Y.; Gizbar C.; Turgeman R.; Cohen Y.; Moshkovich M.; Levi E., *Nature* **2000**, 407, 724.

(3) Levi E.; Gofer Y.; Aurbach D.; *Chem. Mater.*, **2010**, 22, 860.

(4) Levi E.; Levi M. D.; Chasid O.; Aurbach D., *J. Electroceram.* **2009**, 22, 13.

(5) Bruce P. G.; Krok F.; Nowinski J.; Gibson V. C.; Tavakkoli K., *J. Mater. Chem.* **1991**, 1, 705.

(6) Liang Y.; Feng R.; Yang S.; Ma H.; Liang J.; Chen J., *Adv. Mater.* **2011**, 23, 640.

(7) Nuli Y.; Yang J.; Li Y.; Wang J.; *Chem. Commun*. **2010**, 46, 3794.

(8) Li Y.; Nuli Y.; Yang J.; Yilinuer T.; Wang J., *Chin. Sci. Bull*. **2011**, 56, 386.

(9) Nuli Y.; Zheng Y.; Wang Y.; Yang J.; Wang J., *J. Mater. Chem*. **2011**, 21, 12437.

(10) Sutto T. E.; Duncan T. T.; *Electrochim. Acta* **2012**, 79, 170.

(11) Sutto T. E.; Duncan T. T., *Electrochim. Acta* **2012**, 80, 413.

(12) Tao Z. L.; Xu L. N.; Gou X. L.; Chen J.; Yuan H. T., *Chem. Commun.* **2004**, 18, 2080.

(13) Zhang R.; Yu X.; Nam K. W.; Ling C.; Arthur T. S.; Song W.; Knapp A. M.; Ehrlich S. N.; Yang X. Q.; Matsui M., *Chem. Commun.*, **2012**, 23,110.

(14) Rasul S.; Suzuki S.; Yamaguchi S.; Miyayama M., *Electrochim. Acta,* **2004**, 82, 243.

(15) Padhi A. K.; Nanjundaswamy K. S.; Goodenough J. B., *J. Electrochem. Soc.* **1997**, 144, 1188.

(16) Moreau P.; Guyomard D.; Gaubicher J.; Boucher F., *Chem. Mater.*, **2010**, 22, 4126.

(17) Kobayashi G.; Nishimura S.; Park M. S.; Kanno R.; Yashima M.; Ida T.; Yamada A., *Adv. Funct. Mater*. **2009**, 19, 395.

(18) Perdew J. P.; Burke K.; Ernzerhof M., *Phys. Rev. Lett.* **1996**, 77, 3865.

(19) Blöchl P. E., *Phys. Rev. B*. **1994**, 50, 17953.

(20) Henkelman G.; Uberuaga B. P.; Jónsson H., *J. Chem. Phys.* **2000**, 113, 9901.

(21) Yamada A.; Koizumi H.; Sonoyama N.; Kanno R., *Electrochem. Solid State Lett*. **2005**, 8, A409.

(22) Ellis B.; Perry L. K.; Ryan D. H.; Nazar L. F., *J. Am. Chem. Soc.*, **2006**, 128, 11416.

(23) Ling C.; Banerjee D.; Song W.; Zhang M.; Matsui M., *J. Mater. Chem*. **2012**, 22, 13517.

(24) Morgan D.; der Ven A. V.; Ceder G., *Electrochem. Solid-State Lett*. 2**004**, 72, A30.

(25) Dathar G. K. P.; Sheppard D.; Stevenson K. J.; Henkelman G., *Chem. Mater.* **2011**, 23, 4032 (2011).

(26) Oyama, G.; Nishimura, S.; Chung, S.-C.; Okubo, M.; Yamada, A. *Electrochemistry* **2014**, *82*, 855–858.

Part II

Alluaudite sodium iron sulfate as a sodium-ion battery cathode

4. A 3.8 V Earth-Abundant Sodium Battery Electrode

4.1 Introduction

Li-ion battery was intensely explored in 1980s leading to its commercialization in 1990s. Ever since, the synergistic effort in basic science and industrial optimization has led to the doubling of energy-density. Currently, Li-ion batteries are ubiquitous in suites of small-scale consumer electronics, power-tools as well as large-scale power sources driving the (plug-in) hybrid electric transportation and power-grid systems. The ever-growing global population and the meteoric rise in demand of easy access to modern technologies (gadgets / automobiles) have created multi-billion dollar battery industry. The current generation Li-ion batteries employ oxides (such as $LiCoO_2$, $LiMn_2O_4$) and olivine $LiFePO_4$ as cathodes.[1–3] Suddenly this manifold consumption of Li has led to its scarcity and price rise, with many raising a concern if lithium is the new gold that may trigger geo-political tension in future.[4]

The vast range of battery applications can be divided into two broad categories: volume/weight restricted applications like electronics/ automobiles and volume/weight less dependent uses like remote area large power-grid systems for efficient use of electricity transmitted from thermal power plants and solar/wind mills. While the Li-batteries are indispensable for former category, the latter category has been economically catered in part by Na-S batteries operating at high temperature over 300°C. Resource optimization and tailor-made battery design for different applications, including dense smart grid with self-management housing system, is a global call, where Na-ion batteries operating at ambient temperatures can play vital role.

Contrary to lithium, sodium has abundant natural resources with even geographic distribution. Being the fifth-most abundant element in earth's crust, the Na charge carrier is also the second lightest alkali element in periodic table. In this context, mammoth effort has been geared to build efficient sodium-ion batteries with optimization of energy density, rate kinetics, low cost as well as safe and sustainable production and operation. In this pursuit, numerous Fe-based cathode compounds capable of efficient Na (de)insertion have been reported.[5–11]

Looking back the history, soon after the conceptualization of intercalation reaction into TiS_2 host in 1976,[12] research into Li-based and Na-based insertion compounds kick-started in early 1980s[1,5]. However, the commercial prospects of Li-ion batteries in portable electronics owing to its light-weight steered massive effort Li-systems resulting in a two decade long hibernation period for Na-counterparts. Over the past few years, the renewed interest on sodium chemistry has seen a number of researches on various layered oxide phases, mostly based on expensive transition metals, such as cobalt and nickel. The large-scale sodium batteries will be commercially viable with earth-abundant transition metal such as Fe.

Till date O3-type $NaFeO_2$[13,14] and P2-type $Na_x[Fe_{1/2}Mn_{1/2}]O_2$[7] are reported, but both of them registering low operating potential even utilizing Fe^{4+}/Fe^{3+} redox couple and reversibility is relatively limited. Using the inductive effect in polyanion framework systems, Fe^{3+}/Fe^{2+} redox potential can be enhanced with full utilization of one-electron reaction.[14] In this pursuit, many ~3 V Fe-based phosphate PO_4^{3-} insertion compounds have been reported. They are Na_2FePO_4F[8] (the average potential is ca. 3.06 V versus Na^+/Na), $NaFePO_4$ (ca. 2.7 V)[9], $Na_2FeP_2O_7$(ca. 3 V)[10] and $Na_4Fe_3(PO_4)_2(P_2O_7)$ (ca. 3.2 V)[11]. Newer Fe-based compounds with higher electrode potential can be realized by replacing phosphate PO_4^{3-} with sulphate SO_4^{2-} units taking advantage of their higher electronegativity.[14] This avenue is not yet realized with the only known SO_4^{2-} based compounds $NaFeSO_4F$ and $NaFeSO_4F\cdot 2H_2O$ being electrochemically inactive.[15,16]

Herein, an entirely new class of cathode, sodium iron sulfate is reported, combining the unusually high Fe-redox potential around 3.8 V versus Na with excellent rate kinetics as well as good economy. It benchmarks the highest ever Fe^{3+}/Fe^{2+} redox potential by far observed among all known oxides and oxyanionic insertion materials for sodium-ion batteries. Unlike the oxides and various polyanions (BO_3^{3-}, PO_4^{3-}, SiO_4^{4-}) compounds, theSO_4^{2-} containing systems are acutely prone to thermal decomposition above ~ 400 °C (leading to SO_2 gas evolution).

Additionally, inherent dissolution of SO_4^{2-} in water makes it unstable in aqueous media. It rules out conventional high-temperature solid-state and aqueous solution-based synthetic routes. Thus, low temperature ($T_r \leq 350$ °C) solid-state methods are applied to obtain target compound.

4.2 Experimental methods

The target material was synthesized by reacting 1.54 g Na_2SO_4 (Wako, 99%) and 2.73 g $FeSO_4$. The anhydrous $FeSO_4$ precursor was prepared in-house by annealing commercial $FeSO_4{\cdot}7H_2O$ (Wako, 99%) under primary vacuum at 200 °C for 12 h35. The sodium iron sulfate cathode compound was obtained via classical solid-state synthesis by ballmilling the precursors for 4 h followed by annealing the mixture at 350 °C for 24 h under steady Ar flow. As sulfate based compounds are prone to dissolvation (in water) and thermal decomposition, these sustainable non-aqueous, low-temperature 'green' methods are used. Chemical oxidation was performed to obtain desodiated samples using NO_2BF_4 (Alfa Aesor, 96%) oxidant dissolved in acetonitrile solvent (Wako, H_2O level < 5 ppm). The solution was stirred overnight (with steady Ar flow) and the final products were filtered and dried at 60 °C under vacuum.

X-ray powder diffraction patterns were acquired in the 2θ range of 10-80° by a Bruker AXS D8 ADVANCE powder diffractometer equipped with a Co Kα radiation source operating at 35 kV and 40 mA. Synchrotron powder X-ray diffraction data for Rietveld refinement was obtained under vacuum at the BL-4B2 beam line of Photon Factory (PF), High Energy Accelerator Research Organization (KEK), Tsukuba, Japan. The wavelength was calibrated to be 1.196179(10) Å. For all the XRD measurements, samples were mounted on an air-tightened custom-designed sample holder, which was covered with polyimide film inside an Ar-filled glovebox to avoid any undesirable influence of air exposure.

The determination of the peak positions and indexing were carried out with TOPAS-Academic Ver. 4.1 program. The structure of sodium iron sulfate was solved by S. Nishimura using the parallel tempering algorithm[17] available in the global optimization program FOX[18], where tetrahedral constraints are applied to SO_4 units. The positions and occupancies were refined by subsequent Rietveld refinement using TOPAS program, and the final structure was illustrated with VESTA software[19]. The BVS for Na is calculated for whole space in the unit cell of the sodium iron sulfate within a grid resolution of 0.1 Å. The modified "soft-BV" parameters are used by utilizing an expanded evaluation range of the bonding interaction; r_0 = 1.5602 and B = 0.483 for Na–O bond.28 The penalty term of asymmetric coordinate was neglected. The Mössbauer spectra were taken with a Topologic System Inc. spectrometer with a ^{57}Co γ–ray source, calibrated with α–Fe as standard. The model fitting was performed with MossWinn 3.0 software. Particle morphology of powder samples was analyzed by a Hitachi S-4800 field-emission scanning electron microscope (FE-SEM) operating at 2 kV.

For electrochemical tests, the cathode was formulated by mixing 85 wt% $Na_2Fe_2(SO_4)_3$ active material, 10 wt% carbon black (Ketjen Black, Lion Corp., ECP) and 5 wt% polytetrafluoro-ethylene (PTFE) binder. This cathode tape was pressed onto an Al mesh with an average cathode loading of ca. 10 mg/cm^2. Beaker-type three electrode cells were assembled inside an Ar-filled glove box by taking the cathode film as the working electrode and Na metal foils acting as counter and reference electrodes.

These beaker cells were filled with 1 M $NaClO_4$ dissolved in propylene carbonate (PC). Galvanostatic charge-discharge cycling was conducted in the voltage ranges, 2.0~4.5 V, at different rates from C/20 to 20 C (at 25 °C). Rate capability tests were carried out using 2032-type coin cells with Na metal anode. Composite positive electrodes of 85 wt% active materials, 10 wt% ECP and 5 wt% polyvinylidene fluoride (PVdF) were mixed in N-methylpyrrolidone (NMP). The slurry was uniformly casted on an Al foil with an average loading of ca. 3 mg/cm^2, and dried at 120 °C under vacuum. The electrolyte solution was 1.0 moldm^{-3} $NaPF_6$ dissolved in a mixture of ethylene carbonate (EC)/ diethyl carbonate (DEC) (5:5 by vol., Kishida Chemical) with 2 vol% of fluorinated ethylene carbonate (FEC) (Kishida Chemical) as an electrolyte additive.[20] A glass fibre filter (GB-1000R, ADVANTEC) was used as a separator. The coin cells were discharged to

1.5 V at different rate from C/20 to 20 C. Before each discharge, the cells were charged at C/20 to 4.2 V. In-situ X-ray diffraction: In-situ X-ray diffraction measurements were conducted on BL-3A at KEK-PF using synchrotron radiation (λ = 0.12 nm) at room temperature. Diffraction data (exposure time; 30 seconds) were collected with symmetrical reflection geometry by a 2D detector (PILATUS-100K, RIGAKU). As an electrode, 80 wt% cathode, 10 wt% ECP, and 10 wt% PTFE binder were mixed, pressed onto a 10 μm Al foil, and dried 120 ^{o}C under vacuum. An in-situ XRD cell (RIGAKU) filled with 1 M $NaClO_4$ dissolved PC electrolyte was assembled in the following order: Be window, the cathode tape on Al foil, a glass fibre filter, and Na metal. The cell was cycled in the voltage range of 2−4.2 V at C/5 current rate (at 25 ^{o}C).

4.3 Structure of a new sodium iron sulfate

The unknown crystal structure of this new cathode material was determined by synchrotron powder X-ray diffraction (Fig. 4.1). Rietveld refinement and Mössbauer data (Inset of Fig. 4.1) confirm trace amount of Fe(III) impurity phases (e.g. α–$FeSO_4$). Mössbauer spectrum of the pristine material, consisting only Fe(II)-species, could be fitted with two doublets having 1:1 intensity ratio, which can be assigned to two distinct crystallographic sites, Fe(1) and Fe(2). All the Bragg reflections were indexed in a monoclinic lattice assuming *C2/c* (No. 15) symmetry with lattice parameters a = 11.46964(8) Å, b = 12.77002(9) Å, c = 6.51179(5) Å, β = 95.2742(4) °, and V = 949.73(1) Å^3. Although non-stoichiometry was to be considered, the fitting was satisfactory (R_{wp} = 4.87 %, R_p = 3.94 %, R_{Bragg} = 1.58 %, and GOF = 1.74). The crystallographic data are summarized in Tables 4.1 and 4.2. Indexing and analysis adopting alternative *P21/c* symmetry with two Fe sites were also possible with very slight decrease in R_{Bragg}. Due to the negligible difference for the refinement indices, more symmetric *C2/c* symmetry is adopted.

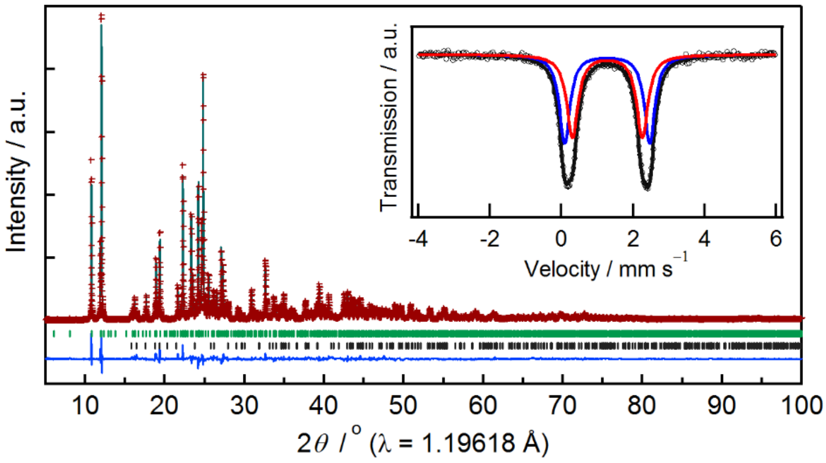

Figure 4.1 Rietveld refinement pattern of powder X-ray diffraction data for alluaudite sodium iron sulfate. Experimental data and calculated profile and their difference are shown as red crosses and black and blue solid lines, respectively. The theoretical Bragg positions of the alluaudite phase and the impurity phase (α-$FeSO_4$) are shown with green and black ticks. green ticks. (Inset) Room temperature Mössbauer spectrum of pristine sodium iron sulfate fitted with two distinctive iron species (blue and red lines).

Table 4.1 Crystallographic data of $Na_{2+2x}Fe_{2-x}(SO_4)_3$ with *C2/c* space group.

Chemical formula	$Na_{2.256}Fe_{1.872}(SO_4)_3$
M_r	444.57(2)
Crystal System, spece group	Monoclinic, *C* 2/*c* (No.15)
Temperature	~ 298 K (ambient)
a , *b* , *c* (Å)	12.65847 (7), 12.77062 (7), 6.51210 (3)
α , *β* , *γ* (Å)	90, 115.5391 (4), 90
V (Å^3)	949.86 (11)
Z	4
True density (g/cm^3)	3.10880(17)
Radiation type	Synchrotron λ = 1.196179(10) Å

Table 4.2 Fractional atomic coordinates, occupancies and isotropic displacement parameters.

Site	Wyckoff	*x* / *a*	*y* / *b*	*z* / *c*	occ.	*B* / Å^2
Na1	4*e*	1/2	0.7333 (2)	3/4	1.0	2.75(6)
Na2	4b	0	0	0	0.741 (5)	6.16(16)
Na3	4*e*	1/2	0.9874 (4)	1/4	0.563 (15)	4.87(19)
Fe1	8*f*	0.73096 (6)	0.15796 (6)	0.14721 (13)	0.9359 (13)	1.847 (19)
S1	4*e*	0	0.77639 (13)	3/4	1.0	1.81 (4)
O11	8*f*	0.0844 (2)	0.8456 (2)	0.7181 (4)	1.0	1.87(6)
O12	8*f*	0.4457 (2)	0.20944 (18)	0.5469 (4)	1.0	1.58(6)
S2	8*f*	0.76214 (11)	0.60305 (9)	0.8696 (2)	1.0	1.81(3)
O21	8*f*	0.76555 (18)	0.66917 (19)	0.6841 (4)	1.0	1.09(6)
O22	8*f*	0.3198 (2)	0.9958 (2)	0.3765 (4)	1.0	2.44(6)
O23	8*f*	0.3601 (2)	0.5869 (2)	0.6708 (5)	1.0	2.64(8)
O24	8*f*	0.3252 (2)	0.1578 (2)	0.0837 (5)	1.0	2.19(6)

The refined crystal structure of sodium iron sulfate is shown in Fig. 4.2. To the best of our knowledge, the composition and crystal structure of sodium iron sulfate are completely new and have never been reported in the literature. Deviating sharply from most of the $A_xM_2(XO_4)_3$–type compounds adopting the NASICON-related structures, sodium iron sulfate does not contain the lantern units $[M_2(XO_4)_3]$, forming a unique structure with alluaudite-type framework. It would be convenient to denote $AA'BM_2(XO_4)_3$ as general alluaudite-type compounds, where A = partially occupied Na(2), A' = partially occupied Na(3), B = Na(1), M = Fe^{2+}, and X = S in the present case. To the best of our knowledge, this is the first sulfate compound with alluaudite-type framework. The Fe-ions occupy octahedral sites that share edges with a crystallographically equivalent octahedron, forming Fe_2O_{10} dimer units. These isolated edge-sharing Fe_2O_{10} dimers are in turn bridged together by SO_4 units strictly by corner sharing mode, hence forming a three-dimensional framework with large tunnels along *c* axis. The constituent Na occupies three distinct crystallographic sites; one fully occupied and two partially occupied. This new structure-type should open up an entirely new $Na_{2-y}M_2(SO_4)_3$ (M = Mg, Ti, Mn, Co, Ni, V, and VO) family of compounds as potential cathodes/ anodes/ solid electrolytes for further material exploration.

Although $NaMnFe_2(PO_4)_3$ compounds with alluaudite-type $AA'BM_2(XO_4)_3$ framework of A, A' = partially occupied Na, B = Mn^{2+} and Fe^{2+}, M = Mn^{3+} and Fe^{3+} and X = P was previously synthesized[21], it showed weak electrochemical reactivity.

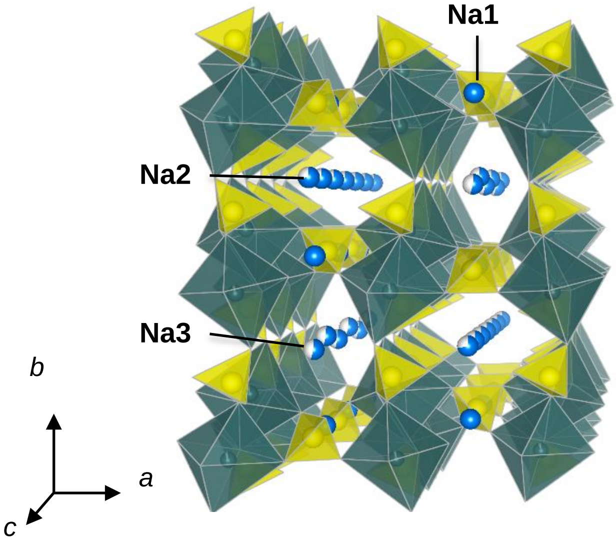

Figure 4.2 The crystal structure of alluaduite sodium iron sulfate projected along the *c* axis. Green octahedra, yellow tetrahedra and blue spheres show FeO_6, SO_4, and Na respectively.

4.4 Electrode properties as a sodium-ion battery cathode

The electrode properties of as-synthesized sodium iron sulfate were examined with no further optimization such as particle downsizing or carbon coating. The primary particle size was evaluated to be around 100-200 nm by SEM observation and the electrode loading was ca. 10 mg/cm^2. The corresponding voltage-capacity profiles for first few cycles between 2.0 - 4.5 V (vs. Na/Na^+) at a rate of C/20 (25 ^oC) is shown in Fig. 4.3 (i). The sodium iron sulfate cathode offers an average potential of 3.8 V (vs. Na/Na^+), which is the highest-ever Fe^{3+}/Fe^{2+} redox potential in any materials environment. The well-known NASICON-type $Fe(III)_2(SO_4)_3$[22] has same composition with desodiated $Na_2Fe_2(SO_4)_3$ in the present study, but NASICON phase delivers an average potential of 3.3 V (vs.Na/Na^+) upon Na insertion.[23]

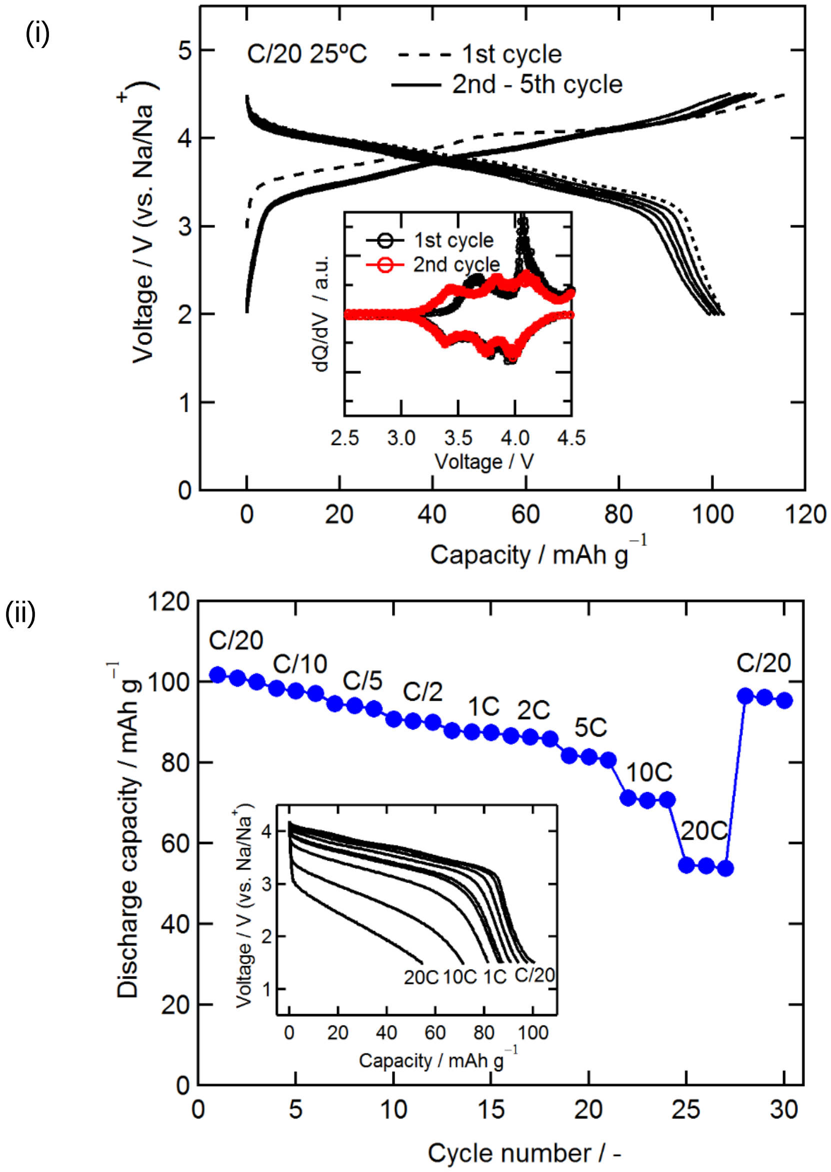

Figure 4.3 (i) Galvanostatic charging and discharging profiles of $Na_{2-y}Fe_2(SO_4)_3$ cathode cycled between 2.0 and 4.5 V at a rate of C/20 (2 Na in 20 h) at 25 ºC. 1st cycle is shown in dashed black line, and 2nd-5th cycle in solid black lines. (Inset) The differential galvanostatic profiles (d*Q*/d*V*) of $Na_{2-x}Fe_2(SO_4)_3$ cathode showing two distinctive peaks the first charge and broader three peaks upon subsequent discharging/charging processes. (ii) Capacity retention upon cycling up to 30 cycles under various rate of C/20 (2 Na in 20 h) to 20C (2 Na in 3 minute). (Inset) The discharge curves of $Na_{2-y}Fe_2(SO_4)_3$ as a function of rate (from C/20 to 20C). Before each discharge, the cells were charged at C/10 to 4.2 V.

Thereby, sodium iron sulfate cathode is characterized by three distinctive features: (i) totally new pristine composition with structure with edge-sharing FeO_6 octahedra different from NASICON- or NASICON-like phases with corner-sharing FeO_6 octahedra, (ii) initial valence state is Fe(II) with inherent existence of Na in the structure allowing to function as a cathode of Na-“ion” battery system, and (iii) much higher electrode potential by about 0.5 V comparing to the NASICON phases, providing very suitable average potential of 3.8 V (vs. Na/Na^+) with smooth sloppy charge-discharge profiles over a narrow voltage range in 3.3 – 4.3 V window. Features (i) and (ii) account for the abnormally high potential of sodium iron sulfate. The voltage E can be expressed as $E = \Delta G^{o} / n\mathrm{F} = (xG^{o}_{Na} + G^{o}_{Host} - G^{o}_{Na_{x}Host})/ \mathrm{nF}$, where n, F and G are number of electrons, Faraday constant and Gibbs free energy respectively. For sodium iron sulfate, the difference $G^{o}_{Host} - G^{o}_{NaxHost}$ is large since the sodiated state is synthesized as stable state (low $G^{o}Na_{xHost}$) while the desodiated one is electrochemical generated (possibly metastable) state (highG^{o}_{Host}). This is reverse for NASICON-type $Fe_2(SO_4)_3$ and any related Fe(III) cathodes.

Another factor, the edge sharing geometry of the Fe octahedra in the sodium iron sulfate, will push up G^{o}_{Host} due to the strong Fe^{3+}–Fe^{3+} repulsion, leading to high E.[24] This geometric characteristics can be found in other high-voltage materials such as triplite-type $LiFeSO_4F$[25] and $Li_2FeP_2O_7$[26]. In fact, the sodium iron sulfate has the shortest Fe–Fe distance among these materials. Thus, the average potential of 3.8 V by $Na_{2-y}Fe_2(SO_4)_3$ records the highest value among all Fe-based battery cathodes; it is even higher than those of Fe^{4+}/Fe^{3+} redox couple in simple oxides as $Na_{1-x}FeO_2$.

Surprisingly, it exceeds the highest record in lithium system in $Li_{1-x}FeSO_4F$, $Li_2FeP_2O_7$ and $Li_2Fe(SO_4)_2$ (around 3.9 V versus Li and hence 3.6 V versus Na).[25–27] Unlike the fluorosulphate cathodes, this high redox voltage is obtained without using electronegative-units that make the synthesis cumbersome and enhances hygroscopic/ instability in the final cathodes.

The initial reversible capacity of 102 $mAhg^{-1}$, which corresponds to 85 % of oneelectron theoretical capacity (ca. 120 $mAhg^{-1}$) based on Fe^{3+}/Fe^{2+} redox couple, was highly reversible over

30 cycles under various current rate and reasonable loading of ca.3 mg/cm^2 as the electrode (Fig. 4.3(ii)). Irreversible capacity of < 14 mAh/g (> 88 % charge/discharge efficiency) in Fig. 4.3 (i) may come from electrolyte decomposition as the cell was charged up to very high voltage, 4.5 V versus Na (4.8 V vs. Li/Li$^+$). When the current is further increased, 86 % (versus the value at C/20) of the initial capacity can be delivered in 1 h (1C), 85 % in 30 min (2C), and 70 % in 6 min (10C) as shown in Fig. 4.3(ii). This excellent high rate-capability of $Na_{2-y}Fe_2(SO_4)_3$ electrode suggests Na-ion migration in the framework structure is fast as will be discussed in the later section.

In spite of its high power operation and excellent cyclability, the voltage profile of the initial charge was slightly different from those of the subsequent cycles. During the first charge segment, the average redox reaction occurs at 3.9 V (vs. Na), which drops to 3.8 V in subsequent cycles. The differential galvanostatic profiles (dQ/dV) of $Na_{2-y}Fe_2(SO_4)_3$ cathode (inset of Fig. 4.3(i)) showing two distinctive peaks (3.65 and 4.06 V vs.Na/Na$^+$) at the first charge and broader three peaks (3.43, 3.48, and 4.10 V vs. Na/Na$^+$) upon subsequent discharging/charging processes. These indicates the occurrence of some irreversible structural transformation during first desodiation process, similar to the cases of Li_2FeSiO_4 and $Li_2FeP_2O_7$.[28] The sloping voltage curve over the entire range of Na composition suggests a single-phase homogeneous reaction mechanism involving minimal volume change. This hypothesis was verified by comparative X-ray diffraction patterns of the $Na_{2-y}Fe_2(SO_4)_3$ (y = 0–1.6) compositions prepared by chemical oxidation (Fig. 4.4 (i)) as well as by in-situ X-ray diffraction measurement during electrochemical charge/discharge (Fig. 4.5). Continuous shift of diffraction peaks with mere volume change (ΔV) of ca. −2 % was confirmed and in striking contrast to the Li_xFePO_4 system dominated by the twophase separation.[29] This is beneficial for long-term cycling, uniform reaction over the whole electrode, and longevity of the cathode involving less aggressive electromechanical grinding during its operation[30]. Such a small volume change in charge/discharge reaction may give another explanation for the high-rate capability but is quite surprising, considering much larger ionic radius of Na^+ than that of Li^+. Indeed, the $\Delta V = -17.6$ % in Na_xFePO_4 has been reported to be much larger than $\Delta V = -6.9$ % in Li_xFePO_4.[9,31] The sodium iron sulfate turns out to be an ideal host structure for efficient and fast Na^+ (de)insertion with unusually high Fe-redox potential.

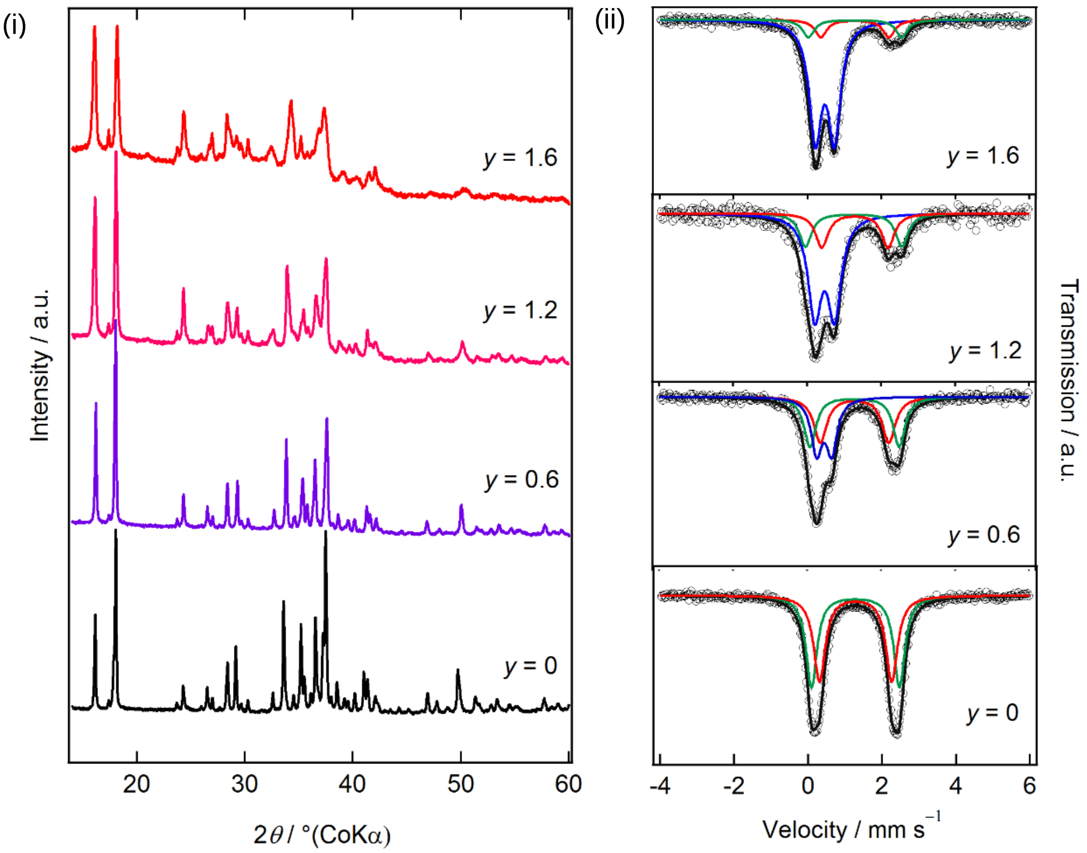

Figure 4.4 (i) X-ray diffraction patterns and (ii) Mössbauer spectra of the $Na_{2-y}Fe_2(SO_4)_3$ solid solution ($y = 0, 0.6, 1.2,$ and 1.6) prepared by chemical oxidation.

Table 4.3 Refined Mössbauer spectrum parameters of $Na_{2-y}Fe_2(SO_4)_3$ solid solution phases. Normalized χ^2 for each fitting were 1.34, 1.22, 1.04 and 1.02 for y = 0, 0.6, 1.2, and 1.6, respectively.

y in $Na_{2-y}Fe_2(SO_4)_3$		Isomer shift mm s^{-1}	Quadrupole splitting / mm s^{-1}	Fraction / %	Line width / mm s^{-1}
0	Fe^{2+}(1)	1.2798 (8)	2.378 (3)	50	0.356 (3)
	Fe^{2+}(2)	1.2798 (8)	1.954 (3)	50	0.382 (4)
	Fe^{3+}(3)	-	-	-	-
0.6	Fe^{2+}(1)	1.281 (4)	2.411 (7)	33.6 (4)	0.427 (1)
	Fe^{2+}(2)	1.281 (4)	1.852 (9)	33.6 (4)	0.389 (8)
	Fe^{3+}(3)	0.457 (3)	0.408 (8)	32.7 (5)	0.356 (8)
1.2	Fe^{2+}(1)	1.283 (1)	2.63 (3)	20.1 (3)	0.423 (2)
	Fe^{2+}(2)	1.283 (1)	1.81 (2)	20.1 (3)	0.433 (2)
	Fe^{3+}(3)	0.468 (5)	0.542 (9)	59.9 (9)	0.446 (1)
1.6	Fe^{2+}(1)	1.277 (8)	2.52 (2)	11.5 (4)	0.38 (1)
	Fe^{2+}(2)	1.277 (8)	1.83 (2)	11.5 (4)	0.38 (2)
	Fe^{3+}(3)	0.463 (1)	0.517 (3)	77.0 (6)	0.398 (4)

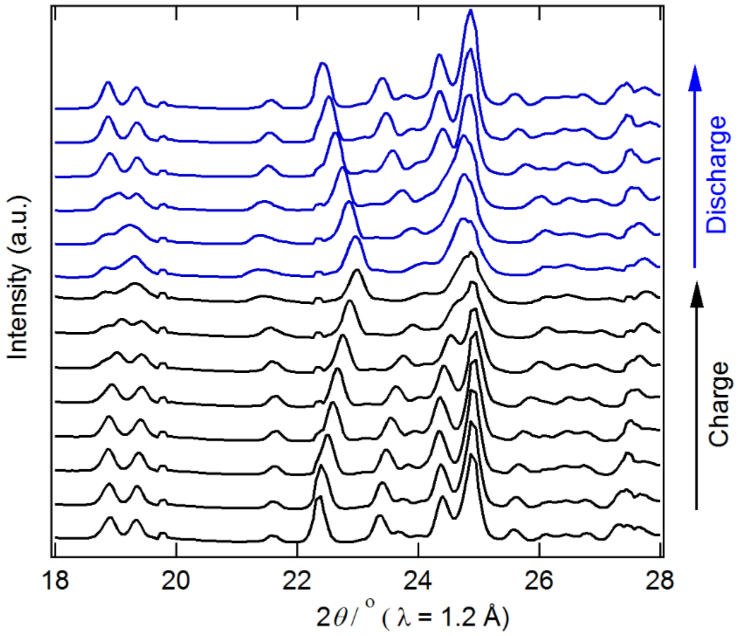

Figure 4.5 In-situ X-ray diffraction patterns of the $Na_{2-y}Fe_2(SO_4)_3$ during electrochemical charge and discharge at a rate of C/5 (3rd cycle).

4.5 Sodium diffusion pathways

To gain further insight on this suitable structure, Bond valence (BV) method was used to evaluate the validity of the crystal structure as well as to elucidate possible Na diffusion paths by utilizing the soft-BV parameters.[32,33] Difference of the bond valence sum from the ideal value (ΔBVS) provides a simple measure of positional suitability of mobile ions in solid frameworks.[34]

Figure 4.6 (i) and (ii) show ΔBVS maps as equi-value surfaces. Inner side of the equi-value surfaces show accessible spaces for Na^+ in the $[Fe_2(SO_4)_3]^{2-}$ framework. All the refined Na positions are consistent with the ΔBVS map. Whilst the Na1 and the Na2 looks to have rather localized character in the present analysis, the Na3 site are clearly permeating along the [001] direction.

Ab initio calculations were performed by Chung et al[35] to gain more quantitative understanding for Na diffusion. The calculations were conducted for the sodium poor region (detailed information for the computational method is in ref. 35). The activation energies for the Na ion migration within the Na3 channel indeed is found to be low, which is 0.28 eV (Fig. 4.6 (iii)). Liquid-like value of 0.14 eV was calculated for defect diffusion along the channel and is among the lowest for Na-ions conductors.[36] The value for the Na2 channel is 0.54 eV similar to that for $Na_2FeP_2O_7$, which shows very fast charge/discharge kinetics[10,37,38] For migrations between channels, the activation energies are 0.88 and 0.58 eV for back-and-forth transport between Na1 and Na2 sites, and they are 0.54 and 0.05 eV for that between Na1 and Na3. Therefore, it is postulate that this material has one-dimensional Na^+ conduction channels along the *c*-axis for both the Na2 and Na3 sites, while the Na1 ion can be extracted through the Na3 sites. As a result, all the Na ions are accessible for (de)intercalation reaction with no limitation toward theoretical capacity. In particular, the continuous space around Na3 site can act as a fast sodium transport channel during the charge discharge reaction, which can be the origin of excellent kinetics of $Na_2Fe_2(SO_4)_3$ cathode material. Similar technical strategies applied for Li_xFePO_4, which also shows one-dimensional diffusion[39], should be effective to enhance electrode performance such as diminishing defect density and minimizing particle size along *c*-axis.[40]

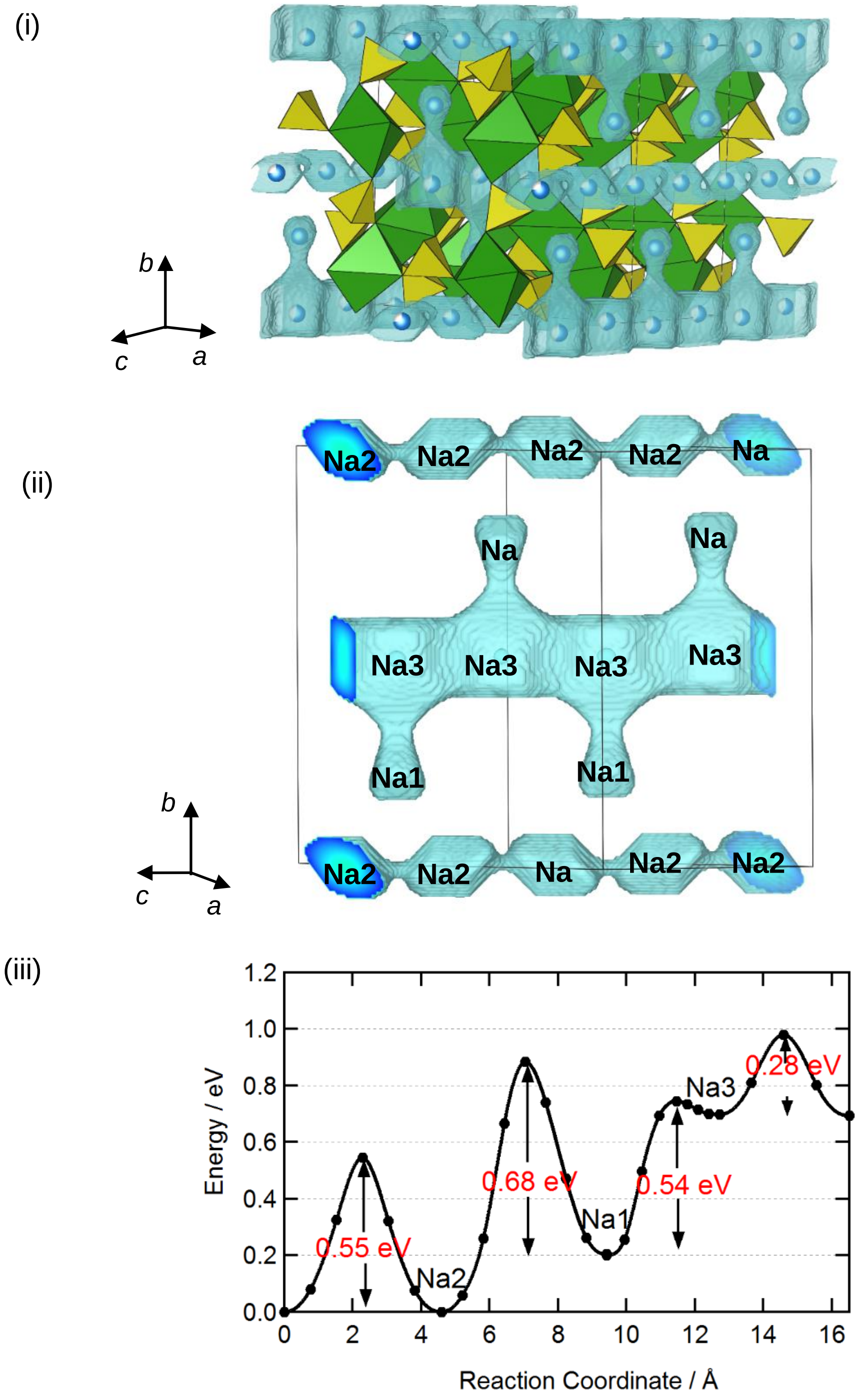

Figure 4.6 (i), (ii) Equi-value-surface of the ΔBVS (i) with and (ii) without FeO_6 and SO_4 units. Green and yellow polyhedra are that of FeO_6 and SO_4, respectively. The light-blue surfaces are for ΔBVS = 0.5. (iii) Migration activation energy of Na^+ ion calculated with DFT.[35] The red colored values (from left to right) are migration barriers along the *c* axis for

the Na2 sites, between Na2 and Na1 sites, between Na1 and Na3 sites and along the *c* axis for the Na3 sites.

4.6 Thermal stability

Finally, the material stability (chemical/ thermal/ storage) was examined. Similar to other sulphate-based cathodes (e.g. fluorosulphates, bisulphates), the sodium iron sulfate was found to dissolve completely in water. Thus, it is not stable in aqueous condition, a fact that was further verified by observation of its steady degradation upon long time moisture exposure (in ambient condition) to form a hydrated derivative $Na_2Fe(SO_4)_2{\cdot}4H_2O$.

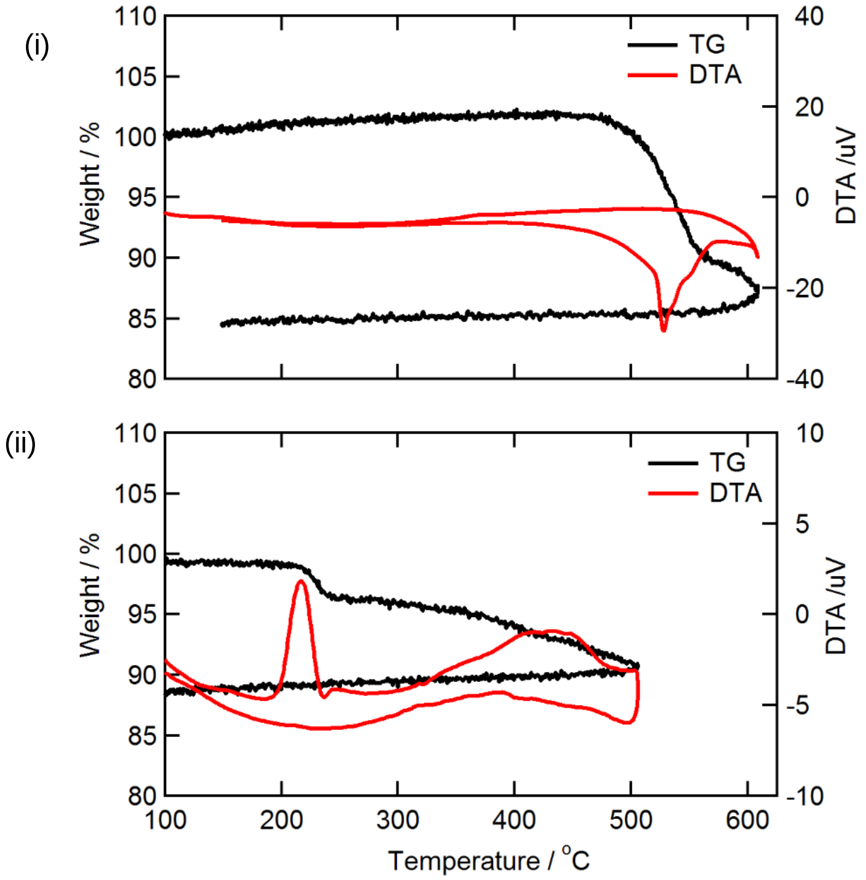

Figure 4.7 TG-DTA curves for (i) pristine and (ii) desodiated phases. Black and red solid lines show TG and DTA curves, respectively.

Nevertheless, with minimal exposure of freshly prepared sample to ambient air and careful packaging/ storage (in inert atmosphere), this metastable compound remains intact with no deterioration in its electrochemical properties. Further, the thermal analysis (TG-DTA) of sodium iron sulfate noticed gradual weight loss upon heating above 450 °C with simultaneous decomposition of SO_4 units, release of SO_2 gas and oxidation of Fe^{2+} species leading to the formation of Na_2SO_4, Fe_2O_3 and Fe_3O_4. In spite of this thermal decomposition above 450 °C, it should be noted that sodium iron sulfate compound offers sufficient thermal stability of real-life battery applications.

4.7 Conclusion

Searching for novel low-cost cathode materials for rechargeable Na-ion batteries, a whole new family of cathode materials with general formula $Na_2M_2(SO_4)_3$ is synthesized. The first such candidate, Fe-based sodium iron sulfate, delivers a reversible capacity exceeding 100 $mAh.g^{-1}$ with the working Fe^{3+}/Fe^{2+} potential located at 3.8 V (vs.Na/Na^+), the highest known value among all Fe-based insertion compounds. This abnormally high-voltage is compatible with the thermodynamic limit of current generation organic electrolytes offering stable/safe operation. Additionally, it offers excellent rate kinetics and cycling stability without demanding any additional cathode optimization. It forms an open framework host for efficient (de)intercalation of Na ions with very low activation energy. Average potential and reversible capacity of various known iron based cathode for sodium-ion (inherent sodium within structure as whole sodium source) battery system are summarized in Fig. 4.8. The new material $Na_2Fe_2(SO_4)_3$ is benchmarking and worth further optimizing as it is the first Fe-based cathode for sodium battery to offer high-voltage compatible with lithium battery system. Moreover, further effort to reach theoretical capacity by full utilization of inherent Na ions (85 % in the present paper) can lead to energy density comparable to those of olive $LiFePO_4$ and spinel $LiMn_2O_4$.

Complementing this electrode performance, the alluaudite sodium iron sulfate can be easily prepared and up scaled by low-temperature solid-state methods, though care should be taken on the hygroscopic nature. The sustainability of sodium iron sulfate further arises from its economic Na–Fe–S–O elemental constitution. In earth's upper crust, Na and Fe are the most abundant and geographically distributed alkali and (3d) transition metal respectively.

Talking about sulphur and sulphate compounds, they are very economic and widely used in fertilizers, pesticides and chemical industries. In fact, they are extremely cheap, being a byproduct of fuel combustion, coal power plants and oil/ petrochemical industries.

Thus, the sodium iron sulfate form an ideal material for economic production and large-scale battery manufacturing. The author strongly believe the sodium iron sulfate cathode will not only open up a new sub-group of polyanionic cathodes with commercial potential, but also inspire future success in discovering superior electrode materials for next generation secondary batteries.

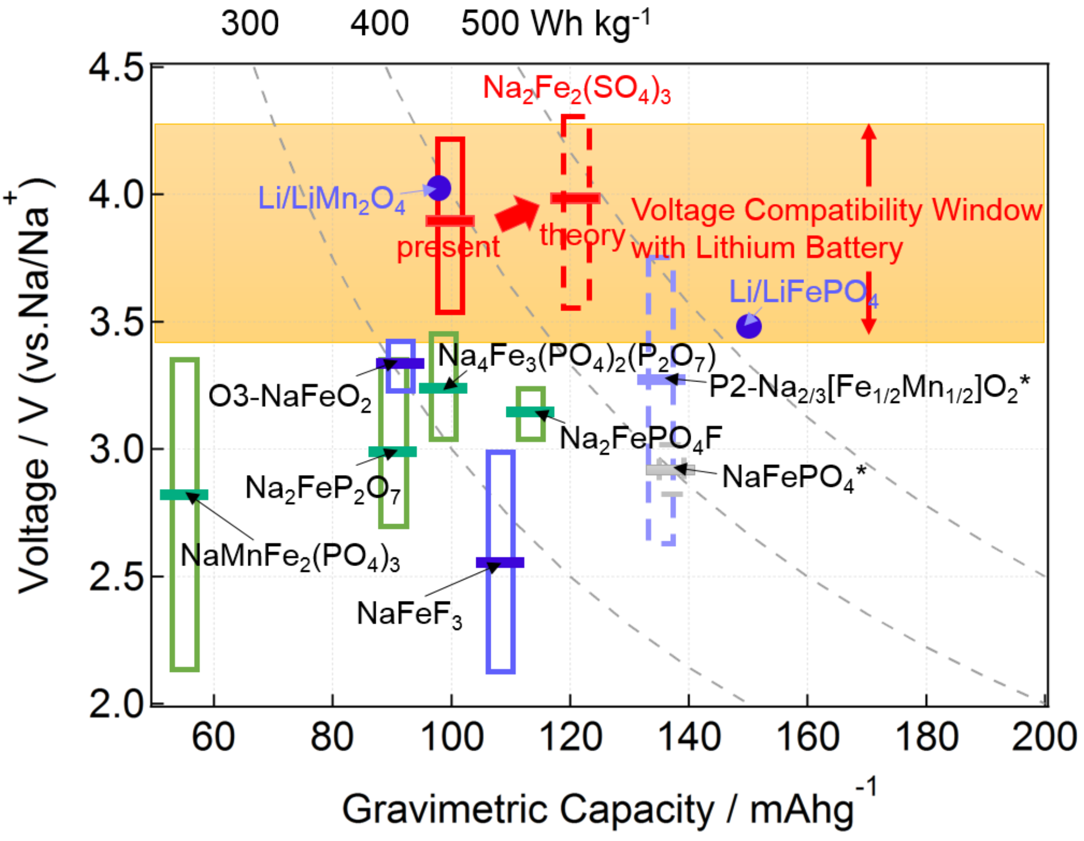

Figure 4.8 Comparison of electrode performances among iron-based cathode materials which can function as sodium source in sodium-ion battery. Average potentials of polyanionic compounds are shown as green solid boxes and simple oxides/fluorides as blue, respectively. Yellow band indicates voltage region, which can ensure the compatibility with

Li-ion batteries. The new compound alluaudite $Na_2Fe_2(SO_4)_3$ is presented by the red box together with its expected dashed-red region based on the theoretical capacity.

References

(1) Mizushima, K.; Jones, P. C.; Wiseman, P. J.; Goodenough, J. B. *Mater. Res. Bull.* **1980**, *15*, 783–789.

(2) Thackeray, M. M.; David, W. I. F.; Bruce, P. G.; Goodenough, J. B. *Mater. Res. Bull.* **1983**, *18*, 461–472.

(3) Padhi, A. K.; Nanjundaswamy, K. S.; Goodenough, J. B. *J. Electrochem. Soc.* **1997**, *144*, 1188–1193.

(4) Tarascon, J.-M. *Nat. Chem.* **2010**, *2*, 510.

(5) Delmas, C.; Braconnier, J.; Fouassier, C.; Hagenmuller, P. *Solid State Ionics* **1981**, *3-4*, 165–169.

(6) Komaba, S.; Murata, W.; Ishikawa, T.; Yabuuchi, N.; Ozeki, T.; Nakayama, T.; Ogata, A.; Gotoh, K.; Fujiwara, K. *Adv. Funct. Mater.* **2011**, *21*, 3859–3867.

(7) Yabuuchi, N.; Kajiyama, M.; Iwatate, J.; Nishikawa, H.; Hitomi, S.; Okuyama, R.; Usui, R.; Yamada, Y.; Komaba, S. *Nat. Mater.* **2012**, *11*, 512–517.

(8) Ellis, B. L.; Makahnouk, W. R. M.; Makimura, Y.; Toghill, K.; Nazar, L. F. *Nat. Mater.* **2007**, *6*, 749–753.

(9) Moreau, P.; Guyomard, D.; Gaubicher, J.; Boucher, F. *Chem. Mater.* **2010**, *22*, 4126–4128.

(10) Barpanda, P.; Ye, T.; Nishimura, S.; Chung, S.-C.; Yamada, Y.; Okubo, M.; Zhou, H.; Yamada, A. *Electrochem. commun.* **2012**, *24*, 116–119.

(11) Kim, H.; Park, I.; Seo, D.-H.; Lee, S.; Kim, S.-W.; Kwon, W. J.; Park, Y.-U.; Kim, C. S.; Jeon, S.; Kang, K. *J. Am. Chem. Soc.* **2012**, *134*, 10369–10372.

(12) Whittingham, M. S. *Science (80-.).* **1976**, *192*, 1126–1127.

(13) Takeda, Y.; Nakahara, K.; Nishijima, M.; Imanishi, N.; Yamamoto, O.; Takano, M.; Kanno, R. *Mater. Res. Bull.* **1994**, *29*, 659–666.

(14) Yabuuchi, N.; Yoshida, H.; Komaba, S. *Electrochemistry* **2012**, *80*, 716–719.

(15) Barpanda, P.; Chotard, J.-N.; Recham, N.; Delacourt, C.; Ati, M.; Dupont, L.; Armand, M.; Tarascon, J.-M. *Inorg. Chem.* **2010**, *49*, 7401–7413.

(16) Ati, M.; Dupont, L.; Recham, N.; Chotard, J.-N. J. N.; Walker, W. T.; Davoisne, C.; Barpanda, P.; Sarou-Kanian, V.; Armand, M.; Tarascon, J.-M. J. M. *Chem. Mater.* **2010**, *22*, 4062–4068.

(17) Falcioni, M.; Deem, M. W. *J. Chem. Phys.* **1999**, *110*, 1754.

(18) Favre-Nicolin, V.; Černý, R. *J. Appl. Crystallogr.* **2002**, *35*, 734–743.

(19) Momma, K.; Izumi, F. *J. Appl. Crystallogr.* **2011**, *44*, 1272–1276.

(20) Komaba, S.; Ishikawa, T.; Yabuuchi, N.; Murata, W.; Ito, A.; Ohsawa, Y. *ACS Appl. Mater. Interfaces* **2011**, *3*, 4165–4168.

(21) Trad, K.; Carlier, D.; Croguennec, L.; Wattiaux, A.; Ben Amara, M.; Delmas, C. *Chem. Mater.* **2010**, *22*, 5554–5562.

(22) Manthiram, A.; Goodenough, J. B. *J. Power Sources 26*, 403–408.

(23) Okada, S.; Arai, S.; Yamaki, J. *Denki Kagaku* **1997**, *65*, 802–807.

(24) Chung, S. C.; Barpanda, P.; Nishimura, S.; Yamada, Y.; Yamada, A. *Phys. Chem. Chem. Phys.* **2012**, *14*, 8678.

(25) Barpanda, P.; Ling, C. D.; Oyama, G.; Yamada, A. *Acta Crystallogr. Sect. B Struct. Sci. Cryst. Eng. Mater.* **2013**, *69*, 584–588.

(26) Nishimura, S.; Nakamura, M.; Natsui, R.; Yamada, A. *J. Am. Chem. Soc.* **2010**, *132*, 13596–13597.

(27) Reynaud, M.; Ati, M.; Melot, B. C.; Sougrati, M. T.; Rousse, G.; Chotard, J.-N.; Tarascon, J.-M. *Electrochem. commun.* **2012**, *21*, 77–80.

(28) Ye, T.; Barpanda, P.; Nishimura, S.; Furuta, N.; Chung, S.-C.; Yamada, A. *Chem. Mater.* **2013**, *25*, 3623–3629.

(29) Yamada, A.; Koizumi, H.; Nishimura, S.; Sonoyama, N.; Kanno, R.; Yonemura, M.; Nakamura, T.; Kobayashi, Y. *Nat. Mater.* **2006**, *5*, 357–360.

(30) Wang, Y.; Yu, X.; Xu, S.; Bai, J.; Xiao, R.; Hu, Y.-S.; Li, H.; Yang, X.-Q.; Chen, L.; Huang, X. *Nat. Commun.* **2013**, *4*.

(31) Lu, J.; Chung, S. C.; Nishimura, S.; Yamada, A. *Chem. Mater.* **2013**, 131029074415004.

(32) Brown, I. D. *The Chemical Bond in Inorganic Chemistry: The Bond Valence Model*; Oxford University Press, Ed.; 12th ed.; 2002.

(33) Adams, S. *Acta Crystallogr. B.* **2001**, *57*, 278–287.

(34) Adams, S. *Solid State Ionics* **2006**, *177*, 1625–1630.

(35) Barpanda, P.; Oyama, G.; Nishimura, S.; Chung, S.-C.; Yamada, A. *Nat. Commun.* **2014**, *5*, 4358.

(36) Ong, S. P.; Chevrier, V. L.; Hautier, G.; Jain, A.; Moore, C.; Kim, S.; Ma, X.; Ceder, G. *Energy Environ. Sci.* **2011**, *4*, 3680.

(37) Clark, J. M.; Nishimura, S.; Yamada, A.; Islam, M. S. *Angew. Chem. Int. Ed. Engl.* **2012**, *51*, 13149–13153.

(38) Kim, H.; Shakoor, R. A.; Park, C.; Lim, S. Y.; Kim, J.-S.; Jo, Y. N.; Cho, W.; Miyasaka, K.; Kahraman, R.; Jung, Y.; Choi, J. W. *Adv. Funct. Mater.* **2013**, *23*, 1147–1155.

(39) Nishimura, S.; Kobayashi, G.; Ohoyama, K.; Kanno, R.; Yashima, M.; Yamada, A. *Nat. Mater.* **2008**, *7*, 707–711.

(40) Malik, R.; Zhou, F.; Ceder, G. *Nat. Mater.* **2011**, *10*, 587–590.

5. Off-stoichiometry in Alluaudite-type Sodium Iron Sulfate $Na_{2+2x}Fe_{2-x}(SO_4)_3$ as an Advanced Sodium Battery Cathode Material

5.1 Introduction

Large-scale electrochemical energy storage has been demanded for its use in the power grid. Low-cost, high power and efficient batteries can load-level the intermittent power from renewable power sources, making energy consumption sustainable. Sodium-ion batteries are promising candidates owing to abundance, fast diffusion, and facile interfacial kinetics of sodium-ion.[1,2] Cathode materials for Na-ion batteries are currently under extensive investigation, particularly for those consisting of relatively low cost transition metals (Fe and Mn) such as P2-$Na_xMn_{0.5}Fe_{0.5}O_2$, O3-$NaFe_{0.5}Ni_{0.5}O_2$, Na_2FePO_4F, and $Na_2FeP_2O_7$.[3–7] Of particular importance for large-scale applications is to utilize Fe as a lightweight redox center in the solid matrix, because Fe has much less environmental impact owing to the fourth most abundance and wide distribution in the earth. However, their operating potential in the Na system is generally too low to achieve high energy density. In the Li system, the operating potential with Fe has been rationally raised up to 3.9 V (versus Li/Li^+) by controlling ionicity of Fe–ligand bonds.[8] Thus the author expects that extension of rational strategies in the Li system to the Na system leads to > 3.6 V (versus Na/Na^+) operation. According to the well-established rational strategies in the Li system, to exploit an inductive effect of SO_4^{2-} is potentially effective for realizing high voltage cathodes in the Na system. Compared with the other oxyanionic compounds such as silicates and phosphates, the sulfate compounds generally have more ionic M–O bonds, leading to the high operating potential.[9] For example, tavorite $LiFeSO_4F$, triplite $LiFeSO_4F$, marinate $Li_2Fe(SO_4)_2$ and orthorhombic $Li_2Fe(SO_4)_2$ show high average redox potential of 3.6, 3.9, 3.83 and 3.79 V versus Li/Li^+, respectively.[10–13] Concerning the present set of sodium-ion cathode materials, α-$NaFeSO_4F$ and kröhnkite $Na_2Fe(SO_4)_2·2H_2O$ have been explored, but their electrochemical activity is limited to date. [14–16]

Recently, a new material, an alluaudite-type sodium iron sulfate $Na_2Fe_2(SO_4)_3$ has been discovered as a promising cathode material for sodium-ion batteries.[17] This material delivers the specific capacity of about 100 mAh g^{-1} with good cycle retention, while 70% of the capacity at C/20 rate is retained at a high rate of 10 C. The average potential is around 3.8 V vs. Na/Na^+ (and hence 4.1 V vs. Li/Li^+), the highest value among all Fe-based compounds, even exceeding the highest record in the Li system. Thereby, the theoretical energy density of alluaudite $Na_2Fe_2(SO_4)_3$ is extremely high (> 540 Wh kg^{-1} vs. Na/Na^+) enough to make Na-ion batteries competitive with the state-of-the-art Li-ion batteries.

Despite the superior electrode performance of alluaudite $Na_2Fe_2(SO_4)_3$, phase equilibrium of Na_2SO_4–$FeSO_4$ system has not been investigated to date, partly due to the thermal decomposition of iron(II) sulfates above ca. 700 K. As was reported in the original paper,[16] an excess amount of sodium sulfate in the precursor mixture is necessary to reduce the amount of impurities, suggesting the existence of off-stoichiometry such as $Na_{2+2x}Fe_{2-x}(SO_4)_3$.

Here, the phase equilibrium of Na_2SO_4–$FeSO_4$ system is targeted, and off-stoichiometric alluaudite $Na_{2+2x}Fe_{2-x}(SO_4)_3$ is isolated. Structural details of the compounds will be reported.

5.2 Experimental methods

The samples targeted for $Na_{2+2x}Fe_{2-x}(SO_4)_3$ was synthesized via a solid-state method. Dehydrated $FeSO_4$ was obtained by calcination of $FeSO_4·7H_2O$ (Kanto chemical co., 99%) under vacuum at 573 K for 12 h. $FeSO_4$ and anhydrous Na_2SO_4 (Wako, 99%) were ball-milled for 6 h with acetone. The milled precursor was dried under vacuum, followed by heating at 623 K for 24 hours under continuous Ar gas flow. The mixture was re-milled and re-heated at 623 K for 24 hours to minimize the amount of impurity phases.

Powder X-ray diffraction (XRD) patterns were obtained at 2θ = 10–60° by a RIGAKU

RINT-TTR III powder diffractometer with a Cu Kα radiation source. High resolution-XRD (HR-XRD) pattern was acquired at a beam line 4B2 of Photon Factory (PF), High Energy Accelerator Research Organization (KEK), Tsukuba, Japan. The measurements were performed under vacuum to avoid moisture contamination. Rietveld refinements were carried out with TOPAS-Ver. 3.0. The wavelength was calibrated to be 1.19670(5) Å.

The Mössbauer spectra were taken by Topologic System Inc. spectrometer with a ^{57}Co/Rh γ–ray source at room temperature. The velocity was calibrated by α-Fe as standard. The samples were sealed in Ar filled polyethylene films. The spectrum was analyzed with the Moss Winn (version 3.0) software.

5.3 Materials exploration in the Na_2SO_4-$FeSO_4$ binary phase

In general, iron(II) sulfate compounds are unstable above ca. 700 K, because they decompose with evolution of SO_2 and/or SO_3 gases.[9] In this work, a combination of mechanical pre-activation by ball-milling and the subsequent low-temperature solid-state reaction is employed.[16] The ball-milled precursor mixtures with the initial compositions of $(2 - x)FeSO_4 + (1 + x) Na_2SO_4$ ($0 \leq x \leq 0.4$) were heated at 623 K.

Figure 5.1 (i) shows the powder XRD patterns for the products targeted for $Na_{2+2x}Fe_{2-x}(SO_4)_3$ ($x = 0$–0.4), where the $x = 0$ corresponds to the composition of the stoichiometric alluaudite $Na_2Fe_2(SO_4)_3$. Most reflections are assigned to the alluaudite phase, but several reflections which remain unassigned by the alluaudite phase are attributable to two polymorphs of sodium-free iron(II) sulfate, α-, β- $FeSO_4$ and magnetite Fe_3O_4. On the basis of the Rietveld refinement, the total amount of α-, β- $FeSO_4$ and Fe_3O_4 in the product targeted for $x = 0$ exceeds 15 wt% (Fig. 5.1(ii)). The refined XRD pattern and R-factors (Fig. 5.2) show the fitting was satisfactory. Thus, in order to purify alluaudite sodium iron sulfate, an excess amount of sodium is necessary in the precursor mixture, presumably due to the off-stoichiometry of the alluaudite phase.

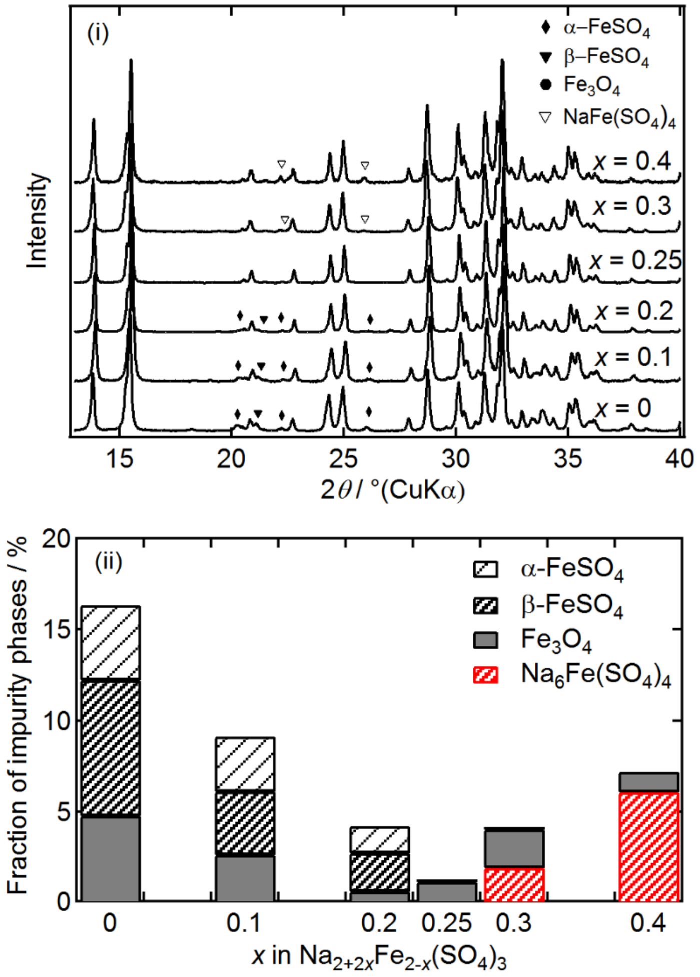

Figure. 5.1 (i) Powder X-ray diffraction (XRD) patterns of the products targeted for $Na_{2+2x}Fe_{2-x}(SO_4)_3$ ($x = 0 - 0.4$). Black triangles, rhombus circle and white triangles indicate peaks of α-$FeSO_4$, β-$FeSO_4$, Fe_3O_4 and $Na_6Fe(SO_4)_4$,respectively. (ii) Weight fraction of impurity phases derived by Rietveld refinements for XRD patterns of the products targeted for $Na_{2+2x}Fe_{2-x}(SO_4)_3$.

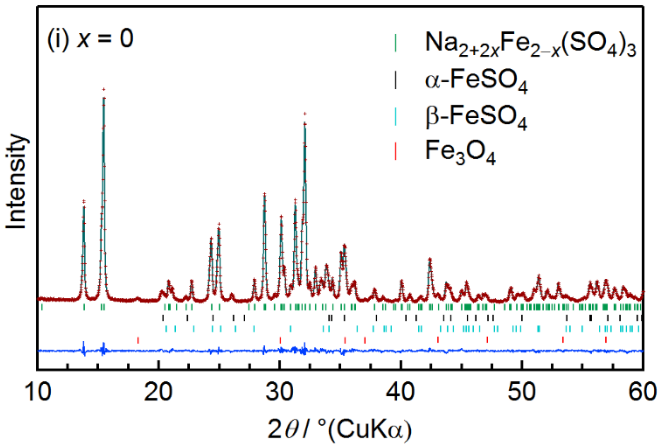

$R_{wp} = 0.0816$, $R_p = 0.0583$, $GoF = 1.24$, and $R_{Bragg} = 0.0170$

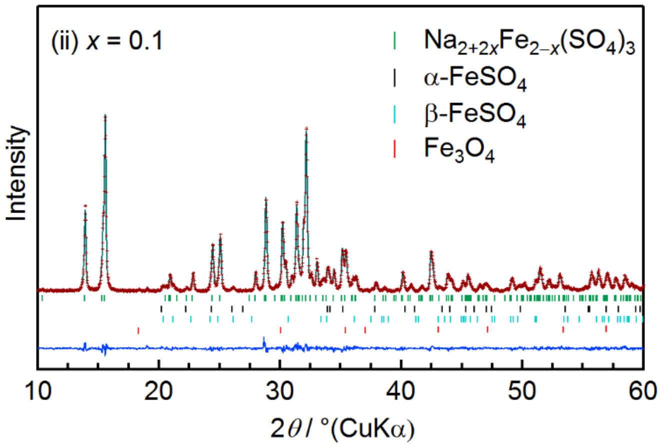

$R_{wp} = 0.0602$, $R_p = 0.0450$, $GoF = 1.32$, and $R_{Bragg} = 0.0152$

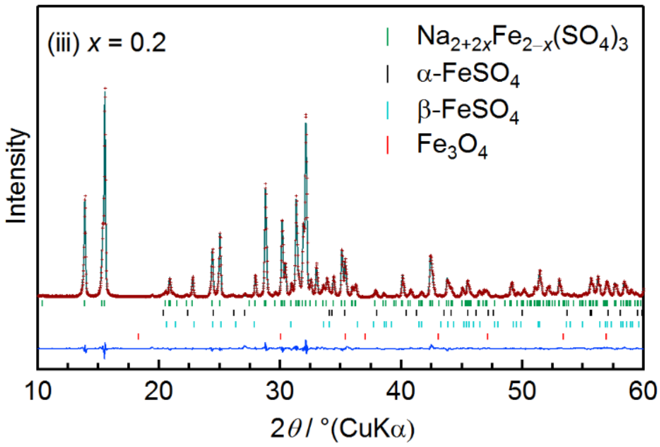

$R_{wp} = 0.0561$, $R_p = 0.0403$, $GoF = 2.52$, and $R_{Bragg} = 0.0197$

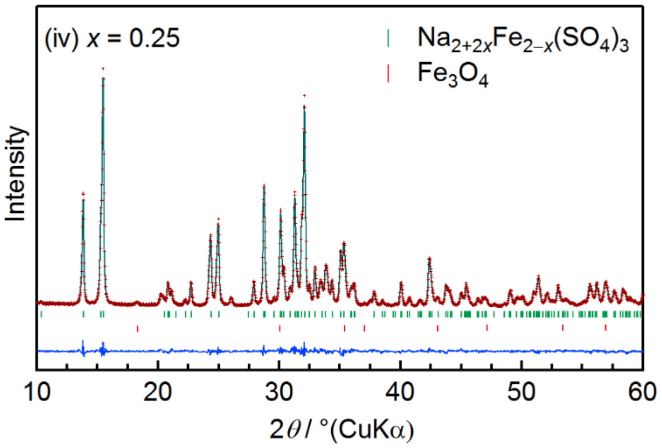

R_{wp} = 0.103, R_p = 0.0722, GoF = 1.22, and R_{Bragg} = 0.0222

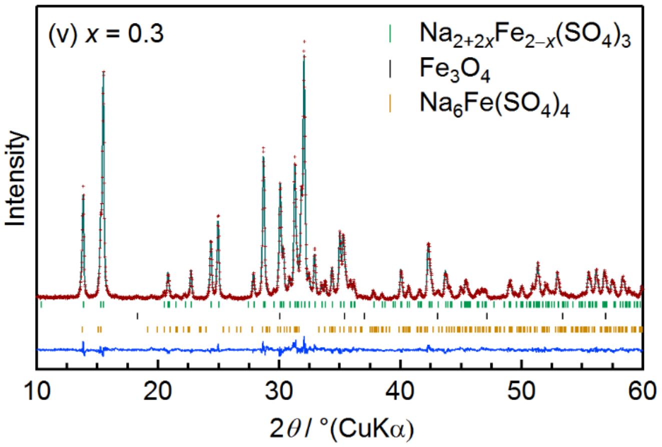

R_{wp} = 0.0745, R_p = 0.0553, GoF = 1.27, and R_{Bragg} = 0.0223

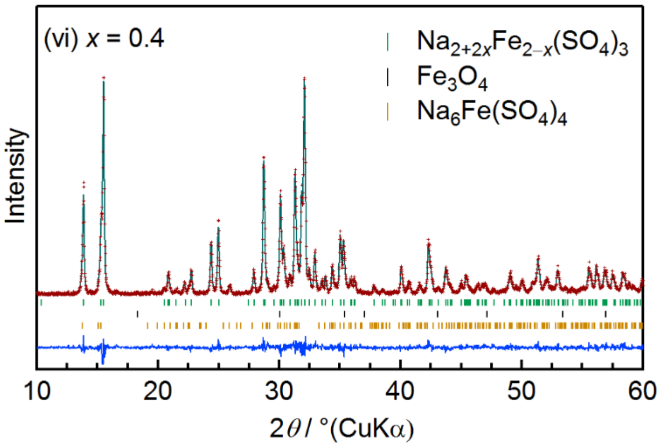

R_{wp} = 0.101, R_p = 0.0875, GoF = 1.21, and R_{Bragg} = 0.0369

Figure 5.2 (i)-(iv) Refined XRD patterns for the product targeted for $Na_{2+2x}Fe_{2-x}(SO_4)_3$ (x = 0 – 0.4), and refinement indices for each fitting. (R_{Bragg} factors of $Na_{2+2x}Fe_{2-x}(SO_4)_3$ phase are shown.)

5.4 Composition range of $Na_{2+2x}Fe_{2-x}(SO_4)_3$

Indeed, with increasing x, reflections from the impurities become weak, while the peak position of the alluaudite phase does not shift significantly. The lattice parameters for the alluaudite phase as a function of x (Fig. 5.3) show small change; the volume change is less than 0.7 % for $0 \leq x \leq 0.4$. In contrast, the weight fraction of the impurity phases decreases from 16 wt% at $x = 0$ to1.2 wt% at $x = 0.25$. As x increases above 0.3, the lattice parameters change was negligible and new impurity peaks appear around $2\theta = 24.5$, 26 and 30.5°. The peaks are assigned to a sodium rich phase $Na_6Fe(SO_4)_4$, which is isostructural to vanthoffite $Na_6Mg(SO_4)_4$.[18] These trends indicate that the stoichiometric $Na_2Fe_2(SO_4)_3$ is not stable in the present synthetic condition, but off-stoichiometric alluaudite $Na_{2+2x}Fe_{2-x}(SO_4)_3$ of x = ca. 0.25-0.3 is formed. It should be mentioned that Reynaud et al. demonstrated existence of $Na_2Fe(SO_4)_2$ ($x = 0.5$ in $(2 - x)$ $FeSO_4$ + $(1 + x)Na_2SO_4$) as a decomposition product from the hydrated sodium iron sulfate $Na_2Fe(SO_4)_2{\cdot}4H_2O$.[19] This phase might be metastable, because $Na_2Fe(SO_4)_2$ was not observed in our synthetic conditions. A schematic phase relation in the Na_2SO_4-$FeSO_4$ system based on the present body of knowledge is presented in Scheme 5.1.

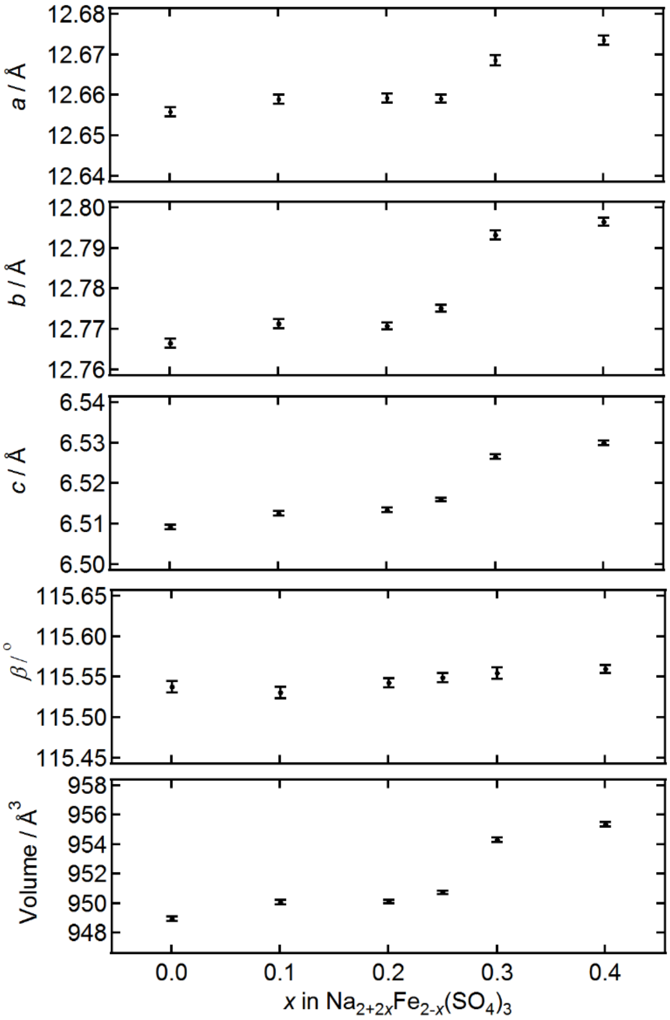

Figure 5.3 Lattice parameters of the products targeted for $Na_{2+2x}Fe_{2-x}(SO_4)_3$ as a function of x.

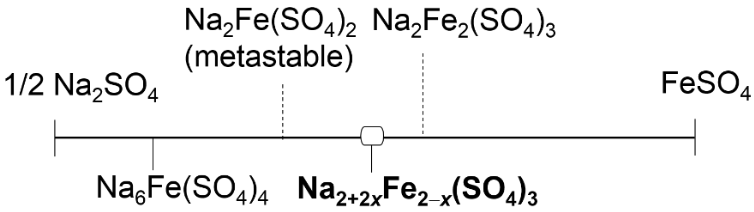

Scheme 5.1 Schematic phase relation in Na_2SO_4–$FeSO_4$ system based on present knowledge.

The ^{57}Fe Mössbauer spectroscopy was applied to clarify the amount of the impurity phase and the exact composition of the product targeted for x = 0.25. The spectrum (Fig. 5.4) was analyzed by three components. The predominant component is a high-spin Fe(II) at a six-coordinated environment, which was assigned to the alluaudite phase. A distribution of quadrupole splitting (QS) was adopted to account a broad line profile with the fixed full width at half-maximum (0.25 mm s^{-1}). The fitting parameters are shown in Table 5.1. The QS distribution (Inset of Fig. 5.4) indicates the inequivalent electric field gradient (EFG) at the each Fe site due to variety of local environments (ex. coordination number, degree of covalency, and symmetry of coordination, etc.). Here, the main source of the large EFG distribution is various possibility of Na arrangement around the Fe (The details are to be mentioned later). The QS distribution was even broader than that of isostructural $NaMnFe_2(PO_4)_3$.[20] The other components (the green dashed line in Fig. 5.4) were typical two magnetic Fe species in the Fe_3O_4. The IS and QS values of Fe_3O_4 phase were fixed to the reported value.[21] Note the difference of Mössbauer recoilless fraction is assumed to be negligible among the observed species. At final refinement, 4.1 atom% of Fe are attributed to Fe_3O_4. Thus, the calculated composition of the obtained alluaudite phase is described as $Na_{2.56}Fe_{1.72}(SO_4)_3$, which is significantly different from those of the reported alluaudite-type phosphates (e.g. AMnFe$_2$(PO$_4$)$_3$ (A = Na, Li)[20,22], Na$_2M_3$(PO$_4$)$_3$ (M = Fe, Mn, Ni[23–25]).

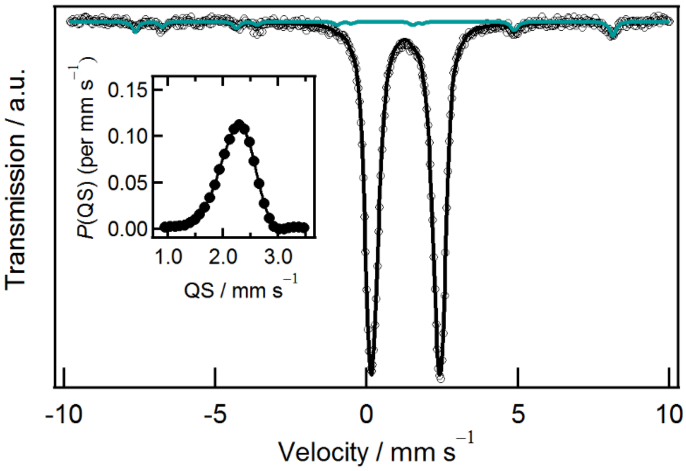

Figure 5.4 Mössbauer spectrum for the product targeted for $Na_{2+2x}Fe_{2-x}(SO_4)_3$ ($x = 0.25$) at room temperature. The experimental data (black circles), and caluclated profile (black line) are shown. (Inset) The contineous quadrupole splitting (QS) distribution of *alluaudite* phase, indicating a wide range of coordination environments.

Table 5.1 Fitting parameters for Mössbauer spectrum of the sample targeted for x = 0.25. Normalized χ^2 was 1.25 for the refinement.

		IS / mm s^{-1}	Magnetic field /T	QS / mm s^{-1}	Fraction / %	Line width / mm s^{-1}
$Na_{2.56}Fe_{1.72}(SO_4)_3$	Fe^{II}	1.2797 (6)	-	2.200 (3)	96.3 (1)	0.25
Fe_3O_4	Fe^{II+III}	0.67	46	0	2.5 (2)	0.204 (3)
	Fe^{III}	0.26	49	-0.02	1.2 (1)	0.120 (4)

To determine the structure of off-stoichiometric alluaudite $Na_{2+2x}Fe_{2-x}(SO_4)_3$, the high-resolution X-ray diffraction (HR-XRD) is conducted. Figure 5.5 shows the Rietveld refinement results for HR-XRD. Amount of Fe_3O_4 impurity phase (1.2 wt%, corresponding to 3.8 atom%) is consistent with the result of the Mössbauer spectroscopy. The *C2/c* structure model is employed for the refinement, based on the absence of forbidden reflections from the *C*-centered lattice ($h + l = 2n + 1$). Note that this is a typical space group of the alluaudite-type compounds.[26] The crystallographic information obtained from HR-XRD is summarized in Tables 5.2-5.3.

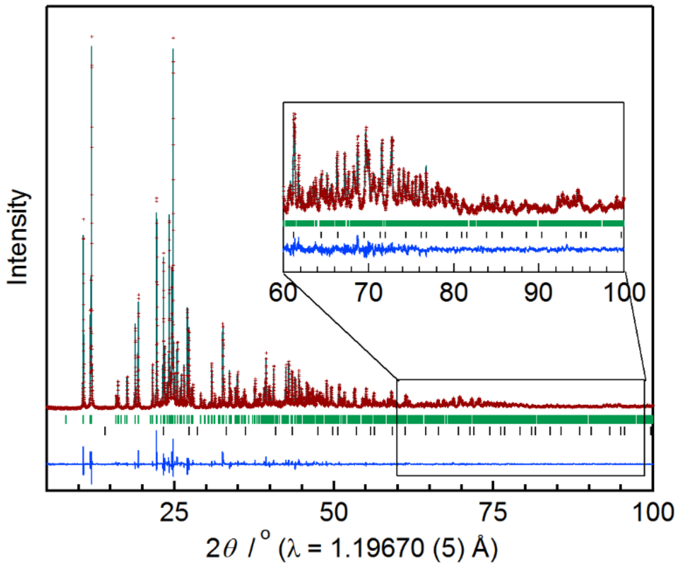

Figure 5.5 Rietveld refinement patterns of high resolution X-ray diffraction data for the product targeted for $Na_{2+2x}Fe_{2-x}(SO_4)_3$ (x = 0.25). The experimental data (red crosses), calculated profile (green line), and their difference (blue line) are indicated.

Table 5.2 Crystal data and refinement indices for X-ray diffraction data.

Chemical formula	$Na_{2.56}Fe_{1.72}(SO_4)_3$
M_r	443.1
Crystal system, space group	Monoclinic, *C*2/*c*
Temperature (K)	300
a, *b*, *c* (Å)	12.65860 (8), 12.77591 (8), 6.51614 (4)
α, β, γ (°)	90, 115.5419 (3), 90
V (Å^3)	950.834 (10)
Z	4
Radiation type	Synchrotron radiation from bending magnet, λ = 1.19670 (5) Å
R_{wp}	0.05711
R_p	0.05173
GoF	1.59
R_{Bragg}	0.0235

Table 5.3 Fractional atomic coordinates and isotropic displacement parameters for X-ray diffraction.

	x	*y*	*z*	B_{iso} / Å^2	Occ. (<1)
Fe1	0.26923 (6)	0.34192 (5)	0.35286 (12)	1.166 (16)	Fe: 0.86, Na: 0.129 (3)
S1	0	0.27645 (12)	1/4	1.18 (3)	
O11	0.0851 (2)	0.3461 (2)	0.2163 (4)	1.72 (6)	
O12	0.0523 (2)	0.20898 (19)	0.4515 (4)	1.50 (6)	
S2	0.23815 (10)	0.10296 (8)	0.1312 (2)	1.40 (2)	
O21	0.23453 (18)	0.16857 (19)	0.3162 (4)	0.94 (5)	
O22	0.1783 (2)	0.0029 (2)	0.1223 (4)	2.17 (6)	
O23	0.3603 (2)	0.0865 (2)	0.1693 (5)	2.62 (7)	
O24	0.3263 (2)	0.3416 (2)	0.0856 (4)	1.73 (5)	
Na1	0	0.73268 (18)	1/4	2.20 (6)	
Na2	0	1/2	0	5.887 (15)	0.738 (5)
Na3	0	0.0137 (4)	1/4	3.91 (16)	0.565 (7)

5.5 Structural considerations

The crystal structure is essentially isostructural with the general alluaudite $AA'BM_2(XO_4)_3$[26]. Na occupies three crystallographic positions (Na1, Na2 and Na3), whereas Fe occupies one crystallographic position under the *C2/c* symmetry (Fig. 5.6 (i)). According to the general formula, this compound corresponds to *A* = Na2, *A'* = Na3, *B* = Na1, *M* = Fe and *X* = S.

Na1 is coordinated by six O atoms with an average bond-length of 2.45 Å, and is close to the sum of the ionic radii (2.53 Å).[27] Na2 and Na3 occupy two special positions 4*b* and 4*e*. Na2 is coordinated by six O atoms with average bond length of 2.49 Å. The bond-valence-sum (BVS) values for Na1 and Na2 (1.06 and 1.00) agree well with the expected value of 1.0 for Na^+,[28] thus these two sites are favorable for Na^+ occupation. In contrast, the average Na3–O distance is 2.74 Å, which is much longer than the sum of the ionic radii. Furthermore, the BVS value for Na3 (0.69) deviates significantly from the formal valence of unity. Therefore, the Na3 site should have shallow site potential for Na+ occupation, leading to high mobility of Na+ ion. Indeed, our previous DFT calculation implies that the Na3 site is more unstable than the Na1 and Na2 sites by 0.5–0.7 eV and connected each other with a small migration barriers.[17]

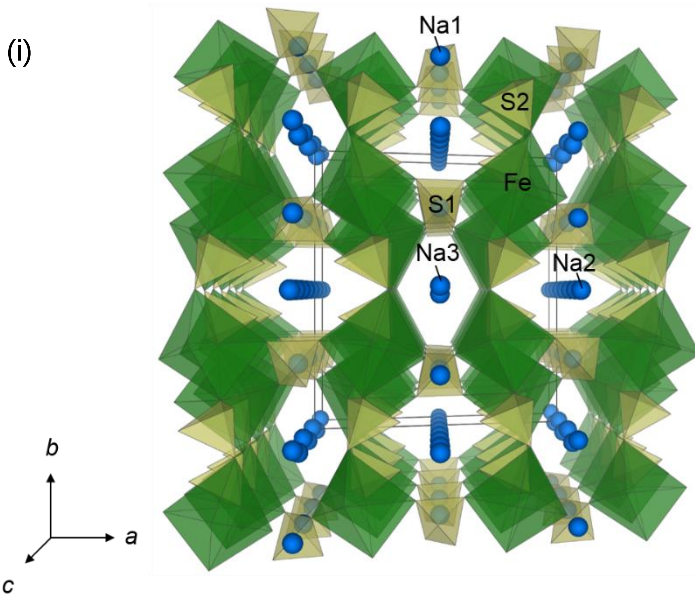

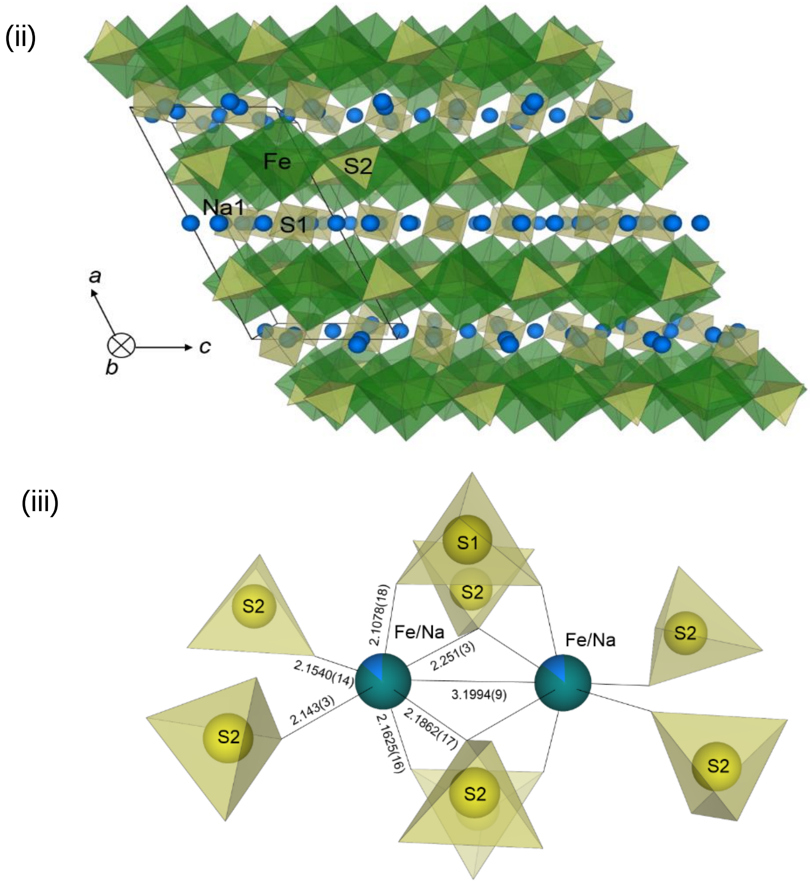

Figure 5.6 (i) Crystal structure of allaudite $Na_{2+2x}Fe_{2-x}(SO_4)_3$ projected along *c*-axis. (ii) $Na[Fe_2(SO_4)_3]_2$ layer marked in a). (iii) Local environment for Fe sites in allaudite $Na_{2+2x}Fe_{2-x}(SO_4)_3$.

Six O-atoms of the SO_4^{2-} anions coordinate to Fe in a distorted octahedral geometry. The FeO_6 octahedron shares an equatorial edge with the crystallographically equivalent FeO_6 octahedron to form an Fe_2O_{10} dimer, the center of which is a centrosymmmetric special position 4*d*, as shown in Fig. 5.6 (iii). Two axial apexes of the Fe_2O_{10} dimer are bridged by the SO_4^{2-} anions, which may cause a short Fe–Fe distance of 3.199 Å. Let us recall $Li_2FeP_2O_7$ has edge-sharing Fe_2O_9 dimers but without polyanion bridge, which gives the longer Fe–Fe distance of 3.23 Å.[29] Therefore, the short Fe–Fe distance in the alluaudite phase may be ascribed to the axial bridge by the small SO_4 tetrahedron (Fig. 5.6(iii)). It should be emphasized that BVS for the Fe site is 1.87, which is smaller than the expected value (2.0) of the formal Fe valence state.[28] Since the small BVS value generally results from the long bond-length, possible explanation for the small BVS value is that a small fraction of Fe^{2+} (ionic radius of 0.79 Å) is partially replaced by Na^+ (ionic radius of 1.16 Å). The substituted Na/Fe site is hereinafter referred to as Na4 site.

To confirm the defect and Na distribution in the structure, occupancies for Na2, Na3, and Na4 sites were refined. Linear constraints were used to satisfy the proposed composition of $Na_{2.56}Fe_{1.72}(SO_4)_3$ based on the result of Mössbauer spectroscopy: $g_{\mathrm{Fe}} = 0.86$, $g_{\mathrm{Na4}} \leq 0.14$, $g_{\mathrm{Na1}} + g_{\mathrm{Na2}} + g_{\mathrm{Na3}} + 2g_{\mathrm{Na4}} = 6 - 4g_{\mathrm{Fe}}$, where g_{i} is the occupancy of the site i, and g_{Na1} was fixed to unity because the vacancy of the Na1 site was negligible in any refinements. The HR-XRD refinement showed a large amount of the vacancy exists at the Na2 and Na3 sites ($g_{\mathrm{Na2}} = 0.738$ (5) and $g_{\mathrm{Na3}} = 0.565$ (7)). Furthermore, the occupancy of Na4 site was 0.129 (3), supporting Na^+ substitution for Fe^{2+} as discussed above. The wide QS distribution in Mössbauer spectrum is mainly due to many possible configurations of these defects in Na2, Na3 sites and Na4 sites around Fe.

Scheme 5.2 summarizes the possible compositional, structural and electrochemical flexibilities of the alluaudite sodium iron sulfate. The Fe/Na ratio can be varied by replacement of Fe with Na as well as the vacancy formation at the Na sites, leading to variation of the theoretical capacity. The stoichiometric sample has not been obtained under the present synthetic conditions, and hence the capacity is limited to ca. 100 mAh g^{-1} at this stage. However, the stoichiometric alluaudite $Na_2Fe_2(SO_4)_3$ is expected to deliver the theoretical capacity of 120 mAh g^{-1}, whereby Na-ion batteries becomes competitive with or better than the state-of-the-art Li-ion batteries.

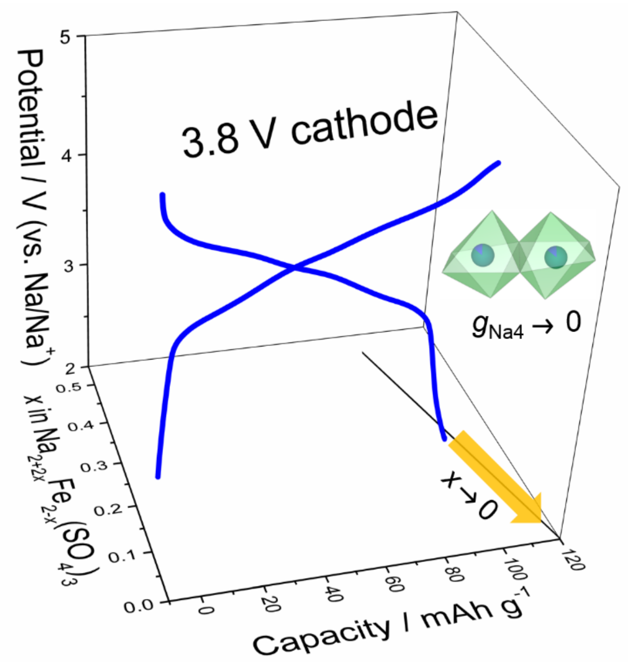

Scheme 5.2 Illustration of possible compositional, structural and electrochemical flexibilities of the allaudite $Na_{2+2x}Fe_{2-x}(SO_4)_3$. The charge-discharge curves are quoted from ref. 16. When the Fe/Na ratio approaches unity, the theoretical capacity increases as indicated with the arrow.

5.6 Conclusion

The author has clarified the overall phase equilibrium in the Na_2SO_4-$FeSO_4$ binary system, and the existence of off-stoichiometric alluaudite $Na_{2+2x}Fe_{2-x}(SO_4)_3$. The systematic XRD experiments for the samples targeted for $0 \leq x \leq 0.4$ showed that the compositional range of the solid solution $Na_{2+2x}Fe_{2-x}(SO_4)_3$ is off-stoichiometric ($x = 0.25$–0.3) under the present synthetic conditions. The composition of the product targeted for $x = 0.25$ was analyzed to be ca. $Na_{2.56}Fe_{1.72}(SO_4)_3$ with partial Na^+ substitution for Fe site. The present work represents the possible compositional, structural and electrochemical flexibilities of alluaudite $Na_{2+2x}Fe_{2-x}(SO_4)_3$, which may open up new opportunities for further improvement/development of the alluaudite–type sodium iron sulfates as Na-ion electrode materials.

References

(1) Slater, M. D.; Kim, D.; Lee, E.; Johnson, C. S. *Adv. Funct. Mater.* **2013**, *23*, 947–958.

(2) Kubota, K.; Yabuuchi, N.; Yoshida, H.; Dahbi, M.; Komaba, S. *MRS Bull.* **2014**, *39*, 416–422.

(3) Yabuuchi, N.; Kajiyama, M.; Iwatate, J.; Nishikawa, H.; Hitomi, S.; Okuyama, R.; Usui, R.; Yamada, Y.; Komaba, S. *Nat. Mater.* **2012**, *11*, 512–517.

(4) Wang, X.; Liu, G.; Iwao, T.; Okubo, M.; Yamada, A. *J. Phys. Chem. C* **2014**, *118*, 2970–2976.

(5) Wang, X.; Tamaru, M.; Okubo, M.; Yamada, A. *J. Phys. Chem. C* **2013**, *117*, 15545–15551.

(6) Ellis, B. L.; Makahnouk, W. R. M.; Makimura, Y.; Toghill, K.; Nazar, L. F. *Nat. Mater.* **2007**, *6*, 749–753.

(7) Barpanda, P.; Ye, T.; Nishimura, S.; Chung, S.-C.; Yamada, Y.; Okubo, M.; Zhou, H.; Yamada, A. *Electrochem. commun.* **2012**, *24*, 116–119.

(8) Yamada, A. *MRS Bull.* **2014**, *39*, 423–428.

(9) Rousse, G.; Tarascon, J. M. *Chem. Mater.* **2014**, *26*, 394–406.

(10) Recham, N.; Chotard, J.-N.; Dupont, L.; Delacourt, C.; Walker, W.; Armand, M.; Tarascon, J.-M. *Nat. Mater.* **2010**, *9*, 68–74.

(11) Barpanda, P.; Ati, M.; Melot, B. C.; Rousse, G.; Chotard, J.-N.; Doublet, M.-L.; Sougrati, M. T.; Corr, S. A.; Jumas, J.-C.; Tarascon, J.-M. *Nat. Mater.* **2011**, *10*, 772–779.

(12) Reynaud, M.; Ati, M.; Melot, B. C.; Sougrati, M. T.; Rousse, G.; Chotard, J.-N.; Tarascon, J.-M. *Electrochem. commun.* **2012**, *21*, 77–80.

(13) Lander, L.; Reynaud, M.; Rousse, G.; Sougrati, M. T.; Laberty-Robert, C.; Messinger, R. J.; Deschamps, M.; Tarascon, J.-M. *Chem. Mater.* **2014**, *26*, 4178–4189.

(14) Ati, M.; Dupont, L.; Recham, N.; Chotard, J.-N. J. N.; Walker, W. T.; Davoisne, C.; Barpanda, P.; Sarou-Kanian, V.; Armand, M.; Tarascon, J.-M. J. M. *Chem. Mater.* **2010**, *22*, 4062–4068.

(15) Barpanda, P.; Chotard, J.-N.; Recham, N.; Delacourt, C.; Ati, M.; Dupont, L.; Armand, M.; Tarascon, J.-M. *Inorg. Chem.* **2010**, *49*, 7401–7413.

(16) Barpanda, P.; Oyama, G.; Ling, C. D.; Yamada, A. *Chem. Mater.* **2014**, *26*, 1297–1299.

(17) Barpanda, P.; Oyama, G.; Nishimura, S.; Chung, S.-C.; Yamada, A. *Nat. Commun.* **2014**, *5*, 4358.

(18) Keester, K. L.; Eysel, W. *Acta Crystallogr. Sect. B Struct. Crystallogr. Cryst. Chem.* **1977**, *33*, 306–307.

(19) Reynaud, M.; Rousse, G.; Abakumov, A. M.; Sougrati, M. T.; Van Tendeloo, G.; Chotard, J.-N.; Tarascon, J.-M. *J. Mater. Chem. A* **2014**, *2*, 2671–2680.

(20) Trad, K.; Carlier, D.; Croguennec, L.; Wattiaux, A.; Ben Amara, M.; Delmas, C. *Chem. Mater.* **2010**, *22*, 5554–5562.

(21) Gray.J., L. *Mössbauer Spectroscopy Applied to Inorganic Chemistry*; Plenum Press: New York, 1984.

(22) Trad, K.; Carlier, D.; Croguennec, L.; Wattiaux, A.; Ben Amara, M.; Delmas, C. *Inorg. Chem.* **2010**, *49*, 10378–10389.

(23) Kim, J.; Kim, H.; Park, I.; Park, Y.-U.; Yoo, J.-K.; Park, K.-Y.; Lee, S.; Kang, K. *Energy Environ. Sci.* **2013**, *6*, 830.

(24) Kim, J.; Kim, H.; Park, K.-Y.; Park, Y.-U.; Lee, S.; Kwon, H.-S.; Yoo, H.-I.; Kang, K. *J. Mater. Chem. A* **2014**, *2*, 8632.

(25) Essehli, R.; Belharouak, I.; BEN YAHIA, H.; Maher, K.; Abouimrane, A.; Orayech, B.; Calder, S.; Zhou, X.; Zhou, Z.; Sun, Y.-K. *Dalt. Trans.* **2015**.

(26) Fisher, D. J. *Am. Mineral.* **1955**, *40*, 1100–1109.

(27) Shannon, R. *Phys. Chem. Miner.* **1979**, *4*, 139–148.

(28) Brown, I. D. *Chem. Rev.* **2009**, *109*, 6858–6919.

(29) Nishimura, S.; Nakamura, M.; Natsui, R.; Yamada, A. *J. Am. Chem. Soc.* **2010**, *132*, 13596–13597.

6. Sodium Intercalation Mechanism of 3.8 V Class Alluaudite Sodium Iron Sulfate

6.1 Introduction

Advanced grid energy storage systems are in great demand to level off-peak and/or intermittent electricity from renewable energy sources (e.g. wind, solar, and tidal). Electrochemical energy storage systems are a promising solution, which can achieve coexistence of high-efficiency, long cycle life, and rapid charge to reduce sudden power spikes without sacrificing cost or safety. As one of the most pragmatic candidates, rechargeable Na-ion batteries have re-attracted attention owing to the high natural abundance and even geographical distribution of sodium. To maximize the advantage of Na, positive electrode compounds for Na-ion batteries should consist of Fe or Mn as earth-abundant 3*d* transition metals as redox centers. In this regard, an increasing number of studies have been focused on layered oxides (e.g. O3-type Na_xMO_2[1,2], P2-type Na_xMO_2[3], where M = Fe and/or Mn) and phosphates (e.g. olivine-Na_xFePO_4[4,5], Na_2FePO_4F[6], $Na_2FeP_2O_7$[7], $Na_4Fe_3(PO_4)_2(P_2O_7)$[8,9]). Replacing PO_4 units with more electronegative SO_4 units is an effective way to increase the redox potential, which is often referred to as an "inductive effect"[10]. Many Li intercalation sulfates generate a high potential (typically 3.5-3.9 V versus Li^+/Li), e.g. tavorite- and triplite-$LiFeSO_4F$[11,12], KTP-type $KFeSO_4F$[13], layered $LiFeSO_4OH$[14], marinate, orthorhombic $Li_2Fe(SO_4)_2$[15,16], and aramanite-derived $Fe_2O(SO_4)_2$[17].

Contrary to a step forward of the sulfates in Li systems, Na intercalation compounds reported to date show limited (e.g. $Na_2Fe(SO_4)_2{\cdot}4H_2O$[18], kröhnkite $Na_2Fe(SO_4)_2{\cdot}2H_2O$[19]) or no (e.g. maxwellite-$NaFeSO_4F$[20], $NaFeSO_4F{\cdot}2H_2O$[21]) electrochemical activity. Recently, an alluaudite sodium iron sulfate with superior rate capability and the highest potential ever reported at 3.8 V (versus Na^+/Na) among any Fe^{3+}/Fe^{2+} redox couples was reported. [22]

The crystal structure of the compound is essentially isostructural to alluaudite, the common alkaline manganese iron phosphate mineral.[23] As typical for alluaudite compounds, the sodium iron sulfate adopts the monoclinic lattice with *C2/c* symmetry with the general formula of $AA'BM_2(XO_4)_3$, where A = Na2, A' = Na3, B = Na1, M = Fe and X = S (Fig. 6.1 (i)).[23,24] An edge-sharing pair of equivalent FeO_6 octahedra form a Fe_2O_{10} dimer, which is bridged by corner-sharing SO_4 tetrahedra. This unique local Fe coordination results in short Fe-Fe interatomic distances of approximately 3.2 Å, which are likely to contribute to the extremely high redox potential.[24,25] Moreover, inherent deviation from stoichiometry ($x \approx 0.28$ in $Na_{2+2x}Fe_{2-x}(SO_4)_3$, i.e. $Na_{2.56}Fe_{1.72}(SO_4)_3$) and Na replacing Fe on the Fe1 site (referred to Na/Fe1 site) were reported.[24] Thereby, Na occupies four distinctive sites (Na1, Na2, Na3, and Na/Fe1) on Wyckoff positions, 4*e*, 4*b*, 4*e*, and 8*f*, respectively. Two of the four Na sites, Na2 and Na3 are located within one-dimensional open channels as illustrated in Fig. 6.1(i).

To the best of our knowledge, the detailed mechanism of structural changes during electrochemical cycling has not been investigated yet. A clear understanding of electrochemical processes is essential for further performance improvements for this important class of cathode materials. In this work, structural changes during the charging and discharging processes were examined, and the underlying mechanism of the irreversible profile during the first charging process as well as the stabilized behavior in the subsequent cycles were revealed.

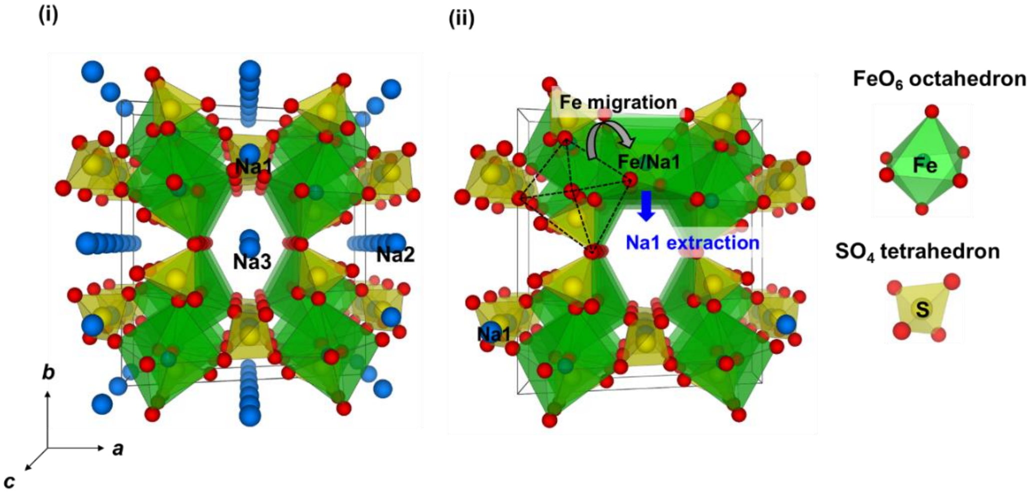

Figure 6.1 (i) The crystal structure of pristine alluaudite sodium iron sulfate. Sodium and

oxygen ions are illustrated in blue and red. Green octahedra and yellow tetrahedra represent FeO_6 and SO_4 units, respectively. Two distinctive Na diffusion channels of Na2 and Na3 are visible along the *c* axis. (ii) The crystal structure of the alluaudite $Na_{2.56-y}Fe_{1.72}(SO_4)_3$ after an irreversible Fe migration from Fe1 to Na1 site upon the first charging process.

6.2 Experimental methods

The alluaudite $Na_{2.56}Fe_{1.72}(SO_4)_3$ powder was synthesized according to the previously reported procedure.[24] All of the galvanostatic charge-discharge measurements for *ex situ* X-ray diffraction (XRD), X-ray near edge absorption (XANES), and Mössbauer spectroscopy measurements were performed with 2032-type coin cells (Hohsen Corp.). Positive electrodes consisted of 80 wt.-% alluaudite phase, 13 wt.-% carbon black (Ketjen Black, Lion Corp., ECP) and 7 wt.-% polytetrafluoro-ethylene (PTFE) binder (provided from an industrial partner). Na metal (Kanto Chemical), glass fiber film (ADVANTEC), and 1 M $NaClO_4$ dissolved in propylene carbonate (PC) (Tomiyama Pure Chemical Industries, Ltd.) with 2 vol.-% of fluoroethylene carbonate (FEC)[26] (Kishida Chemical) were used for negative electrodes, separators, and electrolytes, respectively. After the measurements, the cells were disassembled in an Ar filled glove box (dew point < –70 ^{o}C, Miwa Co. Ltd.), and the positive electrode tapes were washed with dimethyl carbonate (DMC) (Kishida Chemical) three times and dried under vacuum to remove impurities. The electrode tapes were packed into Ar filled borosilicate glass tubes (0.3 mm in diameter) for *ex situ* XRD analyses.

Ex situ synchrotron XRD measurements were carried out at KEK PF BL-8B beam line, Tsukuba, Japan. The wavelength was calibrated to be 1.03289 (5) Å. Rietveld refinements and subsequent Fourier difference syntheses were calculated with TOPAS-Academic Ver. 5.0.

Solid-state Magic Angle Spinning (MAS) ^{23}Na NMR measurements were conducted on 700 MHz, 300 MHz, and 200 MHz Bruker Avance I and III spectrometers with respective ^{23}Na Larmor frequencies of 185.2, 79.4, and 52.9 MHz. Hahn-echo pulse sequences with 90^{o} pulse lengths of 1.0 μs were applied. The spectra were acquired with Bruker 1.3 and 2.5 mm MAS probeheads at 60 kHz and 30 kHz spinning frequency, respectively. ^{23}Na shifts were referenced to a 0.1 M NaCl solution in D_2O.[27] All spectra were analyzed using DMFIT.[28] The investigated samples were prepared by chemical oxidation (desodiation) and reduction (sodiation). Chemical oxidation was done using $NOBF_4$ (95%, Aldrich) in acetonitrile under continuous Ar bubbling. The subsequent chemical reduction was conducted using $NaBH_4$ in tetrahydrofuran (THF, Wako Chemical) under Ar atmosphere. After the chemical oxidation/reduction, the powders were washed by pure acetonitrile/THF three times and dried under vacuum at room temperature. The compounds were packed into 1.3 and 2.5 mm ZrO_2 rotors (Bruker) inside an Ar filled glove box with O_2 and H_2O levels < 0.1 ppm to avoid exposure to air and moisture. Oxidation/reduction states of the Fe ions were determined with Mössbauer spectroscopy measurements and resulted in nominal compositions of $Na_{2.56-y}Fe_{1.72}(SO_4)_3$ with $y = 0.0$, 0.41, 0.62, 0.85, and 1.5 for the desodiated samples and $y = 1.0$, 0.67, 0.45, and 0.1 for the sodiated samples (cf. Fig. 6.6).

XANES spectra were measured at KEK PF BL-7C. Fe K-edge absorption spectra (7080-7180 eV) were collected at room temperature. The X-ray intensity was monitored by ionization chambers in transmission mode using a Si (111) double-crystal monochromator for energy selection. The obtained data were processed with Athena.[29] The electrochemically charged and discharged electrode tapes (about 10 mm in diameter) were applied for the measurements. They were washed with dimethyl carbonate (DMC, Kishida Chemical) and sealed in Ar filled polyethylene films (Asahi Kasei Pax).

Mössbauer spectra were measured for electrochemically charged and discharged samples with a Topologic System Inc. spectrometer equipped with a ^{57}Co/Rh γ–ray source. The velocity was calibrated by using α-Fe. The electrode tapes were processed in the same way as described for the XANES measurements. The obtained spectra were fitted by Moss Winn (version 3.0) software.

6.3 Electrochemical charging/discharging behaviors

Charging/discharging curves and the corresponding differential galvanostatic profiles (d*Q*/d*V*) of alluaudite sodium iron sulfate are shown in Fig. 6.2 (i). The d*Q*/d*V* curve (Inset of Fig. 6.2 (i)) shows two distinctive redox peaks at 3.67 and 4.06 V upon the first charging process, whereas there are three broad peaks at 3.37, 3.76, and 3.99 V upon the first discharging process as previously reported.[22] Common features are reported in the case of Li_2FeSiO_4[30,31], and $Li_2FeP_2O_7$[32,33], where Li-Fe site exchange takes place during the first charging process.

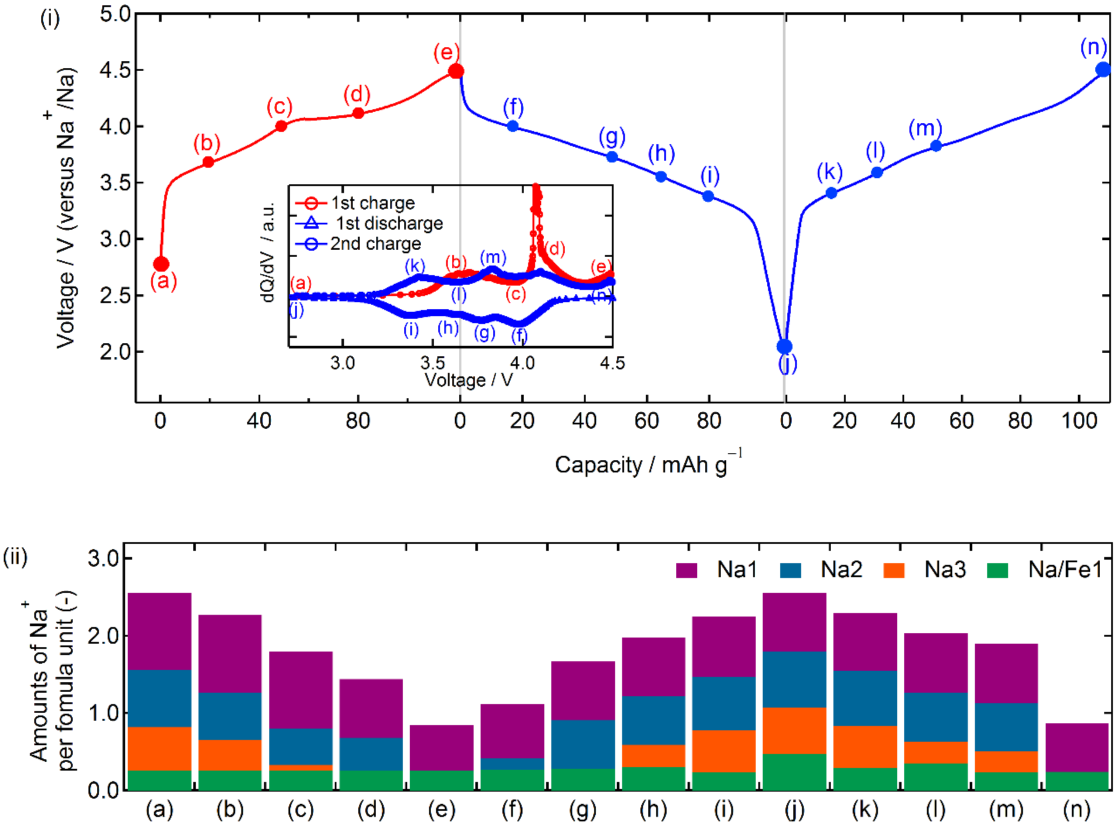

Figure 6.2 (i) Charge/discharge profiles of $Na_{2.56-y}Fe_{1.72}(SO_4)_3$ at different states of charge, (a)-(n). The initial charge and the following full discharge-charge cycle are shown as red and blue curves, respectively. (Inset) The corresponding d*Q*/d*V* profiles, which show an irreversible first charge process and subsequent processes. Note that the reversible feature retained upon further cycling.[22] (ii) Amounts of Na per formula unit in $Na_{2.56-y}Fe_{1.72}(SO_4)_3$ during the electrochemical processes, (a)-(n). Purple, light blue, orange, and green bars

indicate Na^+ amounts at Na1, Na2, Na3, and Na/Fe1 sites, respectively.

6.4 Structural changes

To probe the structural changes during electrochemical cycling, *ex situ* XRD measurements and Rietveld refinements were performed for $Na_{2.56-y}Fe_{1.72}(SO_4)_3$ electrodes (Fig. 6.3 (i)). Refined lattice parameters a, b, c, β and the unit cell volume V are illustrated in Fig. 6.3 (ii) (refined patterns and refinement indices are shown in Fig. 6.4 and Table 6.1). For the refinements, the total amounts of Na were fixed to be those calculated by the electrochemical reaction and atomic displacement parameters of the pristine electrode at (a) in Fig. 6.2 (i) were used.

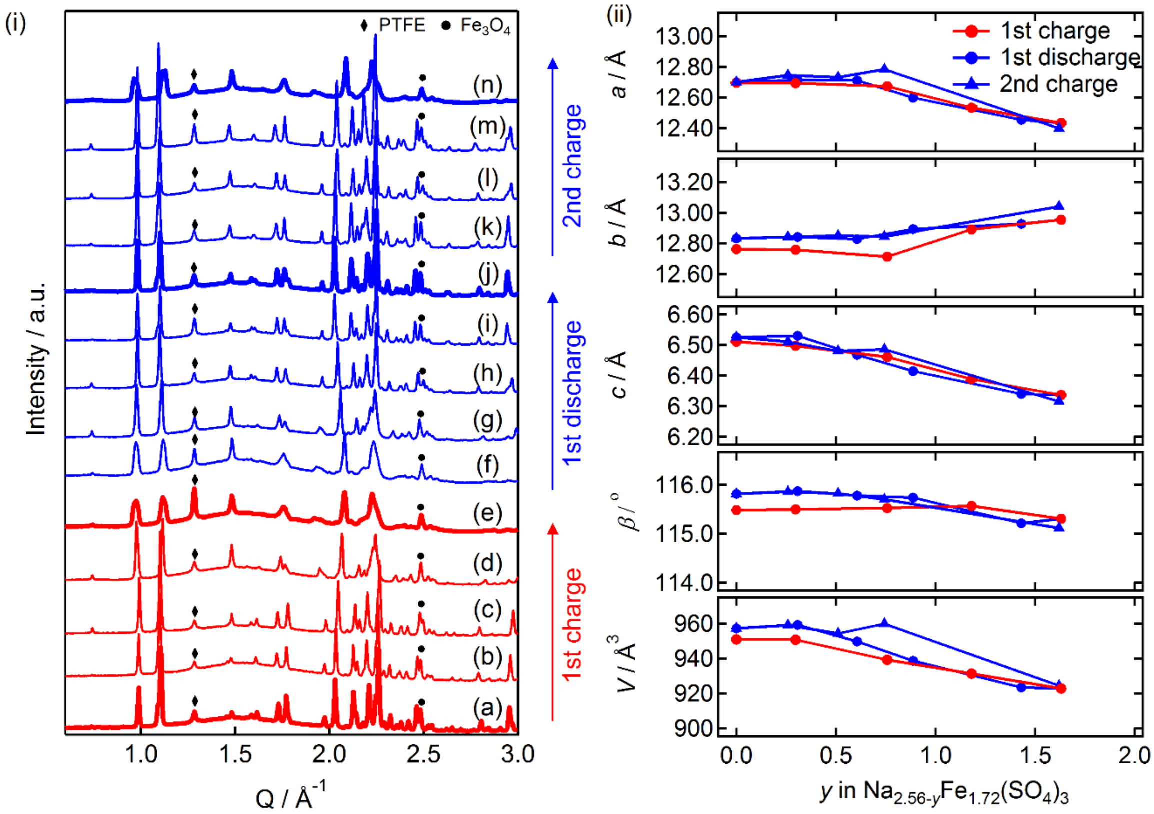

Figure 6.3 (i) *Ex situ* XRD patterns of $Na_{2.56-y}Fe_{1.72}(SO_4)_3$ at the different states of charge (a)-(n). The black rhombus and circle mark diffraction peaks of the PTFE binder and an Fe_3O_4 impurity phases, respectively. (ii) The variation of lattice parameters *a*, *b*, *c*, *β* and the unit cell volume *V* with monoclinic *C2/c* symmetry during the first two electrochemical cycles. 1st charging, discharging, 2nd charging processes are shown in red circles, blue circles

and blue triangles with solid lines, respectively.

Upon the first charging process, the lattice parameters *a* and *c* continuously decrease, whereas the lattice parameter *b* increases after the sharp peak in the d*Q*/d*V* plot (d) at 4.06 V. The unit cell volume *V* shows gradual shrinkage (ΔV = –2.6 % at the fully charged state), which can be classified as a single-phase reaction with a small volume change in spite of a Na extraction with a relatively large ionic radius of 1.02 Å.

Upon the first discharging process, the lattice parameters *a* and *c* undergo reversible expansion, but *b* undergoes a partially reversible shrinkage. These come to a slightly larger absolute volume change (ΔV = +3.5 %) than the first charging process. Upon the second charging process, the lattice parameters and the unit cell volume show reversible change (ΔV = –3.4 %). Overall, the irreversible change was only detected in the first charging process, and the reaction was totally reversible in the following cycles, which is consistent with a good cycle performance. The observed small volume change might be due to the three-dimensional open framework of the alluaudite structure and its off-stoichiometric composition.

Even after the whole oxidation to Fe^{3+} of the non-stoichiometric $Na_{2.56}Fe_{1.72}(SO_4)_{3,}$ 0.84 mol of Na ions remain in the 3D framework, which may function as binding pillars. Indeed, first principle calculations predict that the volume change of the non-stoichiometric $Na_{2+2x}Fe_{2-x}(SO_4)_3$ phase (ΔV = ca. 5 % for x = 0.25) is smaller than that of stoichiometric phase (ΔV = ca. 8 % for x = 0) based on the full utilization of Fe^{3+}/Fe^{2+} redox reaction.

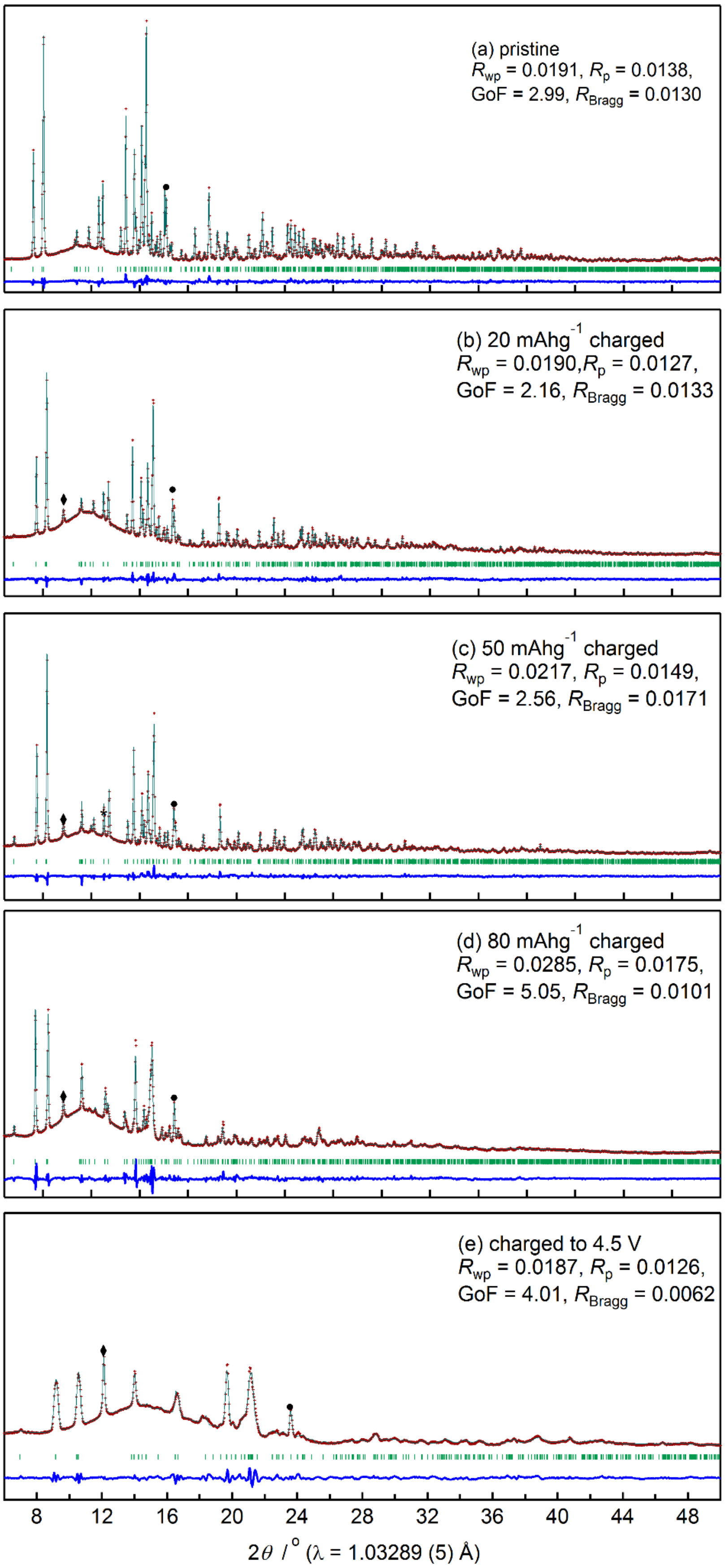
(a) pristine
R_{wp} = 0.0191, R_p = 0.0138,
GoF = 2.99, R_{Bragg} = 0.0130
(b) 20 mAhg^{-1} charged
R_{wp} = 0.0190,R_p = 0.0127,
GoF = 2.16, R_{Bragg} = 0.0133
(c) 50 mAhg^{-1} charged
R_{wp} = 0.0217, R_p = 0.0149,
GoF = 2.56, R_{Bragg} = 0.0171
(d) 80 mAhg^{-1} charged
R_{wp} = 0.0285, R_p = 0.0175,
GoF = 5.05, R_{Bragg} = 0.0101
(e) charged to 4.5 V
R_{wp} = 0.0187, R_p = 0.0126,
GoF = 4.01, R_{Bragg} = 0.0062
8
12
16
20
24
28
32
36
40
44
48
2θ / $^{\circ}$ (λ = 1.03289 (5) Å)

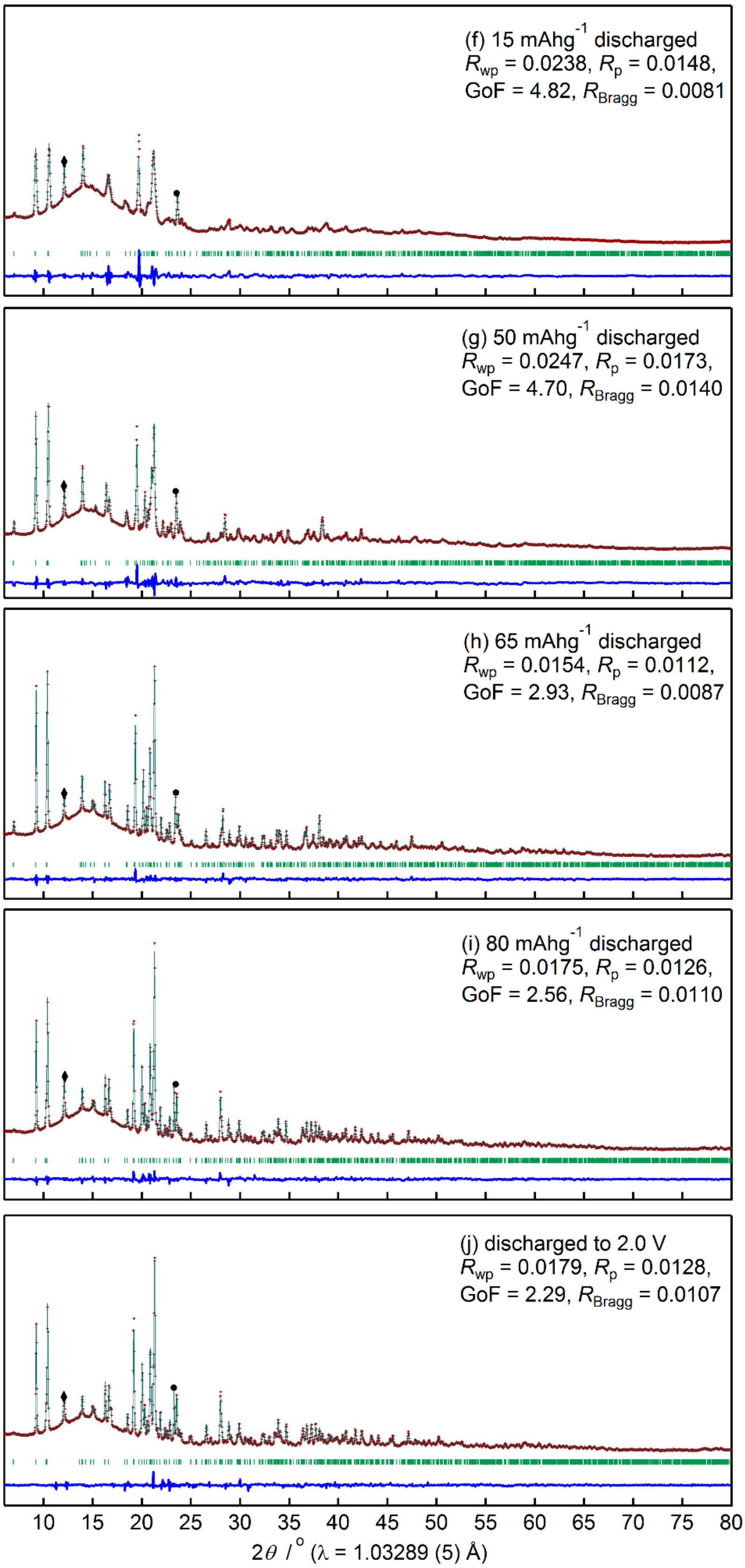
(f) 15 mAhg^{-1} discharged
R_{wp} = 0.0238, R_p = 0.0148,
GoF = 4.82, R_{Bragg} = 0.0081
(g) 50 mAhg^{-1} discharged
R_{wp} = 0.0247, R_p = 0.0173,
GoF = 4.70, R_{Bragg} = 0.0140
(h) 65 mAhg^{-1} discharged
R_{wp} = 0.0154, R_p = 0.0112,
GoF = 2.93, R_{Bragg} = 0.0087
(i) 80 mAhg^{-1} discharged
R_{wp} = 0.0175, R_p = 0.0126,
GoF = 2.56, R_{Bragg} = 0.0110
(j) discharged to 2.0 V
R_{wp} = 0.0179, R_p = 0.0128,
GoF = 2.29, R_{Bragg} = 0.0107
10 15 20 25 30 35 40 45 50 55 60 65 70 75 80
2θ / ° (λ = 1.03289 (5) Å)

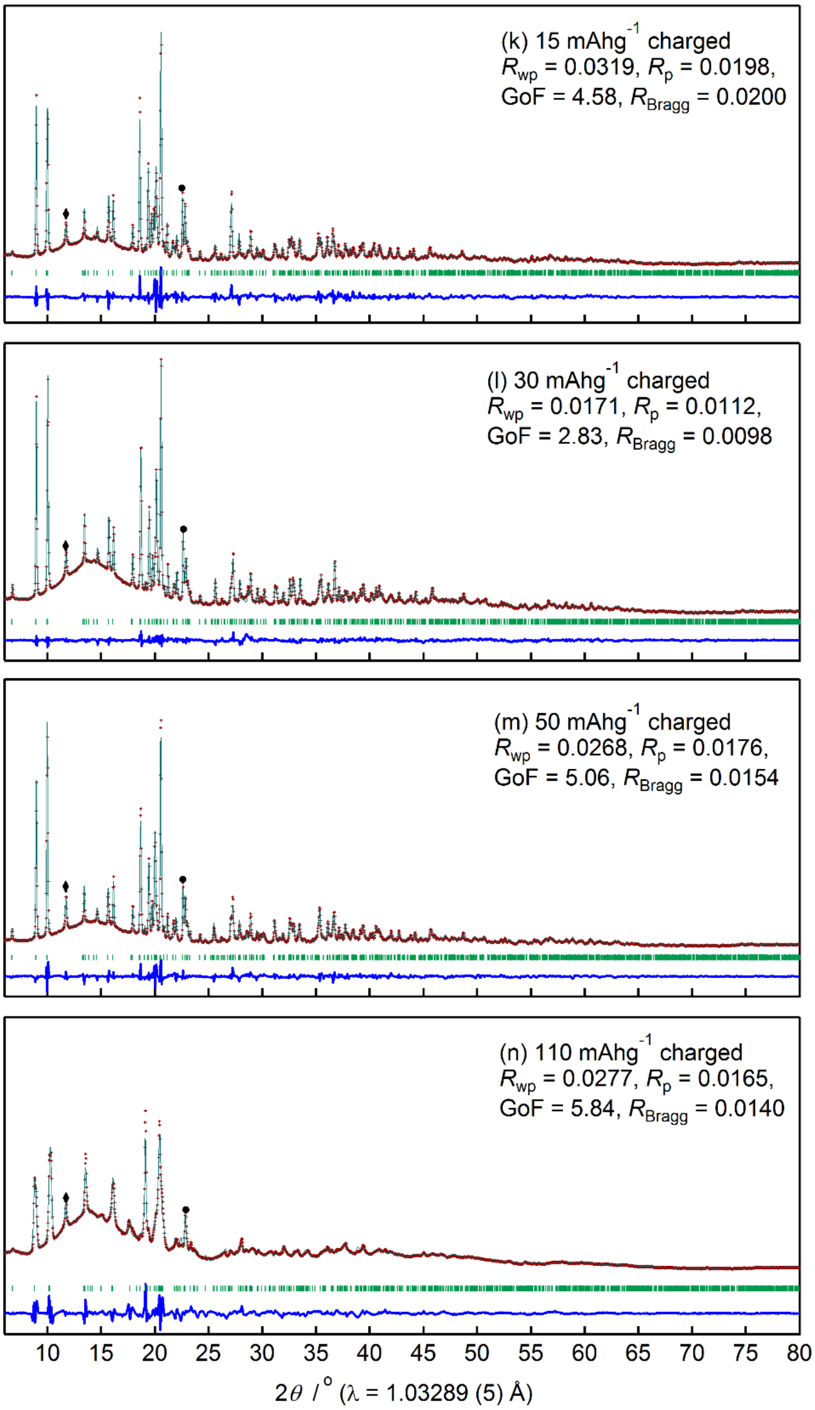

Figure 6.4 **Rietveld refinement patterns of *ex situ* XRD data for electrochemically charged/discharged $Na_{2+2x}Fe_{2-x}(SO_4)_3$ samples (a)-(n). Experimental data is shown with red crosses and calculated profiles in blue-green lines with the respective peak positions in green as well as the difference of fit and experiment in blue. The black rhombus and circle marks represent the Bragg peak positions of the PTFE binder and Fe_3O_4 impurity phases,**

respectively.

Table 6.1 Refined structural parameters for *ex situ* XRD patterns of electrochemically charged and discharged samples. Fractional coordination *x*, *y*, *z* are indicated with the single deviation value in parenthesis. Isotropic displacement parameters B_{iso} (Å^2) were fixed to those of the pristine phase (a) to avoid correlation problems with the occupancies. Full occupancies (Occ. = 1) are not shown.

(a) pristine

	x	*y*	*z*	B_{iso} / Å^2	Occ. (<1)
Fe1	0.26959 (17)	0.34318 (16)	0.3537 (4)	0.59 (3)	Fe: 0.86, Na: 0.13
S1	0	0.2756 (3)	1/4	0.66 (6)	
O11	0.0831 (3)	0.3465 (6)	0.2151 (11)	1.43 (10)	
O12	0.0541 (6)	0.2099 (6)	0.4550 (14)	0.58 (9)	
S2	0.2391 (3)	0.1030 (2)	0.1314 (6)	0.96 (4)	
O21	0.2313 (5)	0.1706 (5)	0.3098 (10)	0.55 (9)	
O22	0.1783 (2)	0.0029 (2)	0.1223 (4)	2.27 (11)	
O23	0.3611 (6)	0.0848 (5)	0.1678 (9)	1.59 (11)	
O24	0.3273 (5)	0.3409 (5)	0.0856 (10)	0.96 (9)	
Na1	0	0.7347 (5)	1/4	1.57 (6)	
Na2	0	1/2	0	5.75 (18)	0.739 (5)
Na3	0	0.0163 (11)	1/4	4.98 (2)	0.561 (4)

(b) 20 mAhg^{-1} charged

	x	*y*	*z*	B_{iso} / Å^2	Occ. (<1)
Fe1	0.26904 (17)	0.34383 (16)	0.3534 (4)	0.59	Fe: 0.86, Na: 0.13
S1	0	0.2755 (4)	1/4	0.66	
O11	0.0820 (5)	0.3421 (6)	0.2134 (11)	1.43	
O12	0.0558 (5)	0.2092 (5)	0.4565 (13)	0.58	
S2	0.2436 (3)	0.1034 (3)	0.1352 (7)	0.96	
O21	0.2315 (5)	0.1706 (5)	0.3073 (11)	0.55	
O22	0.1819 (5)	0.0032 (7)	0.1284 (11)	2.27	
O23	0.3631 (7)	0.0880 (6)	0.1744 (12)	1.59	
O24	0.3248 (6)	0.3429 (5)	0.0762 (12)	0.96	

Na1	0	0.7354 (6)	1/4	1.57	
Na2	0	1/2	0	5.75	0.615 (8)
Na3	0	0.0122 (2)	1/4	4.98	0.395 (8)

(c) 50 mAhg^{-1} charged

	x	*y*	*z*	B_{iso} / Å^2	Occ. (<1)
Fe1	0.27046 (19)	0.34528 (18)	0.3577 (4)	0.59	Fe: 0.86, Na: 0.13
S1	0	0.2790 (4)	1/4	0.66	
O11	0.0798 (6)	0.3418 (6)	0.2061 (12)	1.43	
O12	0.0799 (6)	0.2115 (6)	0.4578 (15)	0.58	
S2	0.2475 (3)	0.1046 (3)	0.1399 (8)	0.96	
O21	0.2343 (6)	0.1689 (6)	0.3055 (12)	0.55	
O22	0.1898 (5)	0.001 (8)	0.13102 (13)	2.27	
O23	0.3726 (7)	0.0911 (6)	0.1910 (13)	1.59	
O24	0.3208 (6)	0.3395 (6)	0.0755 (13)	0.96	
Na1	0	0.7428 (7)	1/4	1.57	
Na2	0	1/2	0	5.75	0.470 (7)
Na3	0	0.007 (12)	1/4	4.98	0.072 (7)

(d) 80 mAhg^{-1} charged

	x	*y*	*z*	B_{iso} / Å^2	Occ. (<1)
Fe1	0.2735 (4)	0.3498 (5)	0.3677 (13)	0.59	Fe: 0.738 (4), Na: 0.13
S1	0	0.2819 (9)	1/4	0.66	
O11	0.0826 (14)	0.3561 (13)	0.2385 (3)	1.43	
O12	0.0446 (15)	0.2152 (14)	0.4503 (3)	0.58	
S2	0.2421 (8)	0.1059 (6)	0.1287 (16)	0.96	
O21	0.2234 (14)	0.1776 (10)	0.3092 (3)	0.55	
O22	0.1907 (6)	0.0029 (8)	0.1317 (13)	2.27	
O23	0.3576 (16)	0.1040 (14)	0.159 (3)	1.59	
O24	0.3410 (15)	0.3324 (12)	0.088 (3)	0.96	
Na1	0	0.7329 (10)	1/4	1.57	Fe: 0.243 (9), Na: 0.757 (9)
Na2	0	1/2	0	5.75	0.425 (9)
Na3	0	0.0163	1/4	4.98	0

(e) 120 mAhg^{-1} charged

	x	*y*	*z*	B_{iso} / Å^2	Occ. (<1)
Fe1	0.2881 (9)	0.3496 (6)	0.390 (2)	0.59	Fe: 0.654 (8), Na: 0.13
S1	0	0.3018 (14)	1/4	0.66	

O11	0.1192 (3)	0.343 (2)	0.252 (5)	1.43	
O12	0.032 (2)	0.2152 (14)	0.388 (4)	0.58	
S2	0.2324 (10)	0.0993 (9)	0.136 (2)	0.96	
O21	0.212 (2)	0.1906 (15)	0.286 (4)	0.55	
O22	0.1361 (16)	0.0275 (17)	0.113 (3)	2.27	
O23	0.332 (2)	0.064 (2)	0.159 (3)	1.59	
O24	0.3421 (19)	0.3295 (14)	0.094 (4)	0.96	
Na1	0	0.7058 (9)	1/4	1.57	Fe: 0.411 (15), Na: 0.589 (15)
Na2	0	1/2	0	5.75	0
Na3	0	0.0163	1/4	4.98	0

(f) 15 mAhg^{-1} discharged

	x	*y*	*z*	B_{iso} / Å^2	Occ. (<1)
Fe1	0.2772 (9)	0.3524 (6)	0.3739 (2)	0.59	Fe: 0.711 (7), Na: 0.133 (17)
S1	0	0.2898 (13)	1/4	0.66	
O11	0.099 (3)	0.354 (2)	0.236 (5)	1.43	
O12	0.043 (2)	0.226 (2)	0.433 (5)	0.58	
S2	0.2450 (11)	0.0965 (10)	0.135 (2)	0.96	
O21	0.211 (2)	0.1871 (18)	0.284 (4)	0.55	
O22	0.162 (16)	0.027 (2)	0.116 (3)	2.27	
O23	0.359 (2)	0.090 (2)	0.162 (3)	1.59	
O24	0.338 (3)	0.7326 (16)	0.090 (5)	0.96	
Na1	0	0.7201 (14)	1/4	1.57	Fe: 0.2977 (15), Na: 0.7023 (14)
Na2	0	1/2	0	5.75	0.152(14)
Na3	0	0.0163	1/4	4.98	0

(g) 50 mAhg^{-1} discharged

	x	*y*	*z*	B_{iso} / Å^2	Occ. (<1)
Fe1	0.2723 (4)	0.3492 (4)	0.3659 (9)	0.59	Fe: 0.740 (3), Na: 0.142 (8)
S1	0	0.2786 (7)	1/4	0.66	
O11	0.083 (3)	0.354 (2)	0.236 (5)	1.43	
O12	0.0485 (11)	0.2115 (9)	0.461 (3)	0.58	
S2	0.2436 (6)	0.1046 (5)	0.1346 (13)	0.96	
O21	0.2257 (11)	0.1782 (9)	0.3120 (3)	0.55	
O22	0.1901 (9)	0.0049 (13)	0.1370 (19)	2.27	
O23	0.3611 (12)	0.1026 (11)	0.168 (2)	1.59	

O24	0.3357 (11)	0.3338 (9)	0.084 (2)	0.96	
Na1	0	0.7387 (8)	1/4	1.57	Fe: 0.240 (6), Na: 0.760 (6)
Na2	0	1/2	0	5.75	0.625 (6)
Na3	0	0.0163	1/4	4.98	0

(h) 65 mAhg^{-1} discharged

	x	*y*	*z*	B_{iso} / Å^2	Occ. (<1)
Fe1	0.2707 (2)	0.34609 (19)	0.3609 (5)	0.59	Fe: 0.7468 (19), Na: 0.153 (6)
S1	0	0.2817 (4)	1/4	0.66	
O11	0.0870 (6)	0.3530 (6)	0.2250 (12)	1.43	
O12	0.0870 (6)	0.2164 (6)	0.4502 (13)	0.58	
S2	0.2433 (4)	0.1081 (3)	0.1342 (8)	0.96	
O21	0.2293 (11)	0.1717 (5)	0.3091 (13)	0.55	
O22	0.1891 (5)	0.0084 (8)	0.1299 (12)	2.27	
O23	0.3629 (7)	0.0975 (6)	0.1678 (11)	1.59	
O24	0.3316 (6)	0.3378 (6)	0.0824 (13)	0.96	
Na1	0	0.7371 (4)	1/4	1.57	Fe: 0.226 (4), Na: 0.774 (4)
Na2	0	1/2	0	5.75	0.632 (6)
Na3	0	0.0308 (2)	1/4	4.98	0.289 (7)

(i) 80 mAhg^{-1} discharged

	x	*y*	*z*	B_{iso} / Å^2	Occ. (<1)
Fe1	0.2698 (2)	0.34319 (18)	0.3580 (4)	0.59	Fe: 0.747 (2), Na: 0.120 (5)
S1	0	0.2814 (4)	1/4	0.66	
O11	0.0862 (6)	0.3507 (6)	0.2270 (11)	1.43	
O12	0.0526 (6)	0.2157 (5)	0.4551 (13)	0.58	
S2	0.2391 (3)	0.1070 (3)	0.1303 (7)	0.96	
O21	0.2301 (6)	0.1687 (5)	0.3120 (11)	0.55	
O22	0.1776 (5)	0.0053 (7)	0.1159 (11)	2.27	
O23	0.3602 (7)	0.0902 (5)	0.1665 (12)	1.59	
O24	0.3313 (6)	0.3413 (5)	0.0904 (11)	0.96	
Na1	0	0.7344 (4)	1/4	1.57	Fe: 0.223 (3), Na: 0.777 (3)
Na2	0	1/2	0	5.75	0.693 (8)
Na3	0	0.0224 (13)	1/4	4.98	0.539 (12)

(j) 110 mAhg^{-1} discharged

	x	*y*	*z*	B_{iso} / Å^2	Occ. (<1)
Fe1	0.27028 (19)	0.34355 (17)	0.3583 (4)	0.59	Fe: 0.742 (2), Na: 0.237 (6)

S1	0	0.2812 (3)	1/4	0.66	
O11	0.0855 (6)	0.3484 (6)	0.2254 (10)	1.43	
O12	0.0535 (6)	0.2154 (5)	0.4570 (13)	0.58	
S2	0.2405 (3)	0.1063 (2)	0.1300 (7)	0.96	
O21	0.2288 (5)	0.1702 (5)	0.3108 (11)	0.55	
O22	0.1779 (5)	0.0062 (7)	0.1174 (11)	2.27	
O23	0.3612 (7)	0.0888 (5)	0.1680 (12)	1.59	
O24	0.3204 (6)	0.3426 (5)	0.0744 (11)	0.96	
Na1	0	0.7348 (4)	1/4	1.57	Fe: 0.236 (5), Na: 0.764 (5)
Na2	0	1/2	0	5.75	0.721 (8)
Na3	0	0.0235 (12)	1/4	4.98	0.601 (15)

(k) 15 mAhg^{-1} charged

	x	*y*	*z*	B_{iso} / Å^2	Occ. (<1)
Fe1	0.2707 (3)	0.3453 (3)	0.3661 (6)	0.59	Fe: 0.734 (6), Na: 0.147 (7)
S1	0	0.2790 (6)	1/4	0.66	
O11	0.0863 (9)	0.3437 (9)	0.2372 (16)	1.43	
O12	0.0616 (9)	0.2161 (8)	0.4423 (18)	0.58	
S2	0.2490 (5)	0.1057 (4)	0.1429 (9)	0.96	
O21	0.2216 (9)	0.1700 (7)	0.3135 (17)	0.55	
O22	0.1692 (7)	0.0138 (10)	0.1183 (16)	2.27	
O23	0.3646 (10)	0.0911 (8)	0.1740 (18)	1.59	
O24	0.3343 (9)	0.3379 (8)	0.0797 (18)	0.96	
Na1	0	0.7336 (6)	1/4	1.57	Fe: 0.252 (7), Na: 0.748 (7)
Na2	0	1/2	0	5.75	0.719 (11)
Na3	0	0.0485 (18)	1/4	4.98	0.540 (16)

(l) 30 mAg^{-1} charged

	x	*y*	*z*	B_{iso} / Å^2	Occ. (<1)
Fe1	0.2710 (2)	0.34586 (17)	0.3598 (4)	0.59	Fe: 0.746 (2), Na: 0.177 (4)
S1	0	0.2821 (4)	1/4	0.66	
O11	0.0851 (6)	0.3513 (6)	0.2270 (11)	1.43	
O12	0.0462 (6)	0.2179 (6)	0.4498 (13)	0.58	
S2	0.2415 (3)	0.1095 (2)	0.1321 (7)	0.96	
O21	0.2291 (6)	0.1724 (5)	0.3085 (12)	0.55	
O22	0.1881 (5)	0.0089 (7)	0.1327 (11)	2.27	
O23	0.3597 (6)	0.0974 (5)	0.1635 (11)	1.59	
O24	0.3319 (6)	0.3392 (5)	0.0831 (11)	0.96	

Na1	0	0.7389 (4)	1/4	1.57	Fe: 0.226 (4), Na: 0.774 (4)
Na2	0	1/2	0	5.75	0.635 (7)
Na3	0	0.0197 (3)	1/4	4.98	0.280 (11)

(m) 50 mAg^{-1} charged

	x	*y*	*z*	B_{iso} / Å^2	Occ. (<1)
Fe1	0.2703 (4)	0.3437 (2)	0.3600 (6)	0.59	Fe: 0.742 (3), Na: 0.118 (6)
S1	0	0.2784 (4)	1/4	0.66	
O11	0.0909 (7)	0.3479 (7)	0.2269 (14)	1.43	
O12	0.0552 (7)	0.2103 (6)	0.4493 (15)	0.58	
S2	0.2459 (4)	0.1085 (3)	0.1359 (9)	0.96	
O21	0.2303 (7)	0.1691 (6)	0.3076 (14)	0.55	
O22	0.1864 (6)	0.0108 (9)	0.1306 (13)	2.27	
O23	0.3595 (6)	0.0933 (7)	0.1696 (14)	1.59	
O24	0.3319 (7)	0.3392 (6)	0.0831 (15)	0.96	
Na1	0	0.7381 (5)	1/4	1.57	Fe: 0.237 (5), Na: 0.763 (5)
Na2	0	1/2	0	5.75	0.632 (8)
Na3	0	0.0235 (4)	1/4	4.98	0.269 (8)

(n) 110 mAg^{-1} charged

	x	*y*	*z*	B_{iso} / Å^2	Occ. (<1)
Fe1	0.2837 (9)	0.3438 (7)	0.379 (2)	0.59	Fe: 0.674 (7), Na: 0.144 (7)
S1	0	0.2902 (14)	1/4	0.66	
O11	0.117 (3)	0.3397 (19)	0.275 (5)	1.43	
O12	0.036 (2)	0.2080 (18)	0.425 (5)	0.58	
S2	0.2350 (13)	0.0946 (10)	0.130 (2)	0.96	
O21	0.219 (3)	0.1660 (18)	0.304 (4)	0.55	
O22	0.1564 (19)	0.0094 (19)	0.108 (4)	2.27	
O23	0.343 (2)	0.071 (2)	0.163 (4)	1.59	
O24	0.339 (2)	0.3349 (18)	0.086 (4)	0.96	
Na1	0	0.7057 (10)	1/4	1.57	Fe: 0.372 (15), Na: 0.628 (15)
Na2	0	1/2	0	5.75	0
Na3	0	0.0163	1/4	4.98	0

6.5 Sodium intercalation mechanism

Figure 6.2 (ii) indicates the amount of Na at each crystallographic site during charge-discharge processes determined by Rietveld refinements for the *ex situ* XRD patterns. At the initial stage of the charging process (a)-(c), corresponding to the broad peak observed at 3.67 V in the dQ/dV plot, the occupancy of Na3 site (g_{Na3}) abruptly decreases from 0.561(5) to 0.072(7). This indicates Na extraction primarily occurred at the Na3 site, which is consistent with the computational results for the shallowest potential of the Na3 site, involving a small migration energy between Na3-Na3 sites (ca. 300 meV).[22,34] At this stage, g_{Na2} decreased by only about 0.12, while g_{Na1}, and $g_{\mathrm{Na/Fe1}}$ remained constant, where $g_{\mathrm{Na2},}$ $g_{\mathrm{Na1},}$ and $g_{\mathrm{Na/Fe1}}$ are the occupancies of Na ions in Na2, Na1 site and Fe1 site, respectively.

At the further charging up to (d) after the irreversible sharp peak observed in the $\mathrm{d}Q/\mathrm{d}V$ plot, a drastic change was observed in the diffraction pattern, which cannot be explained by the occupancy change in mobile Na2 and Na3 sites only.[22,34] The calculated Fourier difference map (Fig. 6.5 (i)) indicates positive residual electron density on the Na1 site, suggesting that the site is replaced by heavier ions. Thereby, a structural model with Fe migrated into Na1 site (referred to Fe/Na1 site) is adopted, as illustrated in Fig. 6.1 (ii). For the refinement, the total number of Fe was fixed to unity with linear constraint: $2g_{\mathrm{Fe1}} + g_{\mathrm{Fe/Na1}} = 1.72$. The refinement based on the proposed model leads to an improvement of reliable indices (e.g. R-weighted pattern (R_{wp}) reduced from 0.0315 to 0.0285) as well as the disappearance of unreasonable residual electron density on Na1 site (Fig. 6.5(ii)), where about 16 % of Fe at Fe1 site ($\Delta g_{\mathrm{Fe1}} = 0.21$) migrated to Na1 site. Based on the redefined structure for (d), the bond-valence-sum (BVS) value calculated for Na1 site (expected to be 1.0 for Na^{+})[35] increased from 1.06 to 1.49, supporting the Fe migration further. The mechanism of the migration might be similar to those of $\mathrm{Li}_{2-y}\mathrm{FeP}_2\mathrm{O}_7$ and $\mathrm{Na}_{4-y}\mathrm{Fe}_3(\mathrm{PO}_4)_2(\mathrm{P}_2\mathrm{O}_7)$[9], where the driving force is the strong Fe^{3+}–Fe^{3+} Coulombic repulsion within the edge-sharing dimer.[33] In fact, the alluaudite sodium iron sulfate has a shorter Fe–Fe length (3.199 Å) in the edge-sharing Fe_2O_{10} dimer than that in $Li_2FeP_2O_7$ (3.23 Å). Therefore, at the sharp peak in the d*Q*/d*V* curve at 4.06 V in the first charging process, Na extraction from Na1 site starts to induce Fe^{3+} migration from the pristine Fe1(8*f*) site into the vacant Na1 (4*e*) site.

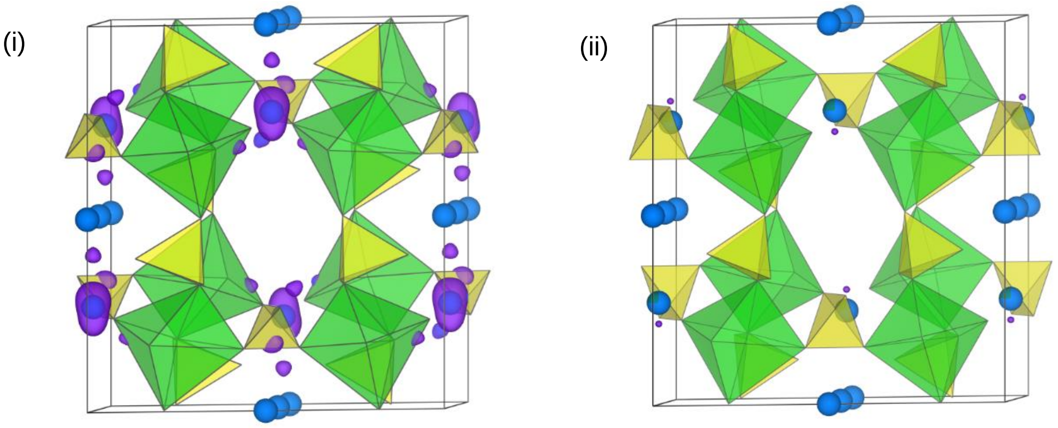

Figure 6.5 Calculated Fourier difference maps of alluaudite sodium iron sulfate (i) before and (ii) after considering the irreversible Fe migration at stage (d) (cf. Fig. 6.3) upon the charging process. Blue spheres, green octahedra, yellow tetrahedra, and purple isosurfaces (0.1 $Å^{-3}$) show Na, FeO_6, SO_4, and residual electron density, respectively.

At the fully charged state (e), g_{Na2} decreased to 0, and the diffraction peaks were broadened (Fig. 6.3), presumably due to a long range disordering induced by micro strains, as the peak width showed reversible change upon subsequent charge/discharge processes. Therefore, throughout the whole initial charging process, Na extraction occurs primarily at Na3 followed by Na1 and Na2 site.

In the following discharging process of (e)-(g), an increase for g_{Na2} was dominant, while negligible changes occurred for g_{Na1}, g_{Na3} and $g_{Na/Fe1}$. Therefore, the cathodic peak at 3.99 V in the d*Q*/d*V* plot is attributed to Na insertion into the Na2 site.

In the deeper discharge at (g)-(h), g_{Na3} started to increase, showing that the potential peak at 3.76 V is mainly due to Na insertion into Na3 site. At the last step of the discharging process (h)-(j), $g_{\mathrm{Na/Fe1}}$ increased, while those of the other Na sites remained constant. Thus, the peak at 3.37 V in the dQ/dV plot corresponds to Na insertion into the vacant Fe1 site which had been occupied by Fe ions before the migration of Fe^{3+} into Na1 site in the first charging process. Throughout the whole discharging process, negligible occupancy change for Fe at Fe1 site (Δg_{Fe1} = ca. 0.09) was observed. Thus, Fe migration occurs in the first charging process but not in the subsequent cycles, which provide reversible features as a battery cathode. Upon the subsequent (second) charging process (j)-(n), the electrode reaction is reversible tracing the preceding discharging step. Sequential Na extraction occurs in the order of Na/Fe1 followed by Na3 and Na2 sites, pairing the three broad peaks in the dQ/dV plot.

^{23}Na MAS NMR signal of pristine $Na_{2.56-y}Fe_{1.72}(SO_4)_3$ (y = 0.0) result in an 350 ppm broad signal centered at 0 ppm (Fig. 6.6). NMR experiments at different magnetic fields and MAS spinning frequencies prove any further signals to be rotational sidebands (RSB). There is no dominant contribution of quadrupole coupling (QC), chemical shift anisotropy (CSA) and/or paramagnetic broadening on the ^{23}Na NMR signal line shape (Fig. 6.6i)[36,37]. The increase of the number of RSB as well as the significant changes of the NMR signal from low to high magnetic fields (4.7, 7.0 and 16.4 T) at a constant MAS frequency of 60 kHz are in agreement with a linear scaling of paramagnetic broadening effects with the field strength (Fig. 6.6i)[36]. Paramagnetic broadening is expected for $Na_{2.56}Fe_{1.72}(SO_4)_3$ due to the unpaired electrons of Fe^{2+} in the $t_{2g}^{4}\ e_{g}^{2}$ (high-spin) configuration.

A deconvolution and signal line shape fitting results in two ^{23}Na NMR resonances at -40 and 70 ppm (Fig. 6.6, Table 6.2). This small shift is unexpected for the paramagnetic material and due to a large inductive effect by the sulfate groups[36–39]. The covalent S-O bonds create ionic M-O (M = Na, Fe) bonds causing a reduced hyperfine interaction between the O(2p) and Fe(3d) orbitals and a respective smaller shift as usually found for paramagnetic materials[37]. Referring the DFT calculation results by Pigliapochi *et al*, $Na_{2.50}Fe_{1.75}(SO_4)_3$ gives shift values (Hyb20/Hyb35) of –80/–97, 385/263, 138/65, and 177/91 ppm for Na1, Na2, Na3, and Na/Fe1.[40] Based on these shift regimes and the total shift trend of Na1<Na3<Na/Fe1<Na2, the two ^{23}Na NMR signals for pristine $Na_{2.56-y}Fe_{1.72}(SO_4)_3$ (y = 0.0) are attributed to Na1+Na3 (green line) and Na2+Na/Fe1 (purple line), respectively (Fig. 6.6, Table 6.2).

A comparison of the site occupancies derived by Rietveld refinements of the XRD data with the fractions of the two Na environments detected by NMR reads 6.2/4.0 (=1.6) vs. 0.6/0.4 (=1.5). The calculation is based on Na1(4*e*)+Na3(4*e*) and Na2(4*b*)+Na/Fe1(8*f*), resulting in 4×(1.0+0.56) / (4×0.74+8×0.13) vs. the fractions of the ^{23}Na NMR signals for pristine $Na_{2.56}Fe_{1.72}(SO_4)_3$ (Table 6.2). The good agreement of the ratios derived by independent methods supports the analysis of the local atomic environments and their assignments.

The ^{23}Na NMR signals of $Na_{2.56-y}Fe_{1.72}(SO_4)_3$ show significant changes of the line shape and an overall positive shift during desodiation that is reversed during sodiation (Fig. 6.7). This is generally due to an increase of Fe^{3+} with more unpaired electrons in the $t_{2g}^3\ e_g^2$ configuration during desodiation causing stronger electron spin density transfer to the Na and a positive shift and vice versa during the sodiation. Note that the ^{23}Na NMR line shape of the fully sodiated sample (y = 0.1) slightly differs from that of the pristine (y = 0) sample (Fig. 6.7). An intensity decrease of the negatively shifted signal might be due to the irreversible desodiation from Na1 site at the first charging process, which is consistent with the results of Rietveld refinements.

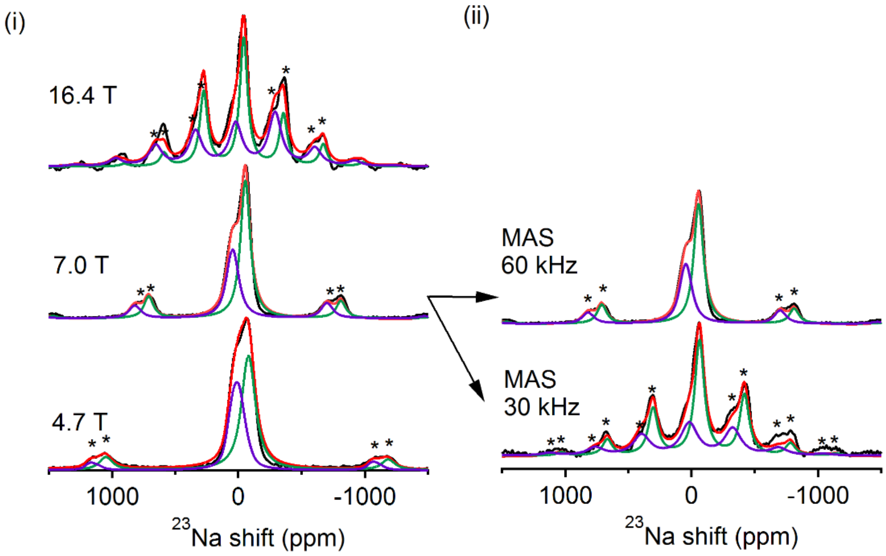

Figure 6.6 ^{23}**Na MAS NMR spectra of pristine** $Na_{2.56-y}Fe_{1.72}(SO_4)_3$ **(**$y = 0$**) at (i) 60 kHz MAS frequency in magnetic fields of 4.7, 7.0, and 16.4 T and (ii) MAS frequencies of 30 and 60 kHz at 7.0 T. Experimental data are depicted in black, fitted data in red (significantly overlapped with experimental) and the respective signal contributions in purple and green. Rotational sidebands are marked by asterisks.**

Table 6.2 Experimentally derived ^{23}**Na NMR coupling parameters (quadrupolar coupling constant** C_Q**, asymmetry parameter for quadrupolar coupling** η_Q**, chemical shift anisotropy CSA, asymmetry parameter of chemical shielding** η_{CSA}**, and total shift** δ_{tot}**) for the Na environments in** $Na_{2.56}Fe_{1.72}(SO_4)_3$**. The environments are denoted as A (green) and B (purple) and assigned to the respective crystallographic sites.**

Environment	**Assignment**	C_Q **(MHz)**	η_Q	**CSA (ppm)**	η_{CSA}	δ_{tot} **(ppm)**	**Fraction (%)**
A (green)	Na1+Na3	1.9(1)	0.7(1)	-900(200)	0.7(1)	-40(5)	59.5(7)
B (purple)	Na2+Na/Fe1	3.0(1)	0.5(1)	1100(100)	0.7(1)	70(10)	40.5(7)

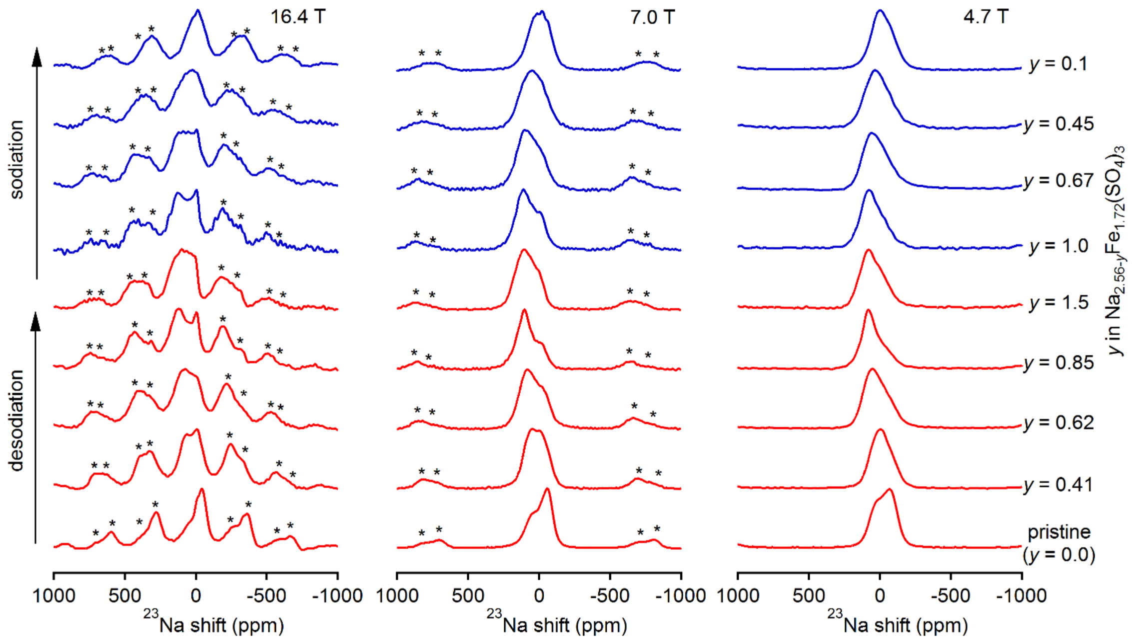

Figure 6.7 ^{23}Na MAS NMR spectra at 60 kHz spinning speed of alluaudite sodium iron sulfate measured in magnetic fields of 16.4 T (left), 7.0 T (middle), and 4.7 T (right). Rotational sidebands are labelled by asterisks. Red and blue spectra represent the first desodiation and sodiation processes, respectively. The nominal compositions of the investigated samples are given by the varying y value in $Na_{2.56-y}Fe_{1.72}(SO_4)_3$ on the right side of the figure.

6.6 Reversible valence state changes of iron

To investigate the oxidation state of Fe, *ex situ* XANES measurements are performed during the first charging and discharging processes. As illustrated in Fig. 6.8, the K-edge of Fe shifted toward higher energy upon charging with the corresponding features for the pre-edge region (inset of Fig. 6.8), which is consistent with the increase of Fe oxidation state. No isosbestic points were observed, supporting the single-phase reaction mechanism. Upon discharging, both the main-, and pre-edges are reversible back toward lower energy. The spectrum at the fully discharged state is very similar to that of the pristine phase, suggesting the Fe^{3+}/Fe^{2+} redox reaction is reversible. Reversible changes for Fe oxidation states are further confirmed by Mössbauer spectroscopy (Fig.

6.9). The fitting parameters of Mössbauer spectra are shown in Table 6.3. The line profiles are extensively broad due to various possible Na arrangements around Fe sites, so distributions of quadrupole splittings (QS) are postulated. A spectrum after the first electrochemical cycle (Fig 6.9 (iii)) shows all of the Fe species are attributed to be Fe^{2+}. These suggest the irreversible capacity (~16 $mAhg^{-1}$) is mainly due to the decomposition of the electrolyte and the irreversible Fe migration at the initial charging process gives the minimal effect for reversibility of the Fe^{3+}/Fe^{2+} redox reaction.

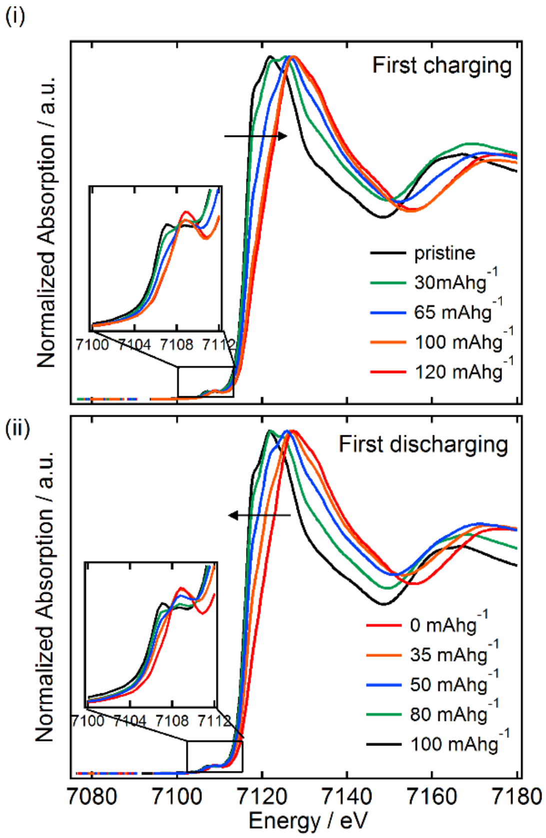

Figure 6.8 ***Ex situ*** **Fe** ***K*****-edge XANES spectra of $Na_{2.56-y}Fe_{1.72}(SO_4)_3$ at different states of charge. (i) and (ii) indicate spectra acquired upon the initial charging and discharging processes, respectively. The insets are enlargements of the pre-edge regions.**

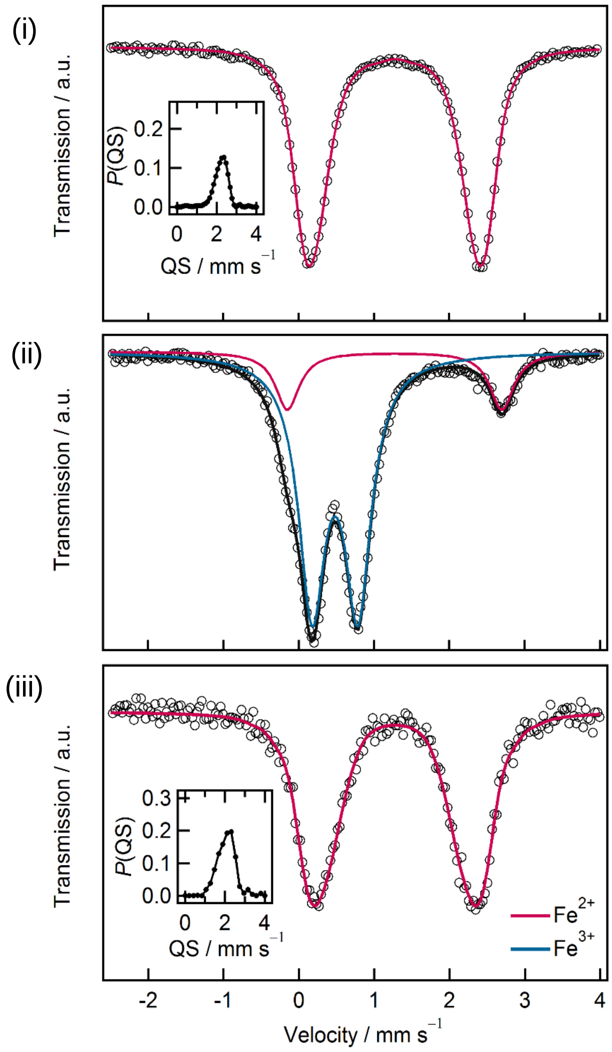

Figure 6.9 Mössbauer spectra of alluaudite sodium iron sulfate at the different states of charge; (i) pristine, (ii) fully charged (to 4.5 V), and (iii) fully discharged (to 2.0 V) states at the first cycle, respectively. The Insets are populations of quadrupole splittings *P*(QS), which show the wide variety of iron local environments.

Table 6.3 Isomer shift (IS), quadrupole splitting (QS) parameter, Fe^{2+}/Fe^{3+} fractions as well as line widths (LW) based on the refinements of the Mössbauer spectra of $Na_{2.56-y}Fe_{1.72}(SO_4)_3$ at different states of charge that are given in the first column of the table. The single standard deviation is given in parenthesis. Normalized chi-square (χ^2) for each fitting were 1.25, 1.39, and 1.02 for the pristine, the charged, and the discharged states, respectively.

		IS (mm s^{-1})	QS (mm s^{-1})	Fraction (%)	LW (mm s^{-1})
Pristine	Fe^{2+}	1.2796 (6)	2.200 (3)	100	0.25
Charged to 4.5 V	Fe^{2+}	1.274 (4)	2.848 (8)	17.3 (4)	0.427 (1)
	Fe^{3+}	0.4821 (10)	0.6099 (16)	82.7 (3)	0.429 (3)
Discharged to 2.0 V	Fe^{2+}	1.2783 (-)	2.06 (3)	100	0.25

6.7 Conclusion

The present chapter reveals the electrochemical reaction mechanism of alluaudite sodium iron sulfate as a Na-ion battery cathode via a combined approach with diffraction and spectroscopic measurements. The single-phase (solid-solution) reaction occurs involving an irreversible rearrangement reaction upon the first charging process. The origin of the irreversibility is the Na extraction from Na1 site accompanied by Fe migration from Fe1 to Na1 site; this mechanism is similar to that of $Li_2FeP_2O_7$ and $Na_4Fe_3(PO_4)_2P_2O_7$. This structural rearrangement is only observed upon the first charging process, and the structural and Fe^{3+}/Fe^{2+} redox reversibility is retained upon the subsequent cycles with a small volume change (ΔV = ca. 3.5 %), which contributes to the good cyclability of the electrochemical processes. Sodium extraction occurs primarily at Na3, followed by Na1 and then Na2 sites for the initial charging. The sodium insertion occurred at Na2, Na3, and Na/Fe1 sites for the first discharging and is reversible in subsequent cycles. Understanding of the irreversible reaction and the following reversible reaction mechanism, which might be common among similar crystal structures, should be helpful in the design of new cathode candidates for next generation batteries.

References

(1) Yabuuchi, N.; Yoshida, H.; Komaba, S. *Electrochemistry* **2012**, *80*, 716–719.

(2) Kubota, K.; Yabuuchi, N.; Yoshida, H.; Dahbi, M.; Komaba, S. *MRS Bull.* **2014**, *39*, 416–422.

(3) Yabuuchi, N.; Kajiyama, M.; Iwatate, J.; Nishikawa, H.; Hitomi, S.; Okuyama, R.; Usui, R.; Yamada, Y.; Komaba, S. *Nat. Mater.* **2012**, *11*, 512–517.

(4) Moreau, P.; Guyomard, D.; Gaubicher, J.; Boucher, F. *Chem. Mater.* **2010**, *22*, 4126–4128.

(5) Lu, J.; Chung, S. C.; Nishimura, S.; Yamada, A. *Chem. Mater.* **2013**, 131029074415004.

(6) Ellis, B. L.; Makahnouk, W. R. M.; Makimura, Y.; Toghill, K.; Nazar, L. F. *Nat. Mater.* **2007**, *6*, 749–753.

(7) Barpanda, P.; Liu, G.; Ling, C. D.; Tamaru, M.; Avdeev, M.; Chung, S.-C.; Yamada, Y.; Yamada, A. *Chem. Mater.* **2013**, 130826145907003.

(8) Kim, H.; Park, I.; Seo, D.-H.; Lee, S.; Kim, S.-W.; Kwon, W. J.; Park, Y.-U.; Kim, C. S.; Jeon, S.; Kang, K. *J. Am. Chem. Soc.* **2012**, *134*, 10369–10372.

(9) Kim, H.; Park, I.; Lee, S.; Kim, H.; Park, K.-Y.; Park, Y.-U.; Kim, H.; Kim, J.; Lim, H.-D.; Yoon, W.-S.; Kang, K. *Chem. Mater.* **2013**, *25*, 3614–3622.

(10) Padhi, A. K. *J. Electrochem. Soc.* **1998**, *145*, 1518.

(11) Recham, N.; Chotard, J.-N.; Dupont, L.; Delacourt, C.; Walker, W.; Armand, M.; Tarascon, J.-M. *Nat. Mater.* **2010**, *9*, 68–74.

(12) Barpanda, P.; Ati, M.; Melot, B. C.; Rousse, G.; Chotard, J.-N.; Doublet, M.-L.; Sougrati, M. T.; Corr, S. A.; Jumas, J.-C.; Tarascon, J.-M. *Nat. Mater.* **2011**, *10*, 772–779.

(13) Recham, N.; Rousse, G.; Sougrati, M. T.; Chotard, J.-N.; Frayret, C.; Mariyappan, S.; Melot, B. C.; Jumas, J.-C.; Tarascon, J.-M. *Chem. Mater.* **2012**, *24*, 4363–4370.

(14) Subban, C. V.; Ati, M.; Rousse, G.; Abakumov, A. M.; Van Tendeloo, G.; Janot, R.; Tarascon, J.-M. *J. Am. Chem. Soc.* **2013**, *135*, 3653–3661.

(15) Reynaud, M.; Ati, M.; Melot, B. C.; Sougrati, M. T.; Rousse, G.; Chotard, J.-N.; Tarascon, J.-M. *Electrochem. commun.* **2012**, *21*, 77–80.

(16) Lander, L.; Reynaud, M.; Rousse, G.; Sougrati, M. T.; Laberty-Robert, C.; Messinger, R. J.; Deschamps, M.; Tarascon, J.-M. *Chem. Mater.* **2014**, *26*, 4178–4189.

(17) Sun, M.; Rousse, G.; Abakumov, A. M.; Van Tendeloo, G.; Sougrati, M.-T.; Courty, M.; Doublet, M.-L.; Tarascon, J.-M. *J. Am. Chem. Soc.* **2014**, *136*, 12658–12666.

(18) Reynaud, M.; Rousse, G.; Abakumov, A. M.; Sougrati, M. T.; Van Tendeloo, G.; Chotard, J.-N.; Tarascon, J.-M. *J. Mater. Chem. A* **2014**, *2*, 2671–2680.

(19) Barpanda, P.; Oyama, G.; Ling, C. D.; Yamada, A. *Chem. Mater.* **2014**, *26*, 1297–1299.

(20) Barpanda, P.; Chotard, J.-N.; Recham, N.; Delacourt, C.; Ati, M.; Dupont, L.; Armand, M.; Tarascon, J.-M. *Inorg. Chem.* **2010**, *49*, 7401–7413.

(21) Ati, M.; Dupont, L.; Recham, N.; Chotard, J.-N. J. N.; Walker, W. T.; Davoisne, C.; Barpanda, P.; Sarou-Kanian, V.; Armand, M.; Tarascon, J.-M. J. M. *Chem. Mater.* **2010**, *22*, 4062–4068.

(22) Barpanda, P.; Oyama, G.; Nishimura, S.; Chung, S.-C.; Yamada, A. *Nat. Commun.* **2014**, *5*, 4358.

(23) Fisher, D. J. *Am. Mineral.* **1955**, *40*, 1100–1109.

(24) Oyama, G.; Nishimura, S.; Suzuki, Y.; Okubo, M.; Yamada, A. *ChemElectroChem* **2015**, *2*, 1019–1023.

(25) Chung, S. C.; Barpanda, P.; Nishimura, S.; Yamada, Y.; Yamada, A. *Phys. Chem. Chem. Phys.* **2012**, *14*, 8678.

(26) Komaba, S.; Ishikawa, T.; Yabuuchi, N.; Murata, W.; Ito, A.; Ohsawa, Y. *ACS Appl. Mater. Interfaces* **2011**, *3*, 4165–4168.

(27) Harris, R. K.; Becker, E. D.; Cabral de Menezes, S. M.; Goodfellow, R.; Granger, P. *Magn. Reson. Chem.* **2002**, *40*, 489–505.

(28) Massiot, D.; Fayon, F.; Capron, M.; King, I.; Le Calve, S.; Alonso, B.; Durand, J.-O.; Bujoli, B.; Gan, Z.; Hoatson, G. *Magn. Reson. Chem.* **2002**, *40*, 70–76.

(29) Ravel, B.; Newville, M. *J. Synchrotron Radiat.* **2005**, *12*, 537–541.

(30) Nytén, A.; Abouimrane, A.; Armand, M.; Gustafsson, T.; Thomas, J. O. *Electrochem. commun.* **2005**, *7*, 156–160.

(31) Masese, T.; Orikasa, Y.; Tassel, C.; Kim, J.; Minato, T.; Arai, H.; Mori, T.; Yamamoto, K.; Kobayashi, Y.; Kageyama, H.; Ogumi, Z.; Uchimoto, Y. *Chem. Mater.* **2014**, *26*, 1380–1384.

(32) Shimizu, D.; Nishimura, S.; Barpanda, P.; Yamada, A. *Chem. Mater.* **2012**, *24*, 2598–2603.

(33) Ye, T.; Barpanda, P.; Nishimura, S.; Furuta, N.; Chung, S.-C.; Yamada, A. *Chem. Mater.* **2013**, *25*, 3623–3629.

(34) Wong, L. L.; Chen, H. M.; Adams, S. *Phys. Chem. Chem. Phys.* **2015**, *17*, 9186–9193.

(35) Brown, I. D. *Chem. Rev.* **2009**, *109*, 6858–6919.

(36) Grey, C. P.; Dupré, N. *Chem. Rev.* **2004**, *104*, 4493–4512.

(37) Clément, R. J.; Bruce, P. G.; Grey, C. P. *J. Electrochem. Soc.* **2015**, *162*, A2589–A2604.

(38) Clément, R. J.; Pell, A. J.; Middlemiss, D. S.; Strobridge, F. C.; Miller, J. K.; Whittingham, M. S.; Emsley, L.; Grey, C. P.; Pintacuda, G. *J. Am. Chem. Soc.* **2012**, *134*, 17178–17185.

(39) Middlemiss, D. S.; Ilott, A. J.; Clément, R. J.; Strobridge, F. C.; Grey, C. P. *Chem. Mater.* **2013**, *25*, 1723–1734.

(40) Oyama, G.; Pecher, O.; Griffith, K. J.; Nishimura, S.; Pigliapochi, R.; Grey, C. P.; Yamada, A. *submitted.*

7. Combined Experimental and Computational Analyses on Electronic Structure of Alluaudite Sodium Iron Sulfate

7.1 Introduction

Reduction of the cost is a pressing issue for full-scale adoption of rechargeable batteries in large-scale energy systems (e.g. on-grid storage and electric vehicles). In this pursuit, sodium-ion battery is one of the most promising candidates replacing current lithium-ion battery owing to low cost, high natural abundance and even geographical distribution of sodium resources.[1–3] However, cathode materials have limited both the volumetric and gravimetric energy densities of the sodium ion battery systems; therefore, considerable efforts have been devoted to identify suitable candidates.

To date, a number of layered oxides, Na_xMO_2 (M: 3d transition metals)[4–9], phosphates (e.g. olivine-Na_xFePO_4[10,11], NASICON-$Na_{3-2x}V_2(PO_4)_3$[12], $Na_{2-x}FeP_2O_7$[13], $Na_{4-3x}Fe_3(PO_4)_2(P_2O_7)$[14,15]), and fluorophospates (e.g. $Na_{2-x}FePO_4F$[16], $Na_{1.5-x}VPO_{4.8}F_{0.7}$[17,18], $Na_{3-2x}V_2(PO_4)_2F_3$[19–21]) have been reported as active cathode materials, but few of which exhibit comparable electrode performances with the practical lithium-ion battery cathode materials.

Inspired by the wide variety of sulfate-based high-voltage cathodes for lithium batteries (e.g. tavorite- and triplite-$Li_{1-x}FeSO_4F$[22,23], layered $Li_{1-x}FeSO_4OH$[24], marinate, orthorhombic $Li_{2-x}Fe(SO_4)_2$[25,26]), alluaudite-type sodium iron sulfate $Na_{2.56}Fe_{1.72}(SO_4)_3$ was discovered recently as a possible sodium battery cathode candidate. It has the highest redox potential (ca. 3.8 V versus Na^+/Na, corresponding to 4.1 V versus Li^+/Li) among all the reported cathode materials driven by the Fe^{3+}/Fe^{2+} redox couple.[27] The extremely high potential can be rationalized to the strong inductive effect[28] caused by the sulfate group; consequently, hybridization of Fe 3d orbital and O 2p orbital is expected to be minimal. However, till date, no study has focused on the electronic structure, especially the one near the Fermi level, which is closely related to the redox behaviors of electrodes. In this regard, soft X-ray absorption spectroscopy (XAS) combined with semi-empirical simulations or *ab initio* calculations is a powerful technique for extracting element-selective information of unoccupied Fe 3*d* and O 2*p* orbitals.

In the present study, the electronic structures of $Na_{2.56}Fe_{1.72}(SO_4)_3$ and its desodiated phases are investigated by combining soft XAS, ligand field multiplet (LFM) simulations, and *ab initio* calculations. Variation of the valence state, crystal field strength, and degree of covalency will be discussed.

7.2 Experimental and computational methods

$Na_{2.56}Fe_{1.72}(SO_4)_3$ compounds were prepared via a solid state synthesis as reported previously.[29] For electrochemical tests, 80 wt% active material, 13 wt% carbon black (Ketjen Black, Lion Corp., ECP) and 7 wt% polytetrafluoro-ethylene (PTFE) binder were mixed to make positive electrode tapes (about 10 mm in diameter) by a pestle and mortar. The tapes were cast onto Al meshes and dried at 393 K for 12 hours. 2032-type coin cells were assembled in an Ar filled glovebox using the above-prepared cathode tapes, 1 mol dm^{-3} $NaClO_4$ dissolved in propylene carbonate (PC) electrolyte (Tomiyama Pure Chemical Industries, Ltd.), glass fiber separators, and Na metal anodes. Galvanostatic charge-discharge tests were operated between 2.0–4.5 V at a C/20 current rate (5.3 mAg^{-1}) under a TOSCAT-3100 charge-discharge unit (Toyo System). After the charge-discharge experiments, the cells were disassembled in an Ar-filled glovebox. The positive electrode tapes were removed from Al mesh and carefully washed with dimethyl carbonate (DMC) (Kishida Chemical) to remove the electrolytes.

Soft X-ray absorption spectroscopy (XAS) measurements were performed for the charged and discharged electrodes at BL07LSU in SPring-8[30]. The samples were attached with carbon tapes to the sample holders, and were transferred to a vacuum chamber without air exposure. XAS for O *K*-edge was conducted in the bulk-sensitive partial fluorescence yield (PFY) mode. Inverse-PEY

(IPFY) mode was carried out for Fe $L_{2,3}$-edge to suppress self-absorption and saturation effects[31]. Energy resolution of the incident beam was approximately 100 meV. All the spectra were recorded at room temperature.

Ab initio calculations were conducted with the *Vienna ab initio* simulation package (VASP). Spin polarized calculations with the PBE exchange-correlation functional[32] were conducted. A Hubbard-type correction GGA+ U (U = 4.2 eV) was used to describe the localized 3d electrons of the Fe ions. Projector augmented wave (PAW) method as implemented in the VASP program was employed. Energy cutoff of 520 eV for the plane-wave basis and 4×4×4 Monkhorst–Pack k-point meshes were applied. Convergence of the forces was set to 0.020 eV $Å^{-1}$. Ferromagnetic and antiferromagnetic orderings of the Fe ions were considered. In the calculation, the off-stoichiometric compositions of $Na_{2.5}Fe_{1.75}(SO_4)_3$ and $Na_{0.75}Fe_{1.75}(SO_4)_3$ were approximated within $a \times b \times 2c$ supercells. For a direct comparison with the experimental XAS spectra, the calculated p-DOS curves are manually shifted to 528 and 530 eV for the pristine, and desodiated phases, respectively. Partitions of electron charge density were performed with the Bader analysis method[33,34].

Ligand field multiplet (LFM) calculations were performed to simulate the experimental Fe $L_{2,3}$-edge XAS of $Na_{2.56}Fe_{1.72}(SO_4)_3$. The simulation was also done for XAS spectrum of the olivine-type $LiFePO_4$, which was previously reported by Kurosumi *et al.*[35], to get semi-quantitative information for the inductive effect. The simulated spectrum of $LiFePO_4$ is manually shifted with −0.64 eV. The CTM4XAS program,[36] which is a freeware program of the Cowan–Butler–Thole code[37–39], was employed. In this method, the relativistic Hartree-Fock atomic calculations are performed for the ground and excited states. Several parameters can be adjusted to mimic the conditions of an ion in a solid matrix; scaling down of the Slater integrals (F_{dd}, F_{pd}, G_{pd}) from their values for respective free M^{n+} ions, and crystal field parameter (10Dq). Following the previous report by Hibberd *et al.*[40], a charge transfer parameter was not used for the simulations in the present analyses; the effect is taken into account by the reduction of the Slater integrals. Core-hole lifetime and experimental resolution effects were taken into account by broadening the spectra with Lorentzian and Gaussian functions. $\Gamma(L_3) = 0.2$, $\Gamma(L_2) = 0.2$ and $G = 0.2$ eV were applied, where Γ and G represent half-width half-maximum values of the Lorentzian and the Gaussian functions, respectively.

7.3 Electronic structure changes during the charging/discharging processes

7.3.1 Fe $L_{2,3}$-edge

Figure 7.1 (i) shows the galvanostatic charge-discharge curves of $Na_{2.56-y}Fe_{1.72}(SO_4)_3$ upon the first two cycles. Some irreversible processes are observed for the first and the second cycles, details of which were discussed in ref. 27, and 41. Here, the second cycle was focused to elucidate the reversible feature.

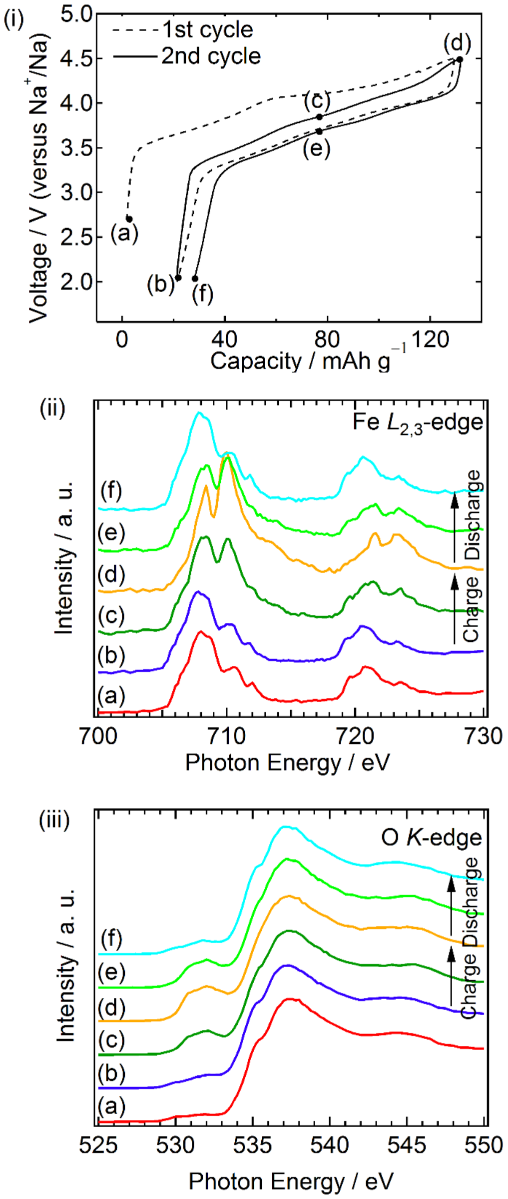

Figure 7.1 (i) Galvanostatic charge-discharge curves of the alluaudite $Na_{2.56}Fe_{1.72}(SO_4)_3$ electrode at a C/20 current rate. The electrochemical processes were stopped at different states of charge (a)-(f). (ii) Fe $L_{2,3}$-edge of alluaudite $Na_{2.56}Fe_{1.72}(SO_4)_3$ electrode at (a)-(f). (iii) *Ex situ* O *K*-edge of the alluaduite electrodes at (a)-(f).

Fe $L_{2,3}$-edge (2*p*-3*d*) XAS at different states of charge (a)-(f) are shown in Fig. 7.1 (ii). Peaks at lower (708-712 eV) and higher (719-725 eV) energies correspond to the Fe L_3-, and L_2-edges, respectively. The overall spectra are similar to those of the olivine Li_xFePO_4 system[42]. Upon the desodiation, the L_3-edge peak at 708 eV decreases, while the peak at 710 eV increases toward the fully charged state (d). As is reported for Li_xFePO_4 system[43], the observed intensity ratio difference can be interpreted as the multiplet structure change due to the oxidation of Fe^{2+} to Fe^{3+}. In contrast, the intensity of the L_3-edge peak at 710 eV decreases and the peak at 708 eV increases toward the discharged state (f) upon the sodiation process, suggesting the reduction of Fe^{3+} to Fe^{2+}. The observed reversible change for the electronic states of iron is consistent with the previous Mössbauer and X-ray near edge absorption spectroscopy (XANES) analyses.[41]

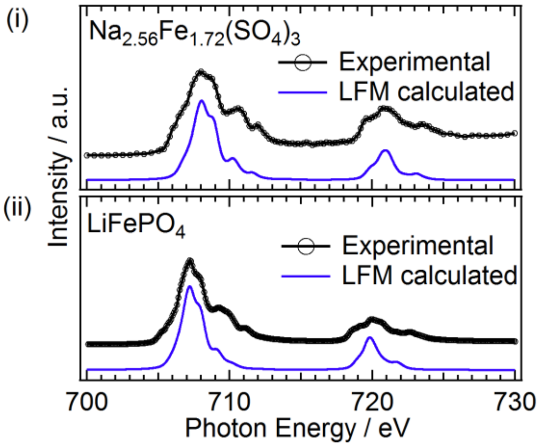

Figure 7.2 Experimental Fe $L_{2,3}$-edge XAS and LFM calculated spectra of pristine $Na_{2.56}Fe_{1.72}(SO_4)_3$ (upper panel) and $LiFePO_4$ (lower panel). The experimental curve of $LiFePO_4$ is replotted using the data in Ref. 35.

Figure 7.2 (i) shows LFM simulation for the experimental Fe $L_{2,3}$-edge XAS of the pristine phase. The simulated curve shows good agreement with the experimental XAS spectrum of $Na_{2.56}Fe_{1.72}(SO_4)_3$. The parameters used for the simulations are listed in Table 7.1. The obtained crystal field splitting ($10Dq = 0.3$) is smaller than typical values of high-spin Fe^{2+} because the core hole in the final state increases the localization of the iron 3*d* orbital, which is common under the XAS condition[40]. Besides, the Slater integral is required to be reduced to 90 % (with −10 % reduction) from the free Fe^{2+} ion. The reduction of the Slater integral is caused by the quantum mechanical mixing of iron 3*d* with ligand orbital and is commonly referred to as the "nephelauxetic effect"[40,44,45]. Thereby, a lower reduction of the Slater integral indicates the electronic state of iron in $Na_{2.56}Fe_{1.72}(SO_4)_3$ is closer to that of an a free Fe^{2+} ion. A similar simulation for the olivine-type $LiFePO_4$ gives a Slater integral reduction down to 70 % (Fig. 7.2 (ii) and Table 7.1), indicating that iron in $LiFePO_4$ is less ionic than in $Na_{2.56}Fe_{1.72}(SO_4)_3$..This is consistent with the observed average potential of 3.4 V and 3.8 V for $LiFePO_4$ and $Na_{2.56}Fe_{1.72}(SO_4)_3$ respectively.[27,46] The sizable difference between Slater integral reduction for the two compounds shows that LFM analyses on the Fe $L_{2,3}$-edge XAS may be an important tool to semi-quantitatively evaluate the relative inductive effects of counteranions in cathode materials of lithium and sodium-ions batteries.

Table 7.1. Parameters applied for LFM calculations. Simulated Fe $L_{2,3}$-edge XAS for pristine and desodiated phases are shown in Fig. 7.2.

	Valence state	Symmetry	Crystal field splitting 10*Dq* (eV)	Slater integral reduction (%)
$Na_{2.56}Fe_{1.72}(SO_4)_3$	Fe^{2+}	O_h	0.3	90
$LiFePO_4$	Fe^{2+}	O_h	0.5	70

7.3.2 O *K*-edge

O *K*-edge (1*s*-2*p*) XAS includes direct information about the hybridization of oxygen with other atoms, because an ideally ionized O^{2-} ion has no empty 2*p* orbital for the excitation.[47] The obtained spectra at the different states of charge (a)-(f) are shown in Fig. 7.1 (iii). For the pristine phase, the relative peak intensity is barely observed below the threshold of the main O *K*-edge at 534 eV (referred to a pre-edge region). Upon the charge (desodiation) process, the intensity of the pre-edge peak visibly increases, and reversibly decreased upon the subsequent discharge (sodiation) process. The intensity increment of the pre-edge peaks are caused by the stronger hybridization at the desodiated phase mainly due to the shorter Fe–O bond length and larger overlap of iron *d* states with oxygen *p* states for Fe^{3+} than that for Fe^{2+}, details of which will be discussed below.

Negligible change is observed above the pre-edge region during the desodiation and sodiation processes. This region is attributed to the hybridized bands between oxygen *p* and sulfurous *p* orbitals, thereby the covalency of S–O bonds marginally change during the charge-discharge measurements.

In order to obtain an overall insight for DOS near the Fermi level and to directly compare with the observed O *K*-edge XAS spectra, the *ab initio* calculations are performed. The DOS of the pristine alluaudite sodium iron sulfate shows overall band structure similar to those of other oxyanionic compounds, such as olivine-$LiFePO_4$[48], tavorite-, and triplite-$LiFeSO_4F$[49] (Fig. 7.3 (i)). The spin-up *d* states of iron show strong overlap with the oxygen *s*, *p* states, with hybridized states extend from –5.92 to –0.76 eV. The spin-down *d* states are however much more localized. As sodium is removed and iron is oxidized to Fe^{3+}, the spin-down *d* states of iron move down in energy and appear below the oxygen bands (Fig. 7.3 (ii)). This is due to the increase in electrostatic charge on iron and the exchange stabilization of the d^5 states. Now the spin-down *d* states show stronger hybridization with the oxygen *p* states, leading to the intensity increment of the O *K* pre-edge for desodiation.

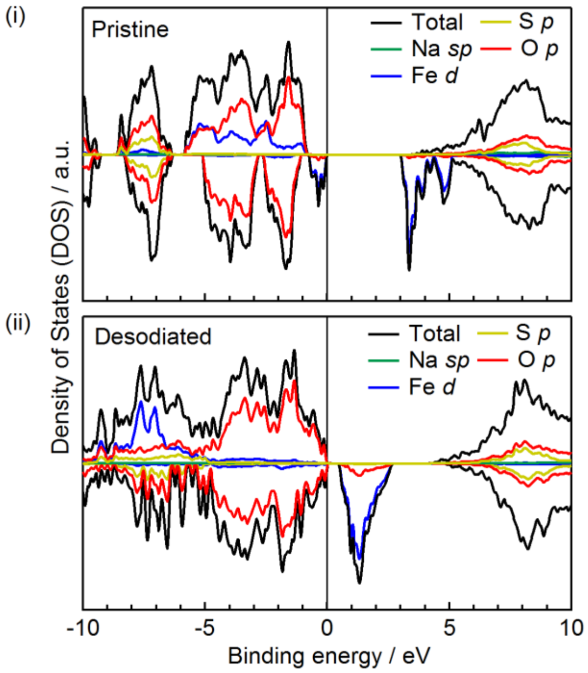

Figure 7.3 Total and partial density of states (DOS) profiles for (i) pristine $Na_{2.5}Fe_{1.75}(SO_4)_3$ phase and (ii) desodiated $Na_{0.75}Fe_{1.75}(SO_4)_3$ phases calculated with GGA+*U* (*U* = 4.2 eV). Total DOS are illustrated as a black dashed line, while partial DOS for Na *sp*, Fe*3d*, S 3*p*, and O 2*p* orbitals are shown as green, blue, yellow, and red solid lines, respectively.

The O *K*-edge XAS spectra of the pristine and the desodiated phases are compared with calculated partial DOS (p-DOS) in Fig. 7.4. The overall features of oxygen p-DOS curves agree with the O *K*-edge XAS for both the pristine (Fig. 7.4 (i)) and the desodiated (Fig. 7.4 (ii)) phases. As is discussed above, the pre-edge region is attributed to a hybridized band between iron 3*d* and oxygen 2*p* orbitals. The absence of the pre-edge peak for the pristine phase suggests the localized Fe 3*d* bands, which is consistent with the results of Fe $L_{2,3}$-edge XAS. However, the O *K*-edges of $LiFePO_4$ reported in ref. 42 and 50 also show almost no intensity at their pre-edge regions. This suggests the O *K*-edge XAS is not sensitive to the covalency difference from the inductive effects of sulfate and phosphate groups.

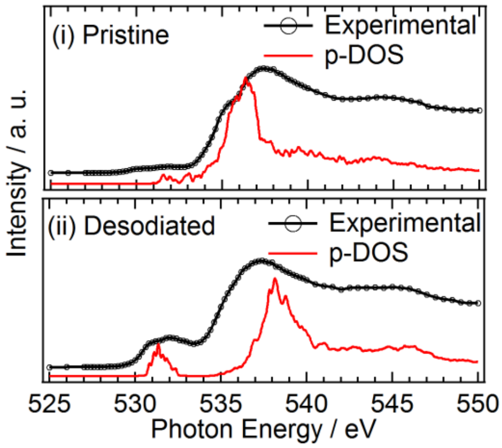

Figure 7.4 Experimental O *K*-edge XAS and DFT calculated partial DOS (p-DOS) of unoccupied oxygen orbitals for (i) pristine and (ii) desodiated phases.

The Bader charge analyses supports the strong inductive effect of the sulfate group further (Table 7.2). The mean Bader charge of Fe for the pristine phase is calculated to be +1.51, which is one of the highest values among the reported polyanionic compounds[51]; this reflects strongly ionic character of the Fe–O bond through the inductive effect of the sulfate group. However, during desodiation the iron ions compensate only 0.39 out of the 0.90 change in charges (corresponding to about 43 %), the rests are mainly compensated by the oxygen ions. This suggests the coordinated oxygen ions participate in the electrochemical redox reaction through the Fe–O bonds, despite the exceedingly ionic character of the Fe-O bonds under the inductive effect of the sulfate group.

Table 7.2 Mean Bader charges of each ions for the pristine, desodiated phases and their differences.

	Na	Fe	S	O
Pristine	+0.90	+1.51	+3.87	–1.37
Desodiated	+0.90	+1.90	+3.81	–1.29
Difference	0.00	+0.39	–0.06	+0.09

7.3.3 Conclusion

In summary, the electronic structure of the alluaudite-type $Na_{2.56}Fe_{1.72}(SO_4)_3$ is surveyed via combined analyses of *ab initio* calculations, soft-XAS, and LFM simulations. The Fe $L_{2,3}$-edge XAS indicates the reversible oxidation/reduction of the iron valence state for the electrochemical desodiation/sodiation processes. The LFM simulation shows the inductive effect of the sulfate group in the pristine $Na_{2.56}Fe_{1.72}(SO_4)_3$ is exceedingly strong, and iron is in almost a free Fe^{2+} state, leading to the highest redox potential among any Fe^{3+}/Fe^{2+} environments. Both the oxygen *K*-edge XAS and *ab initio* calculations indicate the hybridization between iron 3*d* and oxygen 2*p* orbitals increases upon the desodiation process, and it reversibly decreases upon the subsequent sodiation process. The present spectroscopic analyses are principally applicable for manifold oxyanionic cathode materials to reveal electronic structure changes during charge-discharge processes and to evaluate the strength of inductive effect in a semi-quantitative way.

References

(1) Kundu, D.; Talaie, E.; Duffort, V.; Nazar, L. F. *Angew. Chemie Int. Ed.* **2015**, *54*, 3431–3448.

(2) Slater, M. D.; Kim, D.; Lee, E.; Johnson, C. S. *Adv. Funct. Mater.* **2013**, *23*, 947–958.

(3) Ellis, B. L.; Nazar, L. F. *Curr. Opin. Solid State Mater. Sci.* **2012**.

(4) Braconnier, J. J.; Delmas, C.; Hagenmuller, P. *Mater. Res. Bull.* **1982**, *17*, 993–1000.

(5) Komaba, S.; Takei, C.; Nakayama, T.; Ogata, A.; Yabuuchi, N. *Electrochem. commun.* **2010**, *12*, 355–358.

(6) Ma, X.; Chen, H.; Ceder, G. *J. Electrochem. Soc.* **2011**, *158*, A1307.

(7) Takeda, Y.; Nakahara, K.; Nishijima, M.; Imanishi, N.; Yamamoto, O.; Takano, M.; Kanno, R. *Mater. Res. Bull.* **1994**, *29*, 659–666.

(8) Wang, X.; Liu, G.; Iwao, T.; Okubo, M.; Yamada, A. *J. Phys. Chem. C* **2014**, *118*, 2970–2976.

(9) Mortemard de Boisse, B.; Carlier, D.; Guignard, M.; Delmas, C. *J. Electrochem. Soc.* **2013**, *160*, A569–A574.

(10) Moreau, P.; Guyomard, D.; Gaubicher, J.; Boucher, F. *Chem. Mater.* **2010**, *22*, 4126–4128.

(11) Lu, J.; Chung, S. C.; Nishimura, S.; Yamada, A. *Chem. Mater.* **2013**, 131029074415004.

(12) Saravanan, K.; Mason, C. W.; Rudola, A.; Wong, K. H.; Balaya, P. *Adv. Energy Mater.* **2013**, *3*, 444–450.

(13) Barpanda, P.; Liu, G.; Ling, C. D.; Tamaru, M.; Avdeev, M.; Chung, S.-C.; Yamada, Y.; Yamada, A. *Chem. Mater.* **2013**, 130826145907003.

(14) Kim, H.; Park, I.; Seo, D.-H.; Lee, S.; Kim, S.-W.; Kwon, W. J.; Park, Y.-U.; Kim, C. S.; Jeon, S.; Kang, K. *J. Am. Chem. Soc.* **2012**, *134*, 10369–10372.

(15) Kim, H.; Park, I.; Lee, S.; Kim, H.; Park, K.-Y.; Park, Y.-U.; Kim, H.; Kim, J.; Lim, H.-D.; Yoon, W.-S.; Kang, K. *Chem. Mater.* **2013**, *25*, 3614–3622.

(16) Ellis, B. L.; Makahnouk, W. R. M.; Makimura, Y.; Toghill, K.; Nazar, L. F. *Nat. Mater.* **2007**, *6*, 749–753.

(17) Sauvage, F.; Quarez, E.; Tarascon, J. M.; Baudrin, E. *Solid state Sci.* **2006**, *8*, 1215–1221.

(18) Park, Y.-U.; Seo, D.-H.; Kwon, H.-S.; Kim, B.; Kim, J.; Kim, H.; Kim, I.; Yoo, H.-I.; Kang, K. *J. Am. Chem. Soc.* **2013**, *135*, 13870–13878.

(19) Gover, R.; Bryan, A.; Burns, P.; Barker, J. *Solid State Ionics* **2006**, *177*, 1495–1500.

(20) Shakoor, R. A.; Seo, D.-H.; Kim, H.; Park, Y.-U.; Kim, J.; Kim, S.-W.; Gwon, H.; Lee, S.; Kang, K. *J. Mater. Chem.* **2012**, *22*, 20535.

(21) Liu, Z.; Hu, Y.-Y.; Dunstan, M. T.; Huo, H.; Hao, X.; Zou, H.; Zhong, G.; Yang, Y.; Grey, C. P. *Chem. Mater.* **2014**, *26*, 2513–2521.

(22) Recham, N.; Chotard, J.-N.; Dupont, L.; Delacourt, C.; Walker, W.; Armand, M.; Tarascon, J.-M. *Nat. Mater.* **2010**, *9*, 68–74.

(23) Barpanda, P.; Ati, M.; Melot, B. C.; Rousse, G.; Chotard, J.-N.; Doublet, M.-L.; Sougrati, M. T.; Corr, S. A.; Jumas, J.-C.; Tarascon, J.-M. *Nat. Mater.* **2011**, *10*, 772–779.

(24) Subban, C. V.; Ati, M.; Rousse, G.; Abakumov, A. M.; Van Tendeloo, G.; Janot, R.; Tarascon, J.-M. *J. Am. Chem. Soc.* **2013**, *135*, 3653–3661.

(25) Reynaud, M.; Ati, M.; Melot, B. C.; Sougrati, M. T.; Rousse, G.; Chotard, J.-N.; Tarascon, J.-M. *Electrochem. commun.* **2012**, *21*, 77–80.

(26) Lander, L.; Reynaud, M.; Rousse, G.; Sougrati, M. T.; Laberty-Robert, C.; Messinger, R. J.; Deschamps, M.; Tarascon, J.-M. *Chem. Mater.* **2014**, *26*, 4178–4189.

(27) Barpanda, P.; Oyama, G.; Nishimura, S.; Chung, S. C.; Yamada, A. *Nat. Commun.* **2014**, *5*, 4358.

(28) Padhi, A. K. *J. Electrochem. Soc.* **1998**, *145*, 1518.

(29) Oyama, G.; Nishimura, S.; Suzuki, Y.; Okubo, M.; Yamada, A. *ChemElectroChem* **2015**, *2*, 1019–1023.

(30) Senba, Y.; Yamamoto, S.; Ohashi, H.; Matsuda, I.; Fujisawa, M.; Harasawa, A.; Okuda, T.; Takahashi, S.; Nariyama, N.; Matsushita, T.; Ohata, T.; Furukawa, Y.; Tanaka, T.; Takeshita, K.; Goto, S.; Kitamura, H.; Kakizaki, A.; Oshima, M. *Nucl. Instruments Methods Phys. Res. Sect. A Accel. Spectrometers, Detect. Assoc. Equip.* **2011**, *649*, 58–60.

(31) Achkar, A. J.; Regier, T. Z.; Wadati, H.; Kim, Y.-J.; Zhang, H.; Hawthorn, D. G. *Phys.*

Rev. B **2011**, *83*, 081106.

(32) Perdew, J. P.; Burke, K.; Ernzerhof, M. *Phys. Rev. Lett.* **1996**, *77*, 3865–3868.

(33) Richard F. W. Bader. *The Quantum Theory of Atoms in Molecules*; Oxford University Press: New York, 1990.

(34) Henkelman, G.; Arnaldsson, A.; Jónsson, H. *Comput. Mater. Sci.* **2006**, *36*, 354–360.

(35) Kurosumi, S.; Nagamura, N.; Toyoda, S.; Horiba, K.; Kumigashira, H.; Oshima, M.; Furutsuki, S.; Nishimura, S.; Yamada, A.; Mizuno, N. *J. Phys. Chem. C* **2011**, *115*, 25519–25522.

(36) Stavitski, E.; de Groot, F. M. F. *Micron* **2010**, *41*, 687–694.

(37) de Groot, F. M. F.; Fuggle, J. C.; Thole, B. T.; Sawatzky, G. A. *Phys. Rev. B* **1990**, *42*, 5459–5468.

(38) Cowan, R. D. *J. Opt. Soc. Am.* **1968**, *58*, 808.

(39) Thole, B. T.; Van Der Laan, G.; Butler, P. H. *Chem. Phys. Lett.* **1988**, *149*, 295–299.

(40) Hibberd, A. M.; Doan, H. Q.; Glass, E. N.; de Groot, F. M. F.; Hill, C. L.; Cuk, T. *J. Phys. Chem. C* **2015**, *119*, 4173–4179.

(41) Oyama, G.; Pecher, O.; Griffith, K. J.; Nishimura, S.; Pigliapochi, R.; Grey, C. P.; Yamada, A. *submitted.*

(42) Augustsson, A.; Zhuang, G. V; Butorin, S. M.; Osorio-Guillén, J. M.; Dong, C. L.; Ahuja, R.; Chang, C. L.; Ross, P. N.; Nordgren, J.; Guo, J.-H. *J. Chem. Phys.* **2005**, *123*, 184717.

(43) Liu, X.; Liu, J.; Qiao, R.; Yu, Y.; Li, H.; Suo, L.; Hu, Y.; Chuang, Y.-D.; Shu, G.; Chou, F.; Weng, T.-C.; Nordlund, D.; Sokaras, D.; Wang, Y. J.; Lin, H.; Barbiellini, B.; Bansil, A.; Song, X.; Liu, Z.; Yan, S.; Liu, G.; Qiao, S.; Richardson, T. J.; Prendergast, D.; Hussain, Z.; de Groot, F. M. F.; Yang, W. *J. Am. Chem. Soc.* **2012**, *134*, 13708–13715.

(44) Tchougréeff, A. L.; Dronskowski, R. *Int. J. Quantum Chem.* **2009**, *109*, 2606–2621.

(45) Prigogine, I.; Jørgensen, C. K. *Adv. Chem. Phys.* **1963**, *5*, 33–146.

(46) Padhi, A. K.; Nanjundaswamy, K. S.; Goodenough, J. B. *J. Electrochem. Soc.* **1997**, *144*, 1188–1193.

(47) Groot, F. M. F. de; Abbate, M.; Elp, J. van; Sawatzky, G. A.; Ma, Y. J.; Chen, C. T.; Sette, F. *J. Phys. Condens. Matter* **1993**, *5*, 2277–2288.

(48) Zhou, F.; Kang, K.; Maxisch, T.; Ceder, G.; Morgan, D. *Solid State Commun.* **2004**, *132*, 181–186.

(49) Chung, S. C.; Barpanda, P.; Nishimura, S.; Yamada, Y.; Yamada, A. *Phys. Chem. Chem. Phys.* **2012**, *14*, 8678.

(50) Yang, S.; Wang, D.; Liang, G.; Yiu, Y. M.; Wang, J.; Liu, L.; Sun, X.; Sham, T.-K. *Energy Environ. Sci.* **2012**, *5*, 7007.

(51) Melot, B. C.; Scanlon, D. O.; Reynaud, M.; Rousse, G.; Chotard, J.-N.; Henry, M.; Tarascon, J.-M. *ACS Appl. Mater. Interfaces* **2014**, *6*, 10832–10839.

General conclusion and future perspectives

Rechargeable batteries are ubiquitous in our modern life. Lithium-ion batteries were first applied for mobile devices (e.g. mobile/smart phone, laptop computers, digital cameras, etc.) and later for larger-scale systems such as hybrid/electric vehicles, and in-grid energy storage systems. For extending the range of applications of battery technology even further, the reduction of battery cost needs to be accomplished without sacrificing the battery performance. Among the battery components, the cost of the cathode is the highest mainly due to the use of cobalt as a redox center.

One of the most promising strategies to reduce the material cost is the utilization of iron, which is the fourth most abundant element in the earth's crust and an environmentally benign element. In the present thesis, exploration of new iron based cathode materials and their reaction mechanism analyses have been conducted in Chapters 2-7.

In chapter 2, kinetics of two-phase electrochemical reaction in Li_xFePO_4 was investigated by combining potential-step chronoamperometry and Kolmogorov-Johnson-Mehl-Avrami (KJMA) model. The phase transition proceeds with one-dimensional phase-boundary movement, which is consistent with previously reported mechanism.

In chapter 3, the heterosite $FePO_4$, which is the delithiated phase of olivine $LiFePO_4$, has been examined as a possible magnesium battery cathode. The heterosite $FePO_4$ electrode shows partially reversible capacity as a potential Mg battery cathode. Activation energy for Mg^{2+} diffusion is over three times larger than that of Li^+, and partial fraction of the $FePO_4$ phase is suggested to be an amorphous phase by non-topochemical Mg^{2+} intercalation.

In Chapters 4-7, it was shown that the alluaudite-type sodium iron sulfate registers the highest ever Fe^{3+}/Fe^{2+} redox potential at 3.8 V (versus Na/Na^+) along with fast rate kinetics. The Na_2SO_4-$FeSO_4$ binary system was carefully surveyed and the off-stoichiometric composition of the alluaudite-type sodium iron sulfate was revealed. Throughout charging/discharging processes, the structure undergoes a reversible, single-phase (solid solution) reaction based on a Fe^{3+}/Fe^{2+} redox reaction with a small volume change after an initial structural re-arrangement upon the first charging process. Sodium extraction occurs in a sequential manner at various Na sites in the structure at their specific voltage regions. The localized feature of Fe–O bond is observed in the pristine phase due to the strong inductive effect though Fe–O–S bond.

Overall, the obtained knowledges throughout the chapters contribute to the strategy for designing iron based cathode materials with superior electrode performances (e.g. electrode potential, rate capability, and cyclability). To date, an enormous number of iron based cathode materials and their relatives have been reported as active cathode materials. However, the design concept for superior cathode materials has not been well established yet because various factors strongly correlate with each other and trade-off relationships need to be considered in each case.

Here, approaches to improve the electrode potential will be summarized. One of the most widely accepted concepts to control the electrode potential is the "inductive effect" as discussed in Chapter 1. The high electronegativity of X uplifts the electrode potential of oxyanionic cathode materials, where the general formula is described as $A_xM_y(XO)_z$ (A = Li, Na, and Mg, M: transition metal, and X = B, Si, P, S, and etc.).

In the present thesis, the heterosite $FePO_4$ electrode exhibits a relatively low electrode potential for magnesium insertion in Chapter 3. Considering the mechanism of the inductive effect, substitution of phosphorous by sulfur is effective in increasing the potential of magnesium battery cathode. The desodiated phase of alluaudite-type sodium iron sulfate discussed in Chapter 4-7 might be suitable for magnesium intercalation in this context. Furthermore, the author also reveals that one can evaluate the inductive effect in semi-quantitative way in Chapter 7. The combination of the soft-XAS measurements and the LFM calculations indicate that the inductive effect through Fe–O–S bond is stronger than through the Fe–O–P bond; this is attributed to the higher electronegativity of sulfur than phosphorus. The inductive effect is independent of the intercalated guest species and host structures; therefore, the proposed method can be applicable for any oxyanionic cathode materials in lithium-ion, sodium-ion, and magnesium batteries. Note that systematic studies are still required to reveal the universality of the present evaluating method in future.

While the mechanism of the inductive effects are well known, structural mechanisms to upshift the electrode potential are still under debate. Chung *et al.* proposed that the closer Fe–Fe distance within edge-sharing configuration produces strong electrostatic repulsion between Fe^{3+}–Fe^{3+} at the delithated phase; this destabilizes the delithaited phase and upshifts the electrode potential of triplite-type $LiFeSO_4F$ (Ref. 133 in Chapter 1). In Chapter 4 and 5, this theory is further confirmed for alluaudite-type sodium iron sulfate. The obtained highest Fe^{3+}/Fe^{2+} redox potential of the alluaudite-type sodium iron sulfate can be due to the shortest Fe–Fe distances within the edge-sharing Fe_2O_{10} dimers. Furthermore, small SO_4 tetrahedra bridge two axial apexes of the Fe_2O_{10} dimers; this shortens the Fe–Fe distances and upshifts the electrode potential, further. One possible drawback for this local structural effect is discussed in Chapter 6. The strong coulombic Fe^{3+}–Fe^{3+} repulsion irreversibly moves the iron at the first charging process; this downshifts the average electrode potentials in the following processes. A long-time expected 4 V class cathode with iron compounds may be achieved if the irreversible structural change is suppressed. Structural modification methods (e.g. substitution of iron by the other transition metals and the control of Na/Fe ratio) are under consideration.

The current concepts are applicable for any given cathode material regardless of intercalation species once the structure is known. In spired by the current findings, the author expects more and more high-voltage cathode materials will come out in the near future. At present, a few studies have focused on dividing the inductive effect and the local structural effects. Rigorous studies are also required to quantitate these effects.

Thereupon, considerations for high rate capability and high reversibility will be discussed. At microscopic scale, these properties are governed by migration of guest species. General consideration for migration phenomena had already been completed for solid state ion conductors, as was summarized in Chapter 1. The present thesis provides one of the best examples for sodium-ion intercalation. Within the alluaudite-type $Na_{2+2x}Fe_{2-x}(SO_4)_3$ framework, the extremely fast sodium-ion migration between the Na3-Na3 sites is revealed in Chapter 4. This is mainly due to the shallow site potential of Na3 site, and the straight diffusion pathway along *c* axis. The wide open and straight channel of the alluaudite-type $Na_{2+2x}Fe_{2-x}(SO_4)_3$ might be adequate for the intercalation of magnesium. Besides, due to the intrinsic off-stoichiometric composition, the Na3 site is partially occupied even at the endmember pristine state; this increases the ionic conductivity further.

If magnesium occupies the Na3 site instead of sodium, the BVS value becomes much smaller than the formal valence of bivalent Mg^{2+}. This may suppress the deformation of the inserted phase observed in Chapter 3, and enable the reversible magnesium intercalation.

At macroscopic scale, all the electrochemical intercalation reactions can be categorized into the two-phase and single-phase solid solution reactions. In the present thesis, the properties of two-phase reaction became clearer. First, the kinetics of nucleation and growth in Li_xFePO_4 electrode system were revealed in Chapter 2. The nuclear-growth has activation energy lower than the lithium diffusion process at the endmember phases may due to higher electronic conductivity of Fe^{3+}/Fe^{2+} mixed valent phase at the phase boundary. The systematic study suggests that both the nucleation and nuclear-growth processes were accelerated by decreasing particle sizes due to the smaller lattice misfits between Li-poor and Li-rich phases and the increased number of nucleation sites. The observed phenomena may be generalized for a given two-phase reaction system. However, more systematic studies for two-phase reaction systems of other electrode materials (e.g. graphite, $Li_{1+x}Mn_2O_4$, $Li_{1+x}Rh_2O_4$ and $Na_{1+2x}V_2(PO_4)_3$) are necessary in order to obtain a universal understanding of the reaction mechanisms. Besides, the multi-particle effect (Ref. 103-105 in Chapter 1) is not negligible for any of those systems. The author believes combination with the electrochemical single-particle technique will provide more intrinsic information of the phase-boundary movements.

The amorphization of the $FePO_4$ phase may occur by non-topochemical Mg^{2+} intercalation as was discussed in Chapter 3. Though large polarizations between charging and discharging curves were observed, the Fe^{3+}/Fe^{2+} redox reaction occurs reversibly. This may suggest that the reversible electrode reaction might be possible between Mg-rich and Mg-poor amorphous phases. The author supposes that utilization of the amorphous phase prepared by intense ball-milling as the pristine compound for the electrode might be effective as the cathode material; this is due to the decrease of the length of migration pathway.

As another point of view, approaches to explore “unknown” materials will be briefly summarized. As was discussed above, large diffusion pathways without bottle necks and shallow potential of the sites are of importance to intercalate guest species. The host frameworks are totally different between lithium, sodium, and magnesium intercalation, as was suggested in Chapter 2 and 3. In this context, exploration of new compounds can be recognized as one of the valuable approaches to obtain the appropriate host frameworks.

The Na_2SO_4–$FeSO_4$ binary system is explored, and the alluaudite-type $Na_{2+2x}Fe_{2-x}(SO_4)_3$ with a totally new composition and with a new structure is identified in Chapters 4 and 5. The author supposes that there are two key factors for the discovery: (i) large unexplored region had existed in Na_2SO_4–$FeSO_4$ binary system between $Na_6Fe(SO_4)_4$ and $FeSO_4$ phases and (ii) the compound decomposes at relatively low temperature. First, the stability of the phase is governed by thermodynamics, which generally cannot be controlled. Thus, it is of particular importance to explore the region which have never been explored. One should survey the binary/ternary diagrams thoroughly, organize the information of reported phases, and find out the unexplored composition ranges. So far, prediction of unknown stable phase is difficult, and trial and error are one of the best ways for exploration. However, the author supposes that further investigations for new materials are in necessary. There are still unexplored regions in the quaternary diagrams, such as Na-Fe-PO_4-SO_4, Na-Fe-O-SO_4 and Na-Fe-SO_4-OH systems. New superior cathode candidates may come out from the explorations within these systems. Moreover, computational assisted ways have been rapidly developed in recent years. The a*b-initio* calculations to predict the structure from the composition of the compounds may become more popular, and will accelerate the screening of the targeted compounds in future.

More importantly, exploration for thermally metastable compounds can be a fruitful approach. Most of the structures for reported compounds are determined by the analyses for single crystals. Large driving forces (e.g. long-term high temperature and/or pressure) are generally required for the single-crystal growths. However, such growth methods cannot be applied for alluaudite-type $Na_{2+2x}Fe_{2-x}(SO_4)_3$ due to the relatively lower decomposition temperature and the considerably high hygroscopicity. At present, the single crystal of alluaudite-type $Na_{2+2x}Fe_{2-x}(SO_4)_3$ has never been synthesized. The author supposes that sulfate, carbonate, and oxalate compounds, which generally decompose at lower temperatures, still have plenty of rooms for exploration.

In conclusion, through the material exploration and reaction mechanism analyses, the strategy for designing iron based cathode materials with high electrochemical activity becomes more explicit. The thesis recalls the great importance of the search for new cathode materials, and contributes to clearing the path for discovery of new “earth-abundant” cathode materials for next-generation rechargeable batteries in future.

Acknowledgements

The present thesis entitled "Material exploration and reaction mechanism analyses for iron-based cathode materials for rechargeable batteries" has been completed under the supervision of *Professor Atsuo Yamada*, Department of Chemical System Engineering, Graduate School of Engineering, The University of Tokyo, Japan.

I would like to express my deepest gratitude to *Professor Atsuo Yamada* for his fruitful suggestions and discussions throughout the work. He has enthusiastically guided me in "fatherlike" way. His ideas are always far-sighted and his advice is extremely helpful to improve the research. Even when my research did not progress well as per expectation, he positively encouraged me to carry on while focusing the long-term goal of the study. He provided me several opportunities to collaborate with other groups, even in other countries. These experiences abroad helped me broaden my horizon. I learnt from him not only about science but also about the correct attitude towards research, discussion, writing and presentation, which should also be extremely helpful for my future. It is my pleasure to conduct research under his supervision starting from my Bachelor degree till the PhD degree. I would like to express my deepest thankfulness to him again.

I am indebted to *Dr. Shin-ichi Nishimura*, who helped me throughout the present thesis. His discussion and dedicated support were always helpful to clarify the results and obtain deeper insight. Especially, I would like to thank him for determining the initial structure of the alluaudite-type sodium iron sulfate in Chapter 4. All the other refinements in Chapter 5 and 6 are based on his model. These studies could not have been completed without him. Besides, he helped me to acquire synchrotron XRD patterns, and data for XANES at KEK-PF. It is thanks to his training, particularly during my Bachelor and Master degree, that all the work for XRD, SEM observation and Mössbauer spectroscopy techniques could be done throughout Chapter 2-7. Over the past few years, discussions with him regarding the future prospects of rechargeable batteries, intercalation chemistry, and solid state chemistry were truly valuable to me.

I mention heartfelt thanks to *Dr. Prabeer Barpanda* (Indian Institute of Science, India) for his outstanding guidance particularly in Chapter 4. I would like to thank him for providing the idea to explore new materials in the Na-Fe-S-O system and his initial guidance for syntheses of the sulfate based compound from his abundant experiences. It is obvious that all the work in Chapter 4-7 could not have been accomplished without his idea. I would also like to thank him for revising Chapter 4 into idiomatic English.

I am genuinely grateful to *Dr. Masashi Okubo* for reviewing logical writing in English in Chapters 3 and 5. His comments were truly helpful for discussing the results in a more concise way. He also provided invaluable advices for presentations in conferences. I would like to thank his fruitful comments, which helped in improving the discussions regarding the XAS simulations in Chapter 7.

I would like to express my thankfulness to *Dr. Sai-Cheong Chung*, who performed the first principle calculations in Chapter 3 and 4. He also helped me to interpret the calculation results in Chapter 7. It is always interesting and productive to have discussions with him because of his deep knowledge regarding the essence of the theory.

I sincerely acknowledge *Dr. Yuki Yamada*, who helped me in improving my English writing and the discussions in Chapter 2 from his background in electrochemistry. Owing to his help during the earlier stage of my research, all the following studies could proceed more smoothly.

I truthfully thank *Mr. Ryu-ichi Natsui* (Panasonic corporation, Japan), who is an ex-member of Yamada laboratory at Tokyo Institute of Technology. In Chapter 2, he was the one to initiate the work for gaining insight regarding the kinetics of electrode reaction, and this initial step was absolutely necessary. His work was beneficial in pursuing the work after him.

I am deeply grateful to *Professor Haoshen Zhou* (National Institute of Advanced Industrial Science and Technology, Japan) for his precious comments and discussions at laboratory meetings.

I would like to thank *Dr. Jun Ming*, *Dr. Mortemard De Boisse Benoit*, *Mr. Jiechen Lu*, *Mr.*

Kazuhiko Kai, *Mr. Suhao Wei*, *Mr. Yuya Suzuki* and *Mr. Abhishek Panigrahi* for their meaningful discussions for related iron based cathode materials. They revealed knowledges from their researches which was beneficial for improving the discussion in the present thesis.

I truly thank *Mr. Noboru Yoshida*, *Mr. Sho Furutsuki*, *Mr. Naoya Furuta*, *Mr. Daisuke Shimizu*, *Mr. Makoto Yaegashi*, *Mr. Keizo Furukawa*, *Mr. Takeyuki Ishimi, Ms. Tien Ye,* and *Mr. Yasunobu Yamashita*, who are senior members and colleagues in Yamada laboratory. Their thorough discussions during the laboratory meetings were very helpful and in pursuing fair competition with them I was able to truly polish my research work. I would also like to thank them for our friendships ever after their graduations.

I am grateful to all the members of Yamada-Okubo laboratory, *Dr. Satoshi Kajiyama, Dr. Akira Sugawara, Dr. Wenwen Zhao, Mr. Seongjae Ko, Mr. Kenji Usui, Mr. Yuki Sugimoto, Mr. Ching Hua Chiang, Mr. Hiroki Iinuma, Mr. Koji Takada, Mr. Yusuke Morikawa, Mr. Jiangtao Ma, Mr. Hikaru Oka,* and *Mr. Kyosuke Doi* for their hearty supports for daily life in the laboratory. Particularly, I am sincerely grateful to *Ms. Nobuko Miyakubo, Ms. Koyama,* and *Ms. Noriko Sanpei,* who are the secretaries in Yamada-Okubo laboratory. I would like to thank them for helping me kindly and encouraging me.

I am sincerely grateful to *Dr. Oliver Pecher*, *Mr. Kent J. Griffith*, *Ms. Roberta Pigliapochi*, and *Professor Clare P. Grey* (University of Cambridge, UK) for constructive and open minded discussions, and supports for ^{23}Na MAS NMR experiments. *Dr. Oliver Pecher, Mr. Kent J. Griffith* helped me to acquire ^{23}Na MAS NMR spectra, *Ms. Roberta Pigliapochi* conducted the NMR shift calculations in Chapter 6, and *Professor Clare P. Grey* provided profound insight, particularly for the interpretation of the NMR results. Besides, I would like to thank them for supporting me during my student life at Cambridge.

I am truly grateful to *Professor Yoshihisa Harada, Mr. Hisao Kiuchi* (The University of Tokyo, Japan) for their support in measuring soft-XAS at Spring 8, which were discussed in Chapter 7. Within the MERIT self-directed joint research, we came up with the work, but it was still difficult for us to start up the research at the initial stage. I sincerely thank him for convincing his supervisors to help us pursue this research work. I would also like to express my great thankfulness to *Professor Yoshihisa Harada* for his wonderful discussions regarding the soft-XAS.

I am obliged to *Professor Masashi Kawasaki* (The University of Tokyo, Japan) for his precious advices as the mentor through Material Education program for the future leaders in Research, Industry, and Technology (MERIT) program. His comments based on his backgrounds both in engineering and academics were extremely helpful not only to the present thesis but also for improving my future outlook.

I am deeply thankful to committee members for the dissertation, *Professor Tatsuya Okubo*, *Professor Koichi Yamashita*, *Professor Kazunari Domen* (The University of Tokyo, Japan), and *Professor Shinichi Komaba* (Tokyo University of Science, Japan). Owing to their comments in the defense, the discussion has deepened throughout the work. I am indebted to *Professor Tatsuya Okubo*, who is the vice supervisor at my Master's degree. First, he provided many fruitful comments for Chapter 2. Owing to his precious comments during the defense, the general discussions and future perspectives, which are essential parts of the thesis, have been significantly improved. I would like to thank him again for providing the opportunity for improvements. I am indeed grateful to *Professor Koichi Yamashita* for providing me valuable comments regarding calculation results and for helping me kindly. Owing to his comments, the discussions in Chapter 4, and 7 are upgraded. I would like to express my thankfulness to *Professor Kazunari Domen,* who provided me with his valuable comments since my Bachelor's degree. I am obliged to *Professor Shinichi Komaba* for providing me heartfelt comments for the work. Based on his comments, the discussions in Chapter 3 are improved.

I would also like to mention my deepest thankfulness to *Professor Yukio Yamaguchi*, and *Professor Suguru Noda* (Waseda University, Japan) for providing me valuable comments regarding Chapter 2. Besides, I deeply apologize for my arrogant attitude regarding the discussions at the defense presentation, and would like to keep in mind not to commit the same mistake henceforth.

Last but not the least, I wish to express my special thanks to my family for their continuous support and encouragement throughout my student career and towards accomplishing this work.

Gosuke Oyama
February, 2016
Tokyo, Japan